



Attribution–NonCommercial–NoDerivs 2.0 KOREA

You are free to :

- **Share** — copy and redistribute the material in any medium or format

Under the following terms :



Attribution — You must give [appropriate credit](#), provide a link to the license, and [indicate if changes were made](#). You may do so in any reasonable manner, but not in any way that suggests the licensor endorses you or your use.



NonCommercial — You may not use the material for [commercial purposes](#).



NoDerivatives — If you [remix, transform, or build upon](#) the material, you may not distribute the modified material.

You do not have to comply with the license for elements of the material in the public domain or where your use is permitted by an applicable exception or limitation.

This is a human-readable summary of (and not a substitute for) the [license](#).

[Disclaimer](#) 

Ph.D. DISSERTATION

**HIGHLY ELECTRICALLY
CONDUCTIVE TUNGSTEN DOPED
REDUCED GRAPHENE OXIDE
FILM AS LARGE CURRENT
DENSITY FIELD EMITTER**

높은 전기전도를 가진 텅스텐 도핑된 환원된 산화그래핀
고전류 전계방출소자

BY

RANAJAY BHATTACHARYA

FEBRUARY 2018

GRADUATE SCHOOL OF SEOUL NATIONAL
UNIVERSITY
DEPARTMENT OF ELECTRICAL ENGINEERING AND
COMPUTER SCIENCE

공학박사 학위논문

**HIGHLY ELECTRICALLY
CONDUCTIVE TUNGSTEN DOPED
REDUCED GRAPHENE OXIDE
FILM AS LARGE CURRENT
DENSITY FIELD EMITTER**

높은 전기전도도를 가진 텅스텐 도핑된 환원된 산화그래핀
고전류 전계방출소자

2018 년 2 월

서울대학교 대학원

전기·컴퓨터 공학부
라나조이 바타차리야

HIGHLY ELECTRICALLY CONDUCTIVE TUNGSTEN DOPED REDUCED GRAPHENE OXIDE FILM AS LARGE CURRENT DENSITY FIELD EMITTER

Supervised by
Professor Gun-Sik Park

A Thesis Submitted to the Department of Electrical
Engineering and Computer Science, Graduate School of
Seoul National University in Partial Fulfillment of the
Requirement for the Degree of Doctor of Philosophy

by

Ranajoy Bhattacharya
Department of Electrical Engineering & Computer Science
College of Engineering, Seoul National University

February 2018

Confirming the doctoral thesis written by

Ranajoy Bhattacharya

Chair Nam, Sangwook (Seal)

Vice Chair Park, Gun-Sik (Seal)

Examiner Seo, Kwang Seok (Seal)

Examiner Park, Namkyoo (Seal)

Examiner Cho, Boklae (Seal)

Sangwook Nam

Gun-Sik Park

Kwang Seok Seo

Namkyoo Park

Boklae Cho

Abstract

Exploration of the Terahertz (THz) gap, in the field of medical, defense, communication, material processing etc, primarily suffering from the lack of high power, efficient sources, which can be supplemented vacuum electron devices (VED). But to realize practical THz range VED's, cathode with extreme current density is in immense need.

In this thesis, we are motivated to synthesize and develop a field emitter cathode, based on graphene film that could deliver current density up to $10000\text{A}/\text{cm}^2$ as an electron source for THz VED's. Previous studies were carried out on the influence of various cathode parameters such as, free standing nature, thermal and electrical conductivity, mechanical strength for better stability and long life, thickness and width for controlling the current density, to get a deeper understanding of the mechanism of field emission and the improvement & stability of emission performance. Further analysis show that the emission performance is influenced by the presence of impurities such as oxygen functional groups etc. That is if the impurity is less, emission would be higher. Also, the thermo-electrical properties and mechanical stability has an important role to play regarding the stability during operation, which is degraded by those above mentioned impurities. Considering all the before mentioned aspect, a chemical synthesis process was developed to synthesize impurity free, freestanding reduced graphene oxide (rGO) film with improved physical properties. It is known that doping of metal to rGO films improves the physical properties by several times and consequently the field emission performance. Previous reports and study have shown that if the physical properties have been improved by at least two times comparing to as prepared rGO, stable emission can be achieved even when the emission current density is being doubled or more than that. The reason behind this can be explained as, the improved properties can handle the higher thermo-electrical load generated by the larger field emission current. Prepared tungsten doped reduced graphene oxide (W-rGO) film was characterized using, Field Emission Scanning Electron Microscope (FESEM) to study the surface morphology and the thickness. X-ray Photoelectron Spectroscopy

(XPS) was used to study the surface chemical & elemental information, doping & doping homogeneity, and carbon-carbon bonding status. Further, X-ray Diffraction Spectroscopy(XRD) was carried out to study the doping mechanism and layer distance information. Raman spectroscopy was utilized to study the effect of tungsten doping on carbon network morphology and improvement in carbon-carbon bond. It was found that the doped film has much more improved structure than the as-prepared film.

Experimental characterization was carried out on both, the doped and un doped films to compare the improvement in physical properties. It was found that doped film, in all three cases, such as thermal, electrical and mechanical, have much more improved properties than the non-doped films. Field emission experiment was carried out inside of an ultra-high vacuum (UHV) chamber on both of the films. The emission results are extremely positive. A very large current density of $\sim 6000\text{A}/\text{cm}^2$ was achieved at an applied electric field of $7.4\text{ V}/\mu\text{m}$, with a superior stability from the doped films where un-doped films, though initially delivered a current density of $4300\text{A}/\text{cm}^2$, eventually got degraded and was able to deliver only a current density of $\sim 2300\text{A}/\text{cm}^2$. It is of an interesting phenomenon that the I-V characteristics have a growing nature for higher anode fields. This means that, with more efficient setup, where high voltage breakdown can be controlled, higher current density can be achieved.

Keywords: rGO film, tungsten doping, improved physical properties, field emission, stability, THz electron source.

Student ID: 2013-30772

Contents

Abstract	i
List of Figures	v
List of Tables	viii
Chapter 1 Introduction of Field Emitter Cathodes	1
1.1 Introduction	2
1.2 Historical Background	4
1.2.1 Evolution of Field Emitter Cathodes	4
1.2.2 Evolution of Graphene	5
1.2.3 Application of Graphene.....	8
1.2.4 Evolution of Graphene based Field Emitters.....	9
1.3 Field Emission Mechanism.....	11
1.4 Motivation	13
1.5 Goal	15
1.6 Organization of The Thesis.....	15
Chapter 2 Novel Synthesis Method for W-rGO Field Emitter Cathode	17
2.1 Previous Synthesis Methods	18
2.2 Requirements of Hybrid Film Parameters	19
2.3 Choice of Synthesis Process for W-rGO Film.....	20
Chapter 3 Synthesis and Structural Characterization of W-rGO Film.....	22
3.1 Synthesis of W-rGO Films.....	23
3.2 Structural Characterizations.....	25
3.2.1 Characterization of Morphology.....	25
3.2.2 Characterization of Doping Homogeneity	29
3.2.3 Raman Spectroscopy	32
3.2.4 X-ray Diffraction Spectroscopy	36
3.2.5 X-ray Photoelectron Spectroscopy.....	40

Chapter 4 Characterization of Physical Properties of W-rGO and Shaping of Film.....	50
4.1 Experimental Characterization Of Electrical Conductivity.....	51
4.2 Experimental Characterization of Thermal Conductivity	56
4.3 Experimental Characterization of Mechanical Properties.....	61
4.4 Shaping of the Synthesized Film using Microtome Cutting Technique.....	65
Chapter 5 Realization of W-rGO film field emitter cathode	67
5.1 Fabrication of Cathode	68
5.2 Details of Experimental Setup for Emission Measurement	70
5.3 Characterization of W-rGO Film Field Emitter Cathode.....	72
5.3.1 Emission Measurement	72
5.3.2 FESEM Characterization of Post-Experiment Emission Edge	78
Chapter 6 Discussion Of Results, Conclusions, And Suggestions For Future Work.....	80
6.1 Study of Graphene Field Emission	82
6.2 Study Of Various Synthesis Methods for rGO Film.....	82
6.3 Synthesis and Characterization Of W-rGO Film	83
6.4 Characterization and Shaping of Synthesized Film	84
6.5 Realization of W-rGO Film Field Emitter Cathode	85
6.6 Suggestions for the Future Work	86
Bibliography	88
List Of Publications.....	99
Appendix-I	104
Korean Abstract	105
Acknowledgements.....	107

List of Figures

Figure 1.1: Mechanisms of thermionic and field emissions.....	3
Figure 1.2: Typical field emitter cathodes. (a & b) Spindt type emitters. (c) Silicon based emitter. (d) Carbon nano tube array.....	4
Figure 1.3: Current density development of field emitters in terms of effective emission area.. ..	10
Figure 1.4: (a) EM spectrum (b) Available THz devices.....	14
Figure 2.1: General classification of graphene synthesis process	18
Figure 2.2: Common synthesis approach for rGO	19
Figure 2.3: Comparison of physical properties of tungsten with other dopants	21
Figure 3.1: Flow diagram of the synthesis processes to prepare W-rGO film	24
Figure 3.2: (a) Bucky paper (b) Custom made drying chamber for buckypaper...	26
Figure 3.3: In-house developed hydrothermal vessel	26
Figure 3.4: Schematic diagram of Scanning Electron Microscope	27
Figure 3.5: Morphology of rGO & W-rGO obtained from FESEM.....	28
Figure 3.6: SEM image taken during the EDS analysis, indicating four locations (I, II, III and IV) on the image from where EDS spectra was taken ...	29
Figure 3.7: EDS spectra taken at (b) location I, (c) location II, (d) location III and (e) location IV.	30
Figure 3.8: Schematic diagram of Raman spectroscope	33
Figure 3.9: (a) Raman spectra of the synthesized rGO and W-rGO films annealed different reduction temperatures, that is 400°C, 600°C, 800°C, 1000°C and 1200°C. (b) I_D/I_G curve.....	34
Figure 3.10: Schematic diagram of Scanning X-ray diffractometer.....	36
Figure 3.12: Schematic diagram of X-ray photo electron spectrometer	41
Figure 3.13: (a) C1s and (b) O1s for rGO film obtained from XPS analysis, annealed at 800°C	42
Figure 3.14: (a) C1s (b) O1s for W-rGO film obtained from XPS analysis, annealed at 1200°C	43
Figure 3.15: (a) XPS spectra for tungsten, (b) Oxygen at% & carbon to tungsten ration as a function of annealing temperature	44
Figure 3.16: (a) wt% of elements present in as-prepared film and film after annealing at 800°C for rGO film, (b) wt% of elements present in as-prepared film and film after annealing at 1200°C for W-rGO film.....	45

List of Figures

Figure 3.17: Comparison of at% of elemental data from EDS and XPS analysis. (a) rGO annealed at 800°C and (b) W-rGO annealed at 1200°C	48
Figure 3.18: Comparison of work functions calculated from UPS analysis	49
Figure 4.1: Schematic diagram of 4-point probe measurement system	52
Figure 4.2: Film samples loaded on a 4-point probe measurement stage	52
Figure 4.3: Measurement of sheet resistance for (a) rGO and (b) W-rGO as a function of annealing temperature and corresponding oxygen wt% ..	53
Figure 4.4: Calculated electrical conductivity for (a) rGO and (b) W-rGO as a function of annealing temperature (Inset: Comparison of electrical conductivity).....	54
Figure 4.5: Schematic diagram of a laser flash system	57
Figure 4.6: Thermal conductivity data acquired from laser flash analysis as function of temperature. (a) rGO shows much lower conductivity than (b) W-rGO.....	58
Figure 4.7: (a) Cross plane and (b) in-plane conductivity plot for rGO and W-rGO films as a function of temperature.. ..	59
Figure 4.8: Schematic diagram of a universal testing machine.....	62
Figure 4.9: (a) Tensile test graph for rGO (800°C) and W-rGO (800°C & 1200°C) (b) comparison Young's modulus	64
Figure 4.10: (a) Shaping using microtome (b) Shaped films inside paraffin wax... 66	
Figure 5.1: (a) Shaped W-rGO film (b) Film loaded inside experiment jig	69
Figure 5.2: (a) Schematic diagram of test set-up. (b) Photograph of analytical system.....	71
Figure 5.3: Field emission experiment data. (a) Field emission current as a function of applied potential for the rGO (800°C) and W- rGO(1200°C) films. (b) Calculated emission current density for rGO (800°C) and W-rGO(1200°C) films.	75
Figure 5.4: (a) F-N plot. (b) Stability measurement over a period of 192 Hr. Applied potential was 3.3 kV	76
Figure 5.5: 1000 Hr stability test reveal that the W-rGO films is remarkably stable over a long period of time and can be used in practical devices.....	77
Figure 5.6: Beam shape captured on a phosphor screen on ITO glass.....	77
Figure 5.7: After experiment SEM image. Physical damage is clearly visible for the case of (a)rGO, where (b)W-rGO film retained the structure	79

List of Tables

Table 3.1	31
Table 3.2	38

CHAPTER 1

Introduction of Field emitter cathode

1.1 Introduction

1.2 Historical Background

1.2.1 Evolution of Field Emitter Cathodes

1.2.2 Evolution of Graphene

1.2.3 Applications of Graphene

1.2.4 Evolution of Graphene Field Emitters

1.3 Field Emission Mechanism

1.4 Motivation

1.5 Goal

1.6 Organization of The Thesis

1.1 Introduction

Microwave and terahertz (THz) range [1] high power vacuum electron devices (VED) has numerous applications in medical, communication, security, and imaging. The development of such devices require electron sources (cathodes) of large current density with stability and uniformity in emission. Therefore, the study of electron emission mechanism has become a key requirement.

Emission of electron is a process where, electrons are emitted into vacuum from the surface of a solid. The work function(Φ) can be described as the lowest energy needed for an electron to elude from Fermi level to vacuum. In order to extract electrons from the surface of a solid, energy need to be applied to the solid surface through different processes to prevail over the potential barrier. Thermionic and field emission are two of the most widely used processes for extraction of electrons [2]. In these approaches, heat or electric field is applied to obtain electron emission. The mechanism of emission can be elaborated with the help of figure 1.1, where energy band diagram of a metal-vacuum system is exhibited.

In thermionic emission case, due to the applied thermal energy, electron escape into vacuum. At room temperature, electrons inside a metal body have energy below the Fermi level (F_E). However, as temperature increases, some electrons acquire kinetic energy higher than the Fermi level. If temperature is adequately high, some electrons can gain energy to overcome the energy level (E_{vac}) of vacuum. These electrons escape into vacuum without any applied potential. Thermionic emission from metal is generally occurred under a large applied temperature, typically in the range of 1000°C-2000°C depending on the specific work function(Φ) of the metal. However, this large temperature is of a problem when the applied device dimension is comparatively smaller and heat dissipation rate is below the requirement. Also due to the large temperature, thermal spread is large, therefore researchers were looking for an alternate electron source like field emitters [3] where those above mentioned issues would be overcome. However, so far the development in field emitters have not seen such a progress, mainly due to instability and eventual degradation. In recent years, carbon based field emitter [4] such as carbon nano-tube, graphene, graphene oxide etc. have shown significant improvement, because of their strong carbon

backbone. Among them graphene [5] has seen an uprising because of its unmatched properties compared with other carbon based emitters.

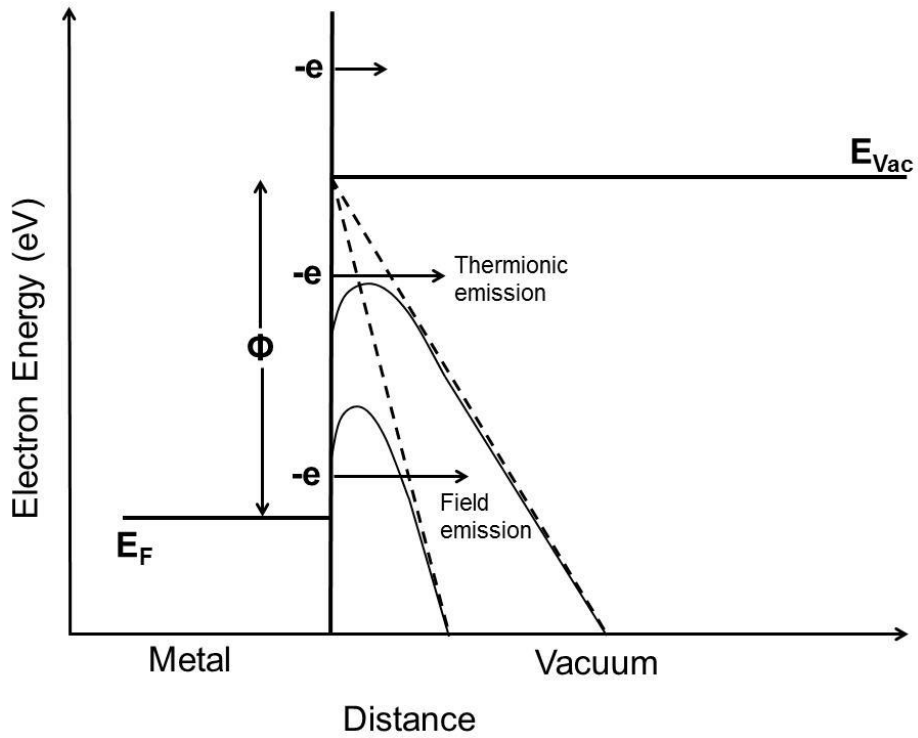


Figure 1.1: Mechanisms of thermionic and field emissions.

1.2 Historical Background

1.2.1 Evolution of Field Emitter Cathode

Among different field emitters, a field emitter array (FEA) [6] is made of large-area field electron source with multiple sharp edges. Typical field emitter array is prepared on a silicon substrate by lithographic [7], Chemical vapor deposition (CVD) [8], micro or nanotechnology similar to those used for the fabrication of integrated circuits etc. Their structure consists of an extremely large number of individual but identical, small size field electron emitters, typically arranged in a regular needle like two-dimensional pattern. FEAs require to be distinguished from planar type large area electron sources, where a very thin layer of emitter material is deposited on a substrate outer surface, using a uniform deposition method. Required electric field to extract electron by means of field emission is extremely large, typically in the range 1~10 GV/m, but can be achieved by using extremely sharp nano-tips.

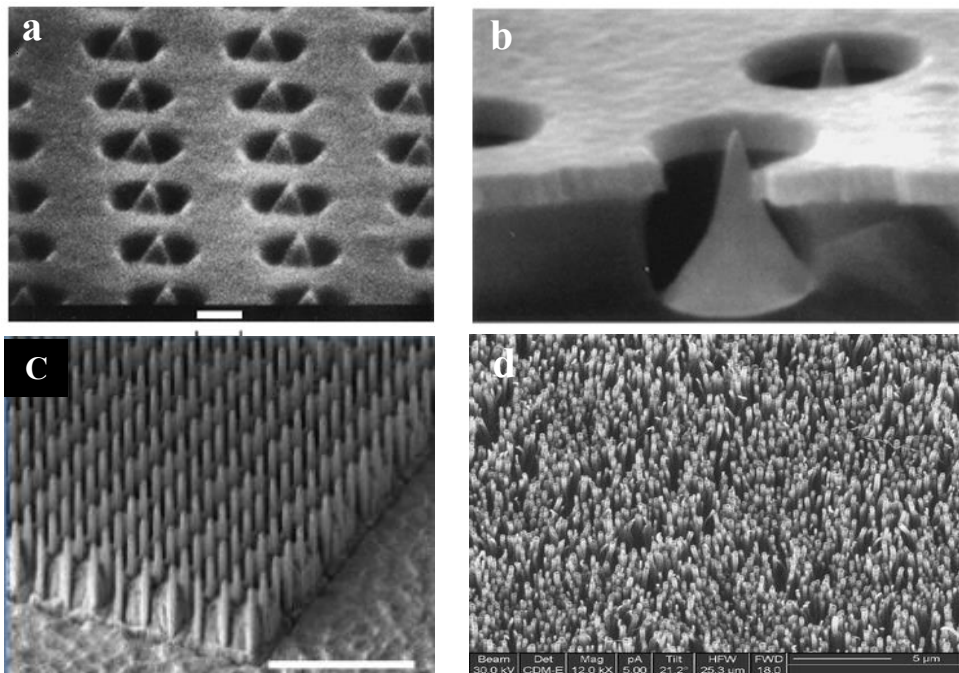


Figure 1.2: Typical field emitter cathodes. (a & b) Spindt type emitters. (c) Silicon based emitter. (d) Carbon nano tube array.

When one of the electrode of a diode is replaced with such arrangements of nano-tip having a tip apex radius of curvature in few nanometers range, the apex field (microscopic field on tip top) can be quite a few times larger than the uniform field determined by the macroscopic separation between the diode electrodes. A common example of filed emitter is spindt type (Fig.1.2(a & b)) silicon (Figure 1.2 (c)) and carbon nano-tube array (Figure 1.2 (d)).

1.2.2 Evolution of Graphene

What is Graphene?

Graphene is a 2-dimentional structure made of pure carbon and was considered present only in theories, for last few decades. In the year of 2004 Andre Geim and Konstantin Novoselov succeeded to synthesize single layer graphene [5] using scotch tape with a procedure called mechanical exfoliation. Nobel Prize in Physics in 2010 were awarded to Geim and Novoselov for the realization of graphene. During this time, around 3000 articles related to graphene research were published and more than 400 number of patent applications was recorded. In this context, it is not hard to say that 2010 was the year of star of graphene era. During that period, a news article in Nature [9] revealed that, several countries are planning to invest millions of US dollars to graphene research in an effort to commercialize the material. New graphene related research work (in nanotechnology) are coming out almost every day. Keep pace with the growth in study related to graphene is becoming quite demanding, and the rate of new findings show no sign of saturation. Single atom thick layer of sp^2 -bonded carbon atoms are building structure of graphene, where carbon atoms are packed into a honeycomb like crystal lattice form [10], [11]. The name “graphene” is often used for multiple layer graphene mistakenly, where the difference in properties are largely significant while comparing single and multilayer structure. It is noticeable that up to ten layers of graphene sheets can be called graphene, where it is called few layer graphene (FLG, from three up to nine layers). Ten or more layers of graphene forms graphite. The single atomic structure of graphene exhibits exceptionally large optical, electrical, thermal, and mechanical properties [12]. The most fascinating electrical properties are very high electron mobility, ballistic transportation of charge carriers and high electrical conductivity.

However, there are quite a few disadvantages exists for graphene. One of the primary disadvantage is zero bandgap semiconductor structure. The absence of bandgap in graphene may be the most the difficult engineering issue considering large scale manufacturing. Graphene cannot switch from conductive to non-conductive state as a result of the absence of bandgap. The non-existing bandgap might be an issue, if graphene is meant to be utilized in metal oxide semiconductor logic circuits [13]. However, the zero gap of graphene may not be a problem in other cases, for an example, radio frequency (RF) applications, membrane filters etc. Other applications including graphene thin film electrodes, photodetector also have a future prospective. Along with others, one of the most extensively studied graphene application today is the graphene based field emitter sources. The advantage of a graphene field emitter [14] is based on its structure and physical properties. It has an atomic to nanometer range (GO or rGO) thickness, extremely large aspect ratio (the ratio of length to width), unprecedented electrical & thermal conductivity, and equally exceptional mechanical strength, which represent it as a potential cathode candidate.

Graphene Electronics Structure

Graphene is made of hexagonally structured, sp^2 -bonded carbon atoms. The configuration of electronic band in graphene can be explained with the linear-combination of atomic orbitals (LCAO), or similar tight binding approximation (TBA), where both are commonly used to explain graphene chemically. The π - π bands of graphene is made of 2×2 Hamiltonian, where the honeycomb structure has 2 atoms per unit cell. The off-diagonal components of the Hamiltonian explain the three closest neighbor interactions in different sub-lattices where diagonal elements illustrate the nearest neighbor interactions. A detailed derivation of the graphene electronic band structure can be obtained from [15]. Graphene primarily has a 2D structure, but it is also can be found in bi-layer and few-layer form (FLG) [16]. Bi-layer graphene has a quite different electronic band structure from single layer graphene. Hundreds of milli electron volt bandgap can be achieved in case of bi-layer graphene by perpendicularly applied electric field [17]. The bandgap in packed bi-layer graphene originate from the pseudospin generating in-between the layers, hence introducing an electrically induced band gap [18]. There are quite a few

numbers features of graphene that have not been explored yet. In case of large area graphene sheets, the presence of band gap is still debatable. However, in practice, apart from bandgap generation using external electric field in graphene bilayer structure, it is also possible to introduce bandgap by fabricating graphene nanoribbons (GNR) where quantum confinement effect takes place [19]. In GNRs, edges might have significant influence on electrical properties, which is still being actively researched. Numerical simulations have shown that band opening induced by strain might be possible. Nevertheless there is no experimentally confirmed evidence of bandgap induced by strain [20]. Engineering the graphene band structure is crucial regarding the competition with silicon for the case of applications in semiconductor technology [21]. The energy bandgap is critical for logical gate applications to have a minimum power uses i.e. shift to the off state. Graphene band structure is different from common semiconductor band structures. In graphene case, the energy dispersal at the band edge is not quadratic but linear [22]. Charge carrier mobility is restricted by impurity in the graphene and/or defect in supporting material. The preceding statement is supported by considerably larger motilities realized in graphene sheets suspended on substrate. Ballistic transport in graphene is a kind of electronic transport, which is restricted by scattering. Ballistic transport is realizable only in graphene sheets with large purity and free of defect. However, procuring pure and defectless graphene is strenuous and most of the time, it is not possible. The linear band dispersal in graphene denotes that the electron velocity is independent of momentum or energy. Moreover, the electron velocity in graphene is $1/300$ of the speed of light or at the maximum Fermi velocity. It is of interest that, backscattering is forbidden, not even through charge impurities or phonons scattering. Although, graphene electrical properties have been studied rigorously, but still, thermal and mechanical properties are yet to be explored in a large way. Graphene has a similar mechanical and thermal properties compared to carbon nanotubes(CNT). Experimental measurements show that the graphene has a tensile strength around 40N/m , and a large thermal conductivity, approximately 5000W/mK . However, the thermo-mechanical properties of graphene are mostly unexplored till date [23]. Although it shows much promise, but the chemical study of graphene is still in the early stage. Graphene is capable of assimilate and dissimilate several atoms and

molecules, such as O and OH, where this adsorbates have an effect on the electronic properties. Localized doping is feasible. However, the stability of graphene under different environment has not been studied extensively.

1.2.3 Applications of Graphene

Graphene is a purely two dimensional materials. Vertically stacked, hundreds of layers of graphene forms graphite which is a three dimension materials. Graphene can be rolled to form CNT, and also can be made in a ball shape to form fullerenes which is OD materials.

Primary statement in Moore's law is that, every two years, transistor number in integrated circuit gets double [24]. Graphene has established itself as one of the best examples of Moore's law, since its discovery in 2004. According to the research community, without expanding the fabrication budget to a higher level where the price of an individual transistor will be quite large, linewidth of transistor cannot be reduced for longer. Although, graphene research, initially was focused on thin film and transistors applications, implementation of graphene in other applications also growing steadily [25]. A large number of articles on graphene photodetectors and sensors have been published lately. It has been showed that graphene can be used as a gas sensors as the electrical conductivity of graphene is highly sensitive doped gas molecules [26]. Graphene material for nano electromechanical systems [27] can be a another interesting application. A graphene sheet deposited on drain and source and the gate below, can be used as a RF nano electromechanical device. In the megahertz range, nano electromechanical devices has an application in RF electrical transducer with specific oscillation frequencies. In optoelectronic research, graphene is coming up with speed after the recent discovery of its fine structure constant of constant $\alpha = 1/137$ [28], by which its opacity could be detected. Among the applications described previously, using graphene as a field emitter could be the closest one to emerge [14]. Graphene has shown exceptional performance in micro and nano structures, because of its excellent physical properties. The currently used material for micro and nano level field emitter is carbon nano tube (CNT). However, CNT has limitations because of its geometric structure, physical properties and screening effect [29]. CNT becomes fragile and has comparatively low electrical conductivity [30]. Necessity

for another material as a substitute to CNT comes primarily from the lack of reliability, deficit in current density, and long life. At this moment, graphene based field emitters are the most advantageous technology to replace previous field emitters. Production of graphene flakes and large sheets are going on in several companies, such as Graphene super market, Graphenea, etc.[31]. Efficient field emitters are required in a varieties of applications, such as field emitter display, field emitter transistors, large current field emitter for vacuum electron devices etc.

1.2.4 Evolution of Graphene based Field Emitters

Due to these outstanding properties of graphene, discussed in previous section, graphene field emitters have been successfully constructed by various methods and these emitters demonstrate considerable promise for application in electron field emission. Because of these properties, they can provide electrically conductive channels for faster electron transportation and tunneling, can be tuned to a lower work function, reduce the screen effect of the adjacent emitters and can be much stable even in larger field emission current also [14], [32]–[34]. Also, graphene emitters have the low threshold field, large field emission current density, superior stability and reproducible performance. Hence, graphene can be an excellent cold field emitter, replacing conventional emitters. Study on single and multi-layer graphene field emission is becoming an attractive topic in recent years although it's a challenge for experimental measurement. The high aspect ratio (thickness to width size ratio) and as a result, enhanced electric field on its sharp edges are accountable for high field enhancement and consequently to an electron field emission current. Extensive research work is being carried out on the field electron emission characteristics of varying shapes and sizes of graphene flakes. But due to random orientation, average current density is still in the order of few $\mu\text{A}/\text{cm}^2$ [35], [36]. However, applications where large current density is required from a relatively compact structure, these flakes are not useful. Fortunately, rGO has proved to be an answer to this issue. From a vertically oriented rGO film with thickness of few tens of μm , $\sim 10\text{A}/\text{cm}^2$ [37] of current density was extracted which is extremely large for a single cold field emitter. However, a detailed analysis of electron emission from thinner, freestanding rGO film is also necessary in order to extract larger current

density from a single emitter. Nonetheless, those emitters require to have optimum physical properties, in order to sustain the thermo-electrical load during field emission, as for a thin film, smaller the cross section, larger the load.

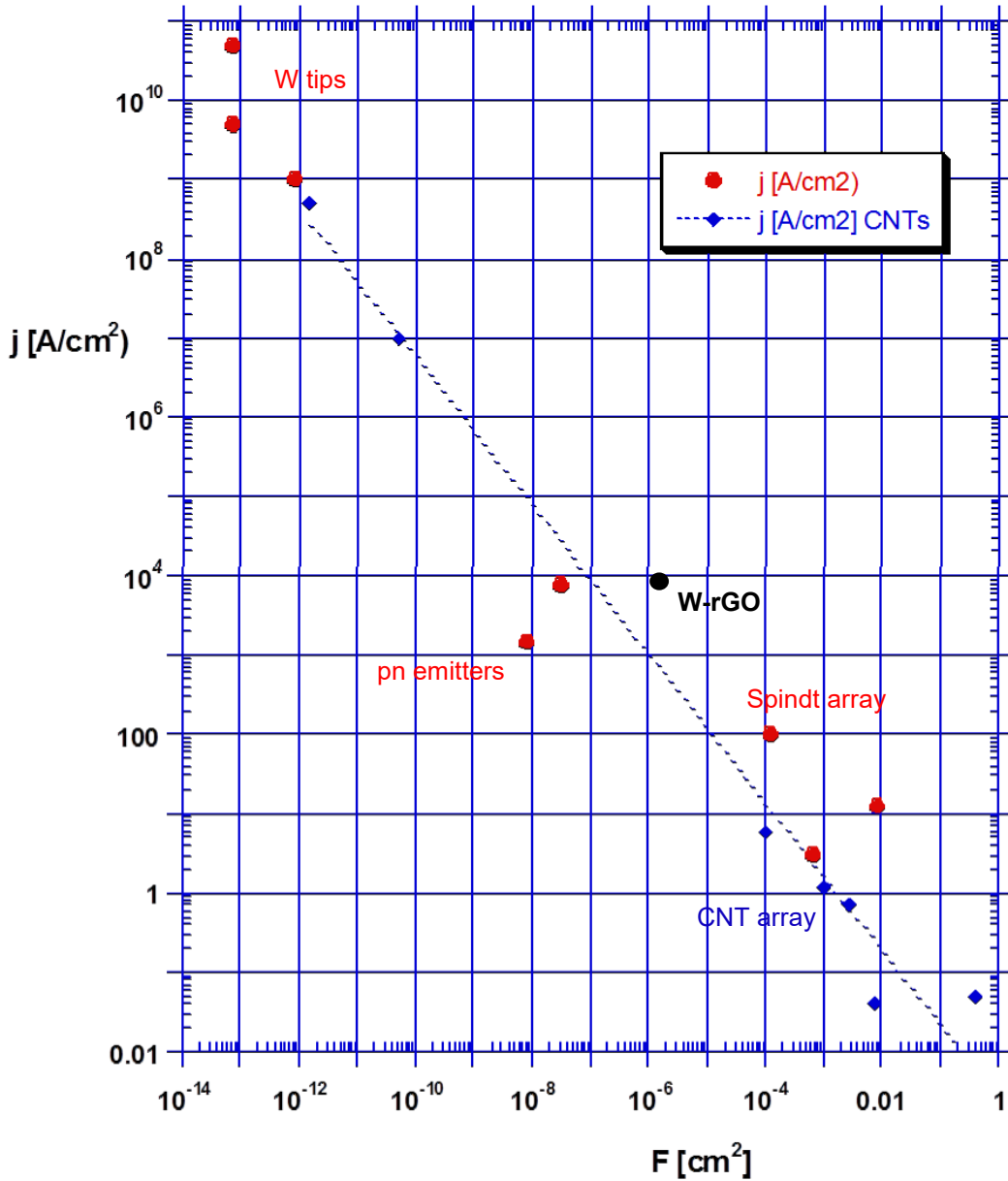


Figure 1.3: Current density development of field emitters in terms of effective emission area[38].

1.3 Field Emission Mechanism

Till date, most of the experimental efforts and theoretical works on the possible applications and the physical mechanism of cold field emitters (CFE) have been concentrated on one-dimensional structures, such as CNTs and various nanowires. However, the CFE from two-dimensional structures should be worthy of a deep investigation. Since the experimental realization of the free-standing graphene [39], it has aroused great interest both in experimental and theoretical studies. It's one atom thick edge is a unique feature and of particular interest. Graphene has an excellent electrical conductivity, as an attractive CFE emitter should be. Several researchers have experimentally showed that graphene does exhibit unprecedented CFE characteristics, such as lower threshold field and larger field emission current density [14], [33]–[35]. Recently J. Liu et.al [37], have shown that graphene based single CFE can emit a very large current density of 10A/cm². However, much larger current density can be achieved by appropriate tuning of the geometry of a free standing graphene based film.

1.3.1 Fowler-Nordheim Model and Field

Enhancement

The Fowler-Nordheim (F-N) model explains the tunneling mechanism through a material and the corresponding current density of electrons emitted into vacuum [40]. The F-N model incorporate tunneling through a material, where the field emitter is assumed as a cloud of free electrons, and the potential barrier height is assumed not dependent on the applied voltage [41]. In reality, potential barrier is an amalgamation of the image and external force potential, However, for simplification, a more simplified model for the triangular barrier shows in figure 1.1, is used [41].

A simplified, but corrected, F-N equation for field emission current density is given here[42], and expressed as, $J = A(\beta E/\phi)^2 \exp(-(B\phi^{1.5})/\beta E) \dots$ (1.1). Here, J is current density in A/cm², A and B are constants of $1.54 \times 10^{-6} \text{ AV}^{-2} \text{ eV}$

and $6.83 \times 10^7 eV^{-3/2} Vcm^{-1}$, E & ϕ is the applied electric field & work function respectively, where β is field enhancement factor. The applied field is adjusted to compensate actual field on the sharp and continuous edge of graphene by introducing the field enhancement factor (β). Potential lines are concentrated at the area, where the radius of curvature is very small. These concentrated potential lines resulted in much larger localized electric field. The field enhancement factor considers the microscopic, enhanced field on top of the emitter tip. The applied field E can be simplified to the uniform field in-between two parallel electrodes and can be expressed as,

$$E=V/d \dots\dots\dots (1.2)$$

Here V is the applied voltage and d is the gap length between the electrodes. After the inclusion of field enhancement factor (β), the localized field, E_L may be expressed as,

$$E_L =E \times \beta \dots\dots\dots (1.3)$$

Field enhancement factor for electron field emitters has a broad range of obtained values ranging from 1000 to 8000 and sometimes as large as 26000 [3], [45]. However, there is few arguments about determining field enhancement and has been discussed thoroughly by G. Eda et.al [14], where the simplifications mentioned above is also included, considering the field enhancement factor, and calculating the current from current density by determining the effective emission area.

Current density development over the effective emission area for different known emitters are shown in figure 1.3.

1.4 Motivation

THz waves have found applications in numerous fields, such as physics, engineering, material science, chemistry and forensics. There is a new research potential area in biology and medicine; therefore, an exploration of the THz range is now-a-days a trend as well as a challenge in vacuum electron device (VED). THz spectrum region is a transition between electron device and optical device; and, the frequency ranges between 100 GHz to 10 THz is also known as the “THz gap” as shown in figure 1.5. This gap exists because until now there is a lack of devices which can produce THz waves. Today there are two basic methods by which THz waves are generated. The first method is by using solid-state electronics. As a general rule, the maximum achievable power from a solid state device has an inversely proportional relation with the square of the frequency. Therefore solid state devices are still unable to produce such a higher frequency with a significant power level [43], [44]. The second method is by optical generation such as free electron LASER, in which the device is bulky and expensive [45], [46]. Therefore, generation of high power THz wave till date is a challenging job to the researches. A significant progress in research in the THz region is due to the technological advancements over the last few decades [47]–[49]. Researchers around the world are working on a comparatively small and compact THz sources using vacuum technology [1], [50], [51]. Out of many requirements, one of the critical needs for these THz VED is of high current density electron beam $> 1000\text{A}/\text{cm}^2$ which can be generated from a high current density cathode capable of delivering $\sim 1000\text{A}/\text{cm}^2$ current density [52]. Another critical requirement is to ensure the emission uniformity from the cathode surface. However, producing such a uniform, high current density electron beam from a miniaturized size is left as a challenge.

A conventional thermionic cathode can produce a limited current density ($\sim 100\text{A}/\text{cm}^2$) where the new field emission sources (graphene,) are capable producing such a current density ($> 1000\text{A}/\text{cm}^2$).

In this thesis work we are motivated to design, fabricate and characterize a graphene based field emission cathode using chemical synthesis technology that can deliver current density greater than $1000\text{A}/\text{cm}^2$ for use in THz VED.

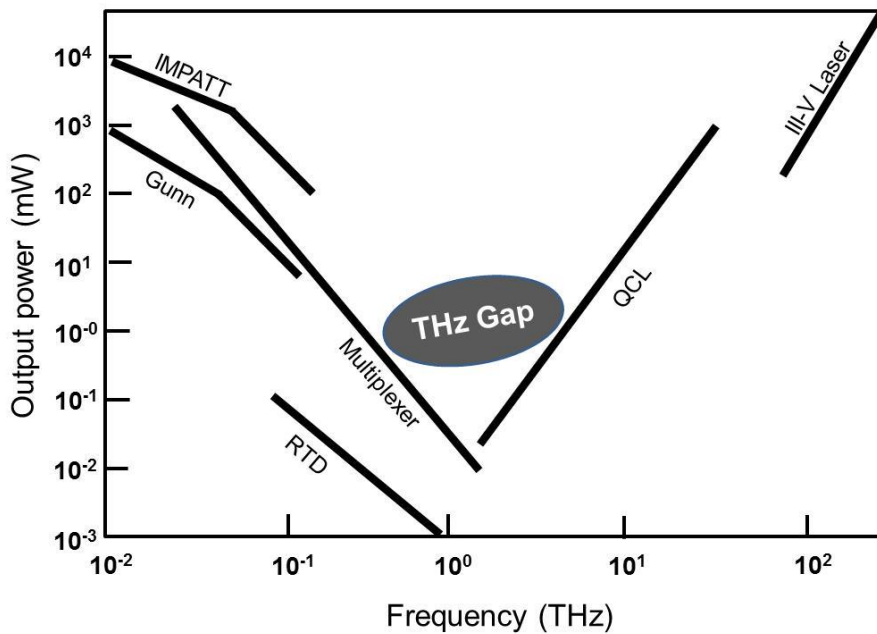
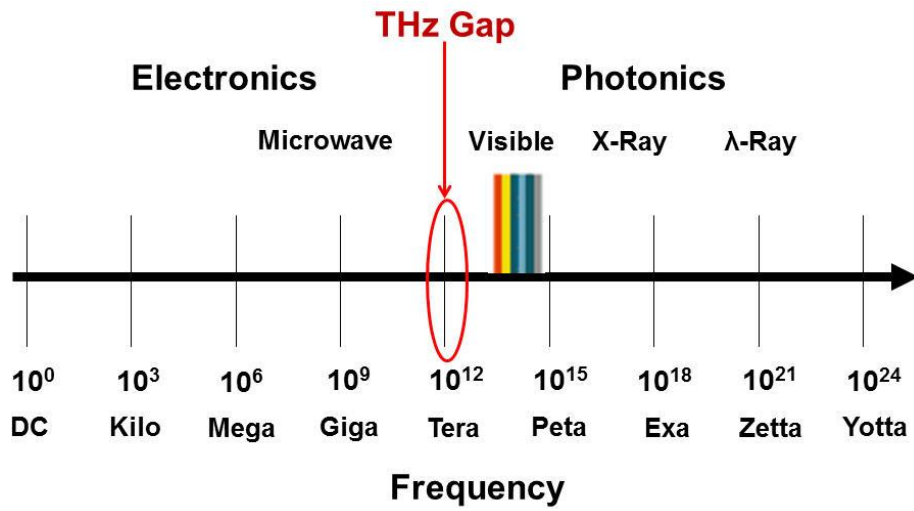


Figure 1.4: (a) EM spectrum (b) Available THz devices.

1.5 Goal

The field emission properties are affected by the emission area aspect ratio and its work function [35], [36], [53]. If the aspect ratio is large, field enhancement also will be large, therefore there will be a large current emission [54]. Similarly, a larger emission current can be obtained with same applied field, if the work function is lower [55]. However, because the thin nature, these films must have sufficient physical properties, such as large electrical conductivity to produce lesser joule heating due to drifting electrons, high thermal conductivity to dissipate heat efficiently, and stronger mechanical strength to handle the thermo-mechanical load during handling and field emission operation. To improve above mentioned properties, the improved/modified synthesis process also has an important part to play [56]. Therefore, synthesis of the large aspect ratio film with uniform thickness, homogeneously doped and improved physical properties are the crucial requirements for the realization of large current density field emission electron source for use in terahertz VED's. Our goal in this thesis is to develop graphene based metal doped field emitter cathode which can produce emission current density of 1000A/cm² or more with superior stability.

1.6 Organization of the Thesis

There are six chapters in this thesis which are organized as following:

- Chapter I is devoted to the introduction to the field emission. In this chapter an extensive survey of historical development of graphene field emission cathodes is also made. Finally, motivation and the goal of the research are mentioned.
- Chapter II contains various graphene synthesis process. Different issues regarding synthesis are addressed; and a choice of suitable synthesis process is mentioned from the application point of view.
- Chapter III provides a deep perception on the synthesis process of metal doped graphene based film using modified hummer method followed by an improvised hydrothermal technique. The techniques adopted and the results on the characterization of synthesized nanoparticles are also given.

- Chapter IV gives the experimental insight into the physical properties of graphene cathode.
- Chapter V describes the experimental work on the fabricated device towards achieving the objectives. The results on the characterization of after the experiment also presented.
- Chapter VI concludes the results of proposed research and discussed about the aspects of future work.

CHAPTER 2

Novel Synthesis Method for W-rGO Film

2.1 Previous Synthesis Methods

2.2 Requirements of Hybrid Film Parameters

2.4 Choice of Synthesis Process for W-rGO Film

2.1 Previous Synthesis Methods

There are many different approaches of graphene synthesis [57]. The synthesis process may be categorized into top-down [58] and bottom-up [59] approaches. For top-down approach, the source material is reduced from bulk size to nano-scale e.g., mechanical & chemical exfoliation and chemical synthesis where graphite is first oxidized then reduced. Bottom-up processes can be further subcategorized into Chemical vapor deposition (CVD), epitaxial growth etc. A general classification of nanoparticle synthesis is given in figure 2.1.

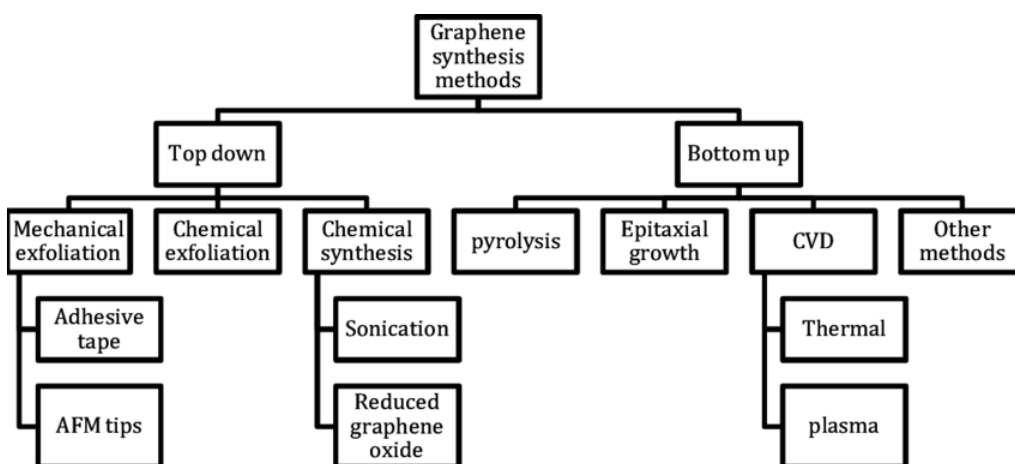


Figure 2.1: General classification of graphene synthesis approach.

Synthesis of pure graphene and functionalized graphene has been widely studied in past few years due to its potential application in critical areas. As a multifunctional material with unmatched thermo-electrical conductivity and equally outstanding mechanical properties, graphene has an immense number of applications, such as gas sensors, transistors, highly efficient filter membrane, field emitters etc. Several methods have been developed over the past few years for the large scale synthesis of graphene and functionalized graphene which is called graphene oxide (GO) [60]. Among them some processes are widely used such as chemical vapor deposition [61]–[63], epitaxial growth [64]–[66], pyrolysis method [67]–[69], chemical exfoliation [70]–[72], mechanical exfoliation [73]–[75], chemical synthesis [76], [77] etc. However, most of the process like CVD, epitaxial growth is unable to produce large scale free standing films, which is mandatory requirement for a field emitter.

Chemical synthesis methods, such as solvo-thermal method [78], [79], modified hummers methods [80]–[82], followed by a vacuum assisted filtration [83], [84] or hydrothermal methods [85]–[89] are easy to control film parameters.

2.2 Requirements of Hybrid Film Parameters

It has been prevailed that: (a) the field emission current density from the edge of a free standing film increases with larger aspect ratio [37]; (b) stability increase with improved physical properties [34], which in turn reduce joule heating, efficiently

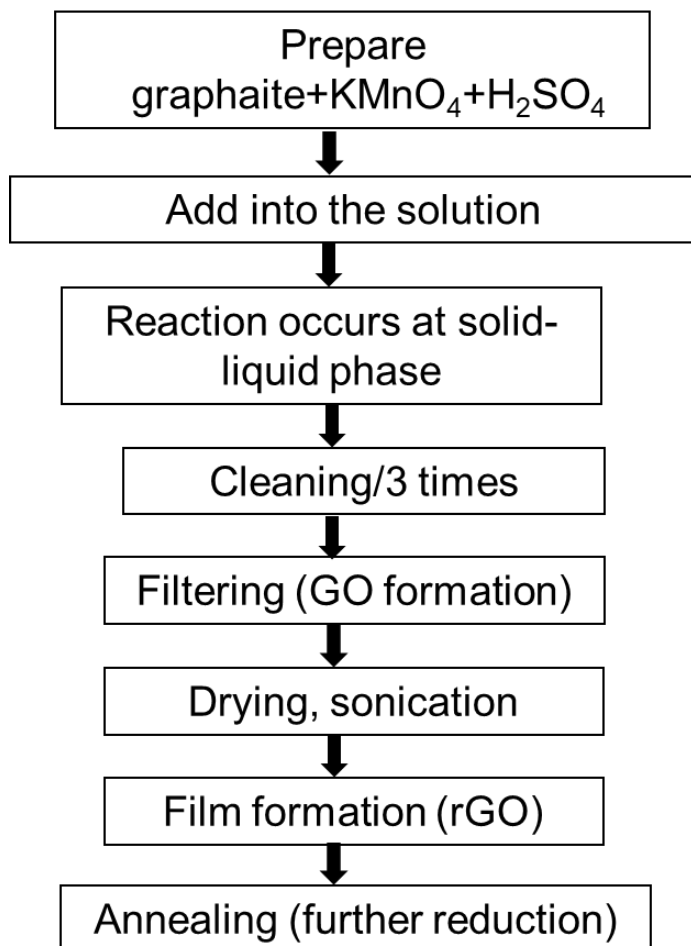


Figure 2.2: Common synthesis approach for rGO.

dissipate the generated heat and provide mechanical stability during field emission operation [90]; and (c) the emission current density increases if work function is tuned [91]. Therefore, the synthesis of a large aspect ratio film with thin and uniform edge, homogeneously doped for improved physical properties, and free standing in nature are the crucial requirements regarding the realization of high current density field emitter cathode for THz range VED's. Our aim in this section is to develop an easy, reproducible synthesis process addressing these issues in the development of tungsten doped rGO, free standing thin film for cathode applications.

2.3 Choice of Synthesis Process for W-rGO Film

A considerable amount of research is going on to synthesize metal doped contamination free-standing rGO films with controlled sizes and morphologies [56], [68], [90], [92]. Different approaches, including chemical, and physical methods, have been adopted for this purpose. However, there is no general strategy to create homogeneous metal doped films with a large aspect ratio, highly thermo-electrically conductive & mechanically stable and uniform size distribution. For the preparation of metal doped rGO, bulk quantities of GO are required. So, for the synthesis of doped graphene system, in most of the cases, chemical approach has been used. Different architectures of doped graphene can be obtained using the one-pot synthesis method [93]. However, in this process, for most of the cases, doping does not take place, thus make those films unstable during treatment [94]. In another approach to synthesize of graphene-nano particle composites, graphene or nano-particles could be chemically functionalized firstly and then nan-particles could be conjugated to the graphene surface by covalent or noncovalent interaction [95], [96]. But those methods often fail to form a covalent bond. Recently Zhen Xu et al. [90] adopted a novel synthesis process consisting of Hummers method [97], followed by a low temperature mixing with silver nano-wire dispersions in room environment. Initially they prepared graphene oxide by Hummers method. Then they doped graphene oxide solution with silver nano-wire dispersed in dimethylformamide (DMF). However, in this process the doping rate is poor as silver nano-wires does

not form ions. However, this process appears to be rather cumbersome, motivating us to suggest here a simple method of synthesizing W-rGO thin film using novel *sol-sol mixing* process. Also we choose tungsten as dopant material based on its superior thermo-electro-mechanical properties compared to rather common metal dopants [92] for rGO. In this work, tungsten doped reduced graphene have been synthesized by preparing graphene oxide by a modified Hummers method followed by an sol-sol mixing of GO solution and Tungsten oxide solution and finally doping of tungsten & film formation using a *modified* hydrothermal method [98]–[101], which is developed in our laboratory. It was found that the film thickness can be easily controlled and morphology of the film is sheet in nature since the source is in solution form. At the same time tungsten mixed homogeneously with graphene oxide solution which is responsible for the doping uniformity. We have synthesized thin (a few hundred nm) free-standing rGO and W-rGO films to compare, and found that W-rGO films have superior field emission capability and can produce comparatively high current densities with superior stability during continuous operation, making them reliable electron sources for terahertz vacuum electron devices.

◆ Main material: evaporation Joule's heating Heat dissipation Bending

	Melting point	Electrical conductivity	Thermal conductivity	Tensile strength
rGO	~1000 °C	~10 ⁵	~60 W/mK	500 MPa

◆ Possible composites:

Metal	Melting point	Electrical conductivity	Thermal conductivity	Tensile strength
Titanium	1650°C	~10 ⁶ S/m	~20 W/mK	250 MPa
Gold	1050°C	~10 ⁷ S/m	~300 W/mK	120 MPa
Silver	961°C	~10 ⁷ S/m	~400 W/mK	125 MPa
Tungsten	3422°C	~10⁷ S/m	~150 W/mK	941 MPa

Figure 2.3: Comparison of physical properties of tungsten with other dopants.

CHAPTER 3

Synthesis and Structural Characterization of W-rGO Film

3.1 Synthesis of W-rGO Film

3.2 Structural Characterizations

3.2.1 Characterization of Morphology

3.2.2 Characterization of Doping Homogeneity

3.2.3 Raman Spectroscopy

3.2.4 X-ray Diffraction Spectroscopy

3.2.5 X-ray Photoelectron Spectroscopy

3.1 Synthesis of W-rGO Film

A schematic flow diagram of the tungsten-doped rGO film synthesis is shown in figure 3.1. Graphite Powder (grade Sp-1) was purchased from Baycarbon Inc. (Bay city, Michigan, USA) and Tungsten Oxide ($\text{WO}_{2.9}$) from Sigma Aldrich. The other materials, those are, potassium permanganate (KMnO_4), sulfuric acid (H_2SO_4), hydrogen peroxide (H_2O_2), and ammonium hydroxide (NH_4OH) were purchased from Daejung chemicals (South Korea). De-ionized water (resistivity > \$18 \text{ M}\Omega\$) was used during the synthesis process.

Graphene oxide was synthesized using modified hummer method. 0.3gm of graphite powder was mixed with 1.8gm of KMnO_4 and 40 ml of H_2SO_4 was added and the solution was mixed in glass bottle. The bottle was then transferred to a rotating (950 rpm) heating mantle and was mixed for 6 hr at 45°C . The solution then neutralized using DI water. After that, 2 liter of DI water was added for washing and cleaning the solution along with a 40ml of H_2O_2 for the sedimentation. The solution was left to clean the chemical residues for 6 more days. During this period, DI water was changed in every 24 hours. The solution is then filtered using a vacuum filter and a buckypaper/GO cake was obtained. The cake (Figure 3.2(a)) was dried out for 24 hours in vacuum environment inside a custom made vacuum chamber (Figure 3.2(b)). After the drying process, sonication bath was used for 6 hours to make the GO-water solution. 0.038 gm of WO_3 (nano-particle form) was dissolved into 0.5 ml of NH_4OH solution to create a liquid form. At the start of the sonication process, this liquid was mixed with the GO solution, which significantly improved the mixing rate and the homogeneity of the solution. WO_3 nano-particle has been prepared using a novel technique [102]. This well prepared WO_3 has been proved to very advantageous for us, as they got dissolved in the NH_4OH with a fast rate and homogeneously, and also due the nano form, the required volume of NH_4OH was very less (<0.5 ml for 0.038 gm), which helped us to keep the pH of the solution unchanged. The well mixed solution was used to synthesize thin films (few hundreds of nm thickness) by a modified hydrothermal method developed in our laboratory. An in-house developed hydrothermal vessel (figure 3.3) was used for this purpose. Film thickness was controlled by controlling the amount solution. For further

reduction, prepared film was annealed inside a vacuum furnace at 1200°C in Nitrogen environment. For comparison, rGO film with similar synthesis process was also synthesized, but without tungsten doping. However, after annealing in 1200°C temperature, film become completely evaporated, thus we have obtained rGO films annealed only up-to 1000°C for comparison. Both films are then cut into shape by microtome technique and characterized using FESEM, Raman spectroscopy, XRD, and XPS.

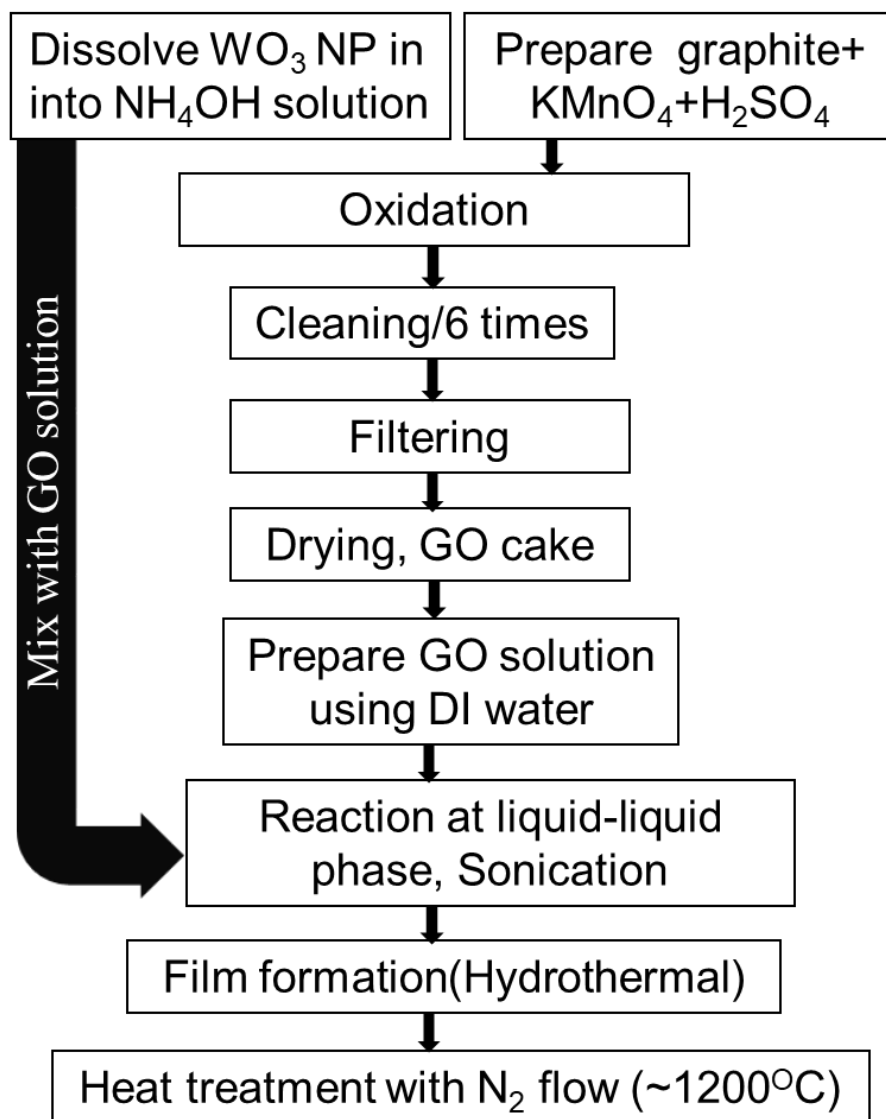


Figure 3.1: Flow diagram of the synthesis process to prepare W-rGO films.

3.2 Experimental Characterizations

Several characterization tools were utilized to determine the film thickness, morphology, elemental composition, carbon network purity, reduction of oxygen functional groups of the synthesized film. The size, doping status and status of carbon network of the film were carefully examined at room temperature condition by FESEM & Energy dispersive X-ray spectroscopy (EDS), Raman spectroscopy, and High-resolution X-ray diffraction (XRD) system comprised of Cu-K α radiation. The XRD analysis was carried out over the 2θ range of 10° to 80° . The morphology and elemental analysis of the films were examined using an X-ray photoelectron spectroscopy (XPS). The samples for the analysis were prepared by shaping the synthesized films into large rectangular shape.

3.2.1 Characterization of Morphology

The microstructures and the thickness of as prepared rGO and W-rGO was characterized using an FE-SEM (SUPRA). The schematic diagram of FE-SEM shown in figure 3.4.

Figure 3.5 shows the FE-SEM image of films. As it is clearly visible, both film have a thickness ~ 100 nm. However, W-rGO film (Figure 3.5 (c)&(d)) show more compactness near to the edge also, compare to as-prepared rGO (Figure 3.5 (a)&(b)). Figure 3.5(e,f,g) show the rGO film in case of as-prepared, annealed in 800°C and 1000°C respectively, where (h,i,k) is for W-rGO films, for as-prepared, 800°C and 1200°C respectively. It can be depicted clearly that the W-rGO films show much more structure integrity compared to as-prepared rGO films, where edges of the films annealed in higher temperature can be seen clearly exfoliated. With a larger temperature (1000°C) physical damage was occurred and edges of the film was broken. However, W-rGO films retained their structure even on edges with almost no exfoliation under a very high annealing temperature (1200°C). This phenomenon clearly suggests that the W-rGO films have a superior structural integrity over as-prepared rGO films.



Figure 3.2: (a) Bucky paper (b) Custom made drying chamber for buckypaper.

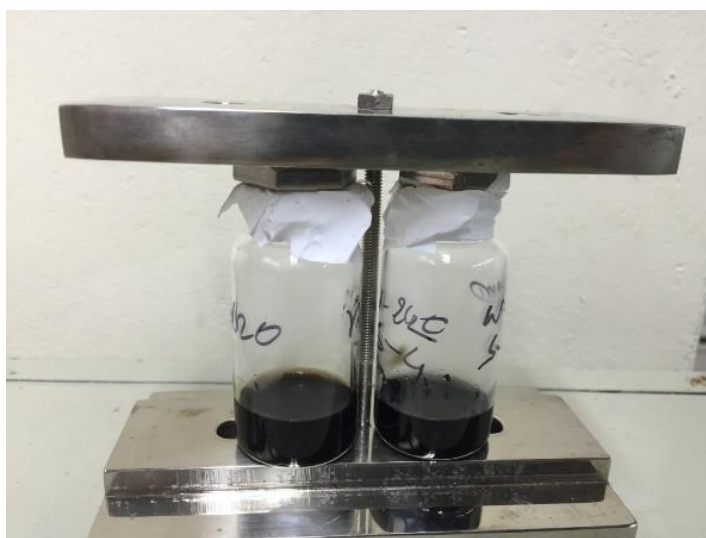


Figure 3.3: In-house developed hydrothermal vessel.

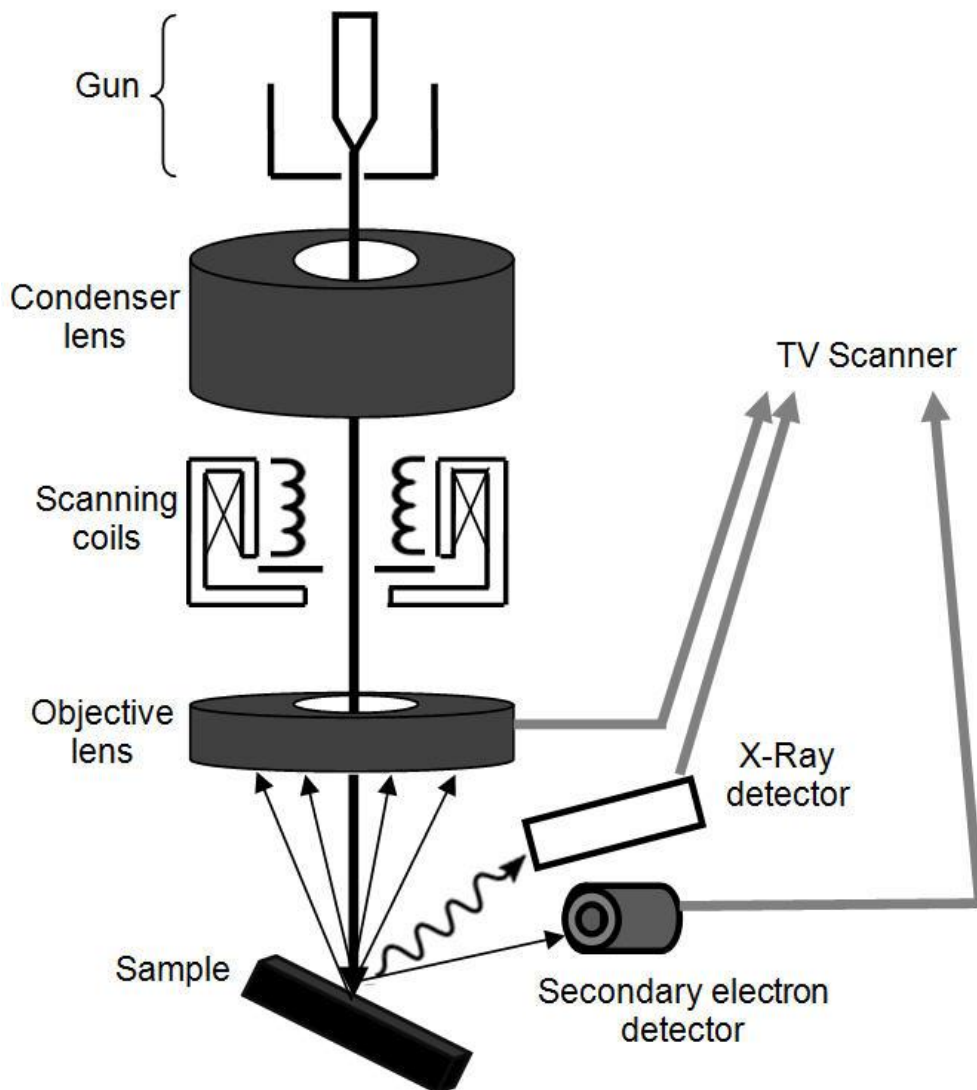


Figure 3.4: Schematic diagram of Field Emission Scanning Electron Microscope.

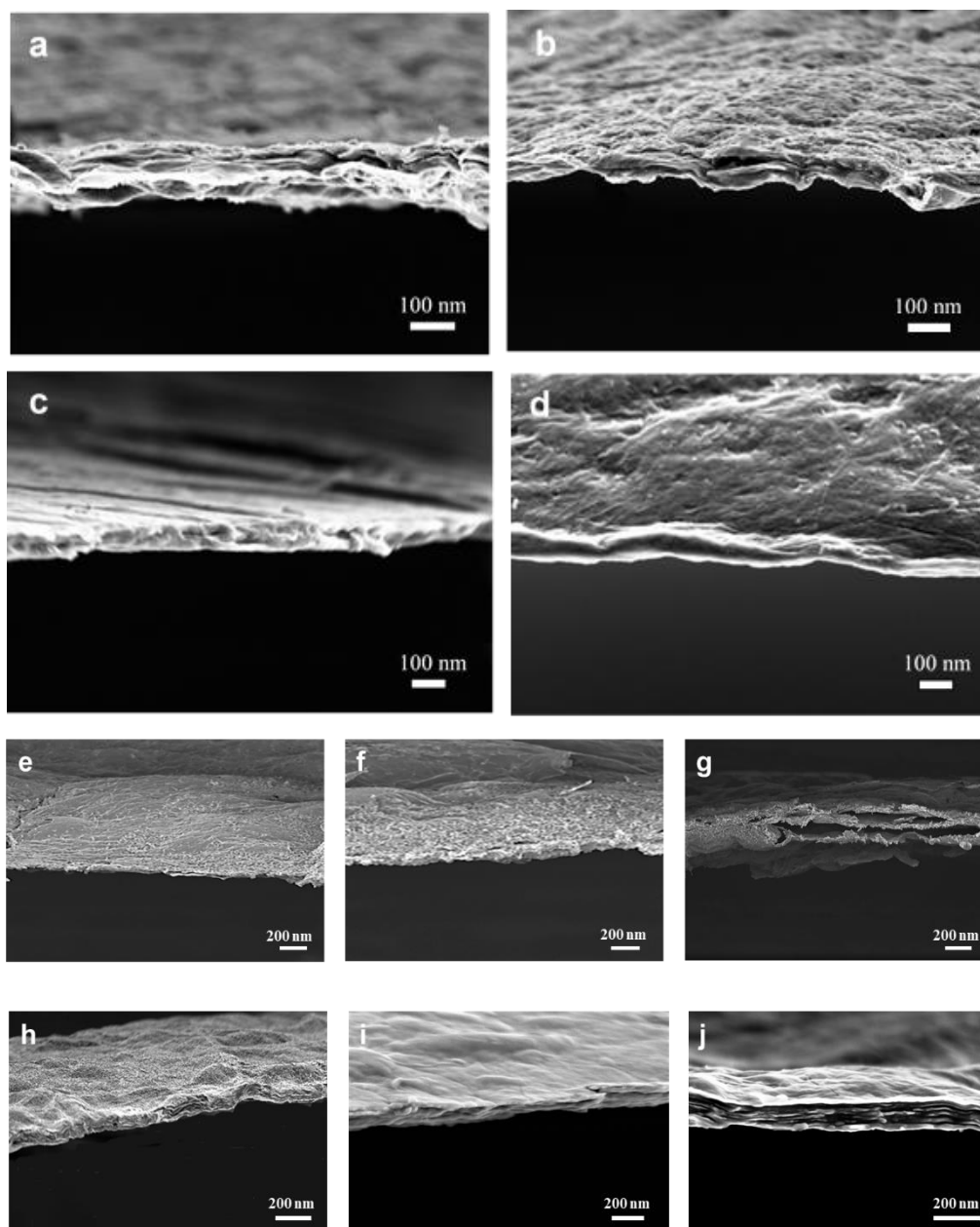


Figure 3.5: Morphology of rGO and W-rGO obtained from FE-SEM. (a) Thin edge (100 nm~200 nm) and (b) Surface images shows the exfoliation of rGO. (c) Thin edge (100 nm~200 nm) and (d) Surface images shows the tightly bounded edges of W-rGO. After annealing at different temperature. (e), (f) and (g) are rGO films with as-prepared, 800°C and 1000 °C annealed. (h), (i) and (j) are W- rGO films with as-prepared, 800°C and 1200 °C annealed.

3.2.2 Characterization of Doping Homogeneity

An EDS spectroscopy combined with the FE-SEM device was used to analyze the doped films, in spot size dimension of 50 μm . Figure 3.7(a)–(d) shows the EDS spectrum of two films taken from two different locations in each case (figure 3.6). Only carbon & oxygen for rGO films and carbon, tungsten & oxygen data is shown here, although detected contaminations were more. Practically, Mn, S, K, and N elements were also detected by the EDS analysis, where these elements originate during the synthesis process. The trace of the element tungsten confirms that W-rGO films are doped with tungsten. Table 3.1 represents the percentage in terms of the weights and atomic concentrations of the carbon, oxygen and tungsten elements as evaluated from the EDS measurements. From figure 3.7 and Table 3.1, one can infer that the reduction of oxygen and insertion of tungsten.

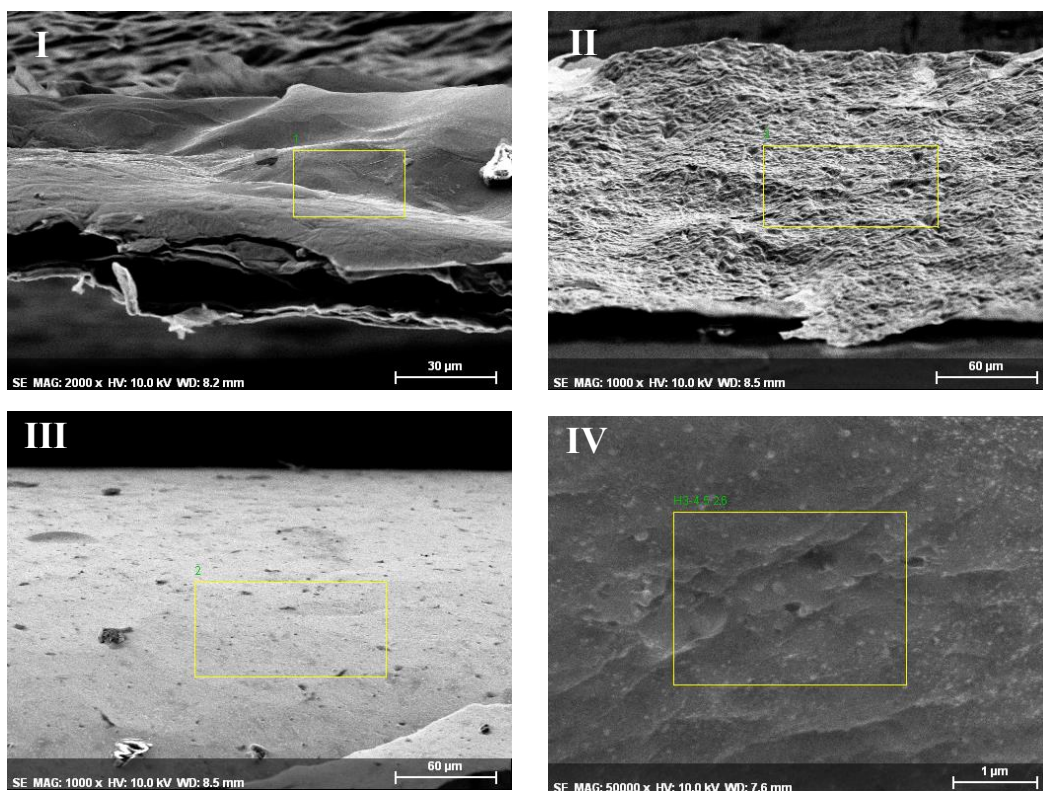


Figure 3.6: SEM image taken during the EDS analysis, indicating four locations on rGO film(I, II) and W-rGO films(III, IV), from where EDS spectra was taken.

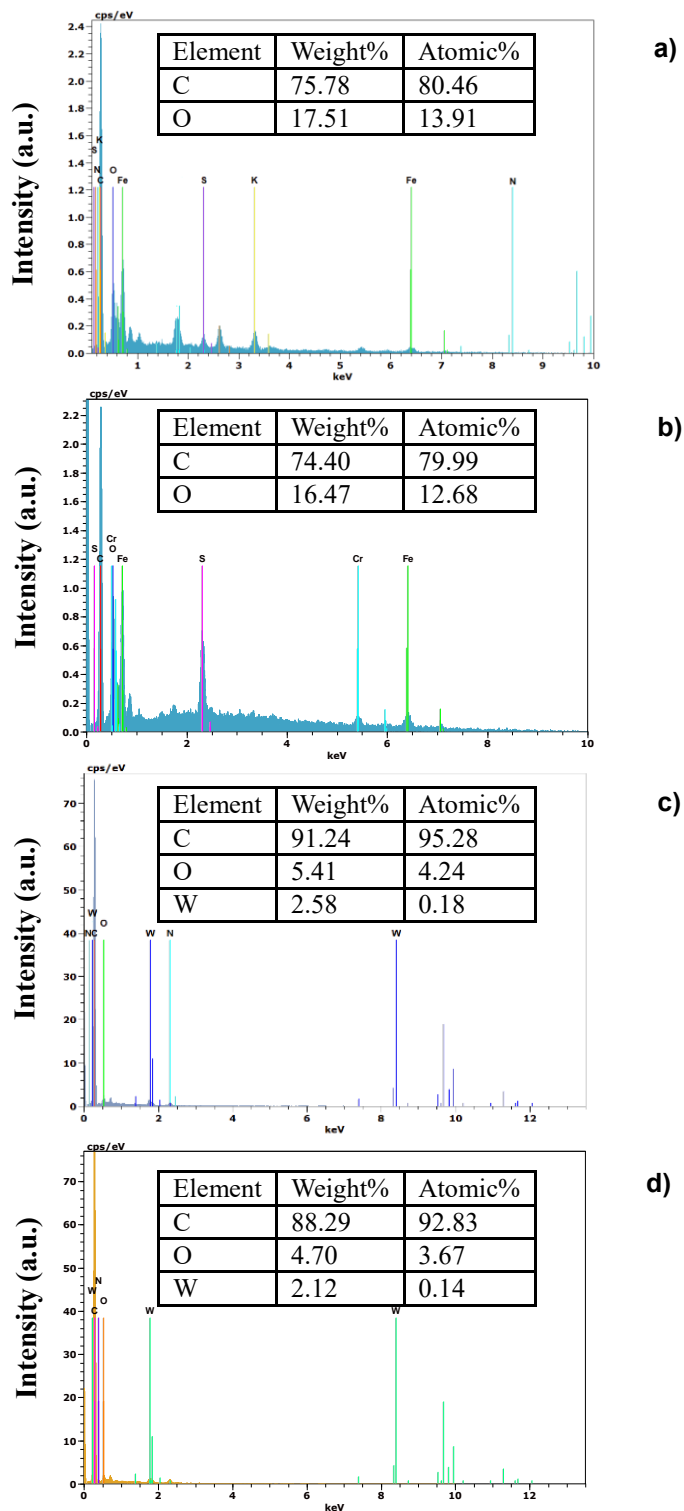


Figure 3.7: EDS spectra taken at (a) location I, (b) location II, (c) location III and (d) location IV.

Table 3.1 EDS Analysis of rGO and W-rGO films.

Figure		Element		
		Tungsten	Carbon	Oxygen
a	Weight %	-	75.78	17.51
	Atomic %	-	80.46	13.91
b	Weight %	-	74.40	16.47
	Atomic %	-	79.99	12.68
c	Weight %	2.58	91.24	5.48
	Atomic %	0.18	95.28	4.24
d	Weight %	86.08	0.14	4.70
	Atomic %	53.42	2.12	3.67

3.2.3 Raman Spectroscopy

The defect distribution and intact sp² bonded carbon network inside the film structure was determined using the Raman spectroscopy [103]. Analysis was carried out in a Raman spectroscope (LabRAM HV Evolution, Horiba, Japan) with a laser frequency of 532nm. A schematic diagram of a typical Raman spectroscope is depicted in figure 3.8.

Raman spectroscopy yields information about vibrations in molecules inside a samples. Those information is used for determining the molecular structure. This method involves exposing the sample under a monochromatic light, for an example, laser, and the detection of the light dispersion. Most part of the scattered light is of the identical frequency as the excitation source, alternatively knows as Rayleigh scattering. However, a very small portion of the scattered light (example. 10⁻⁵% of the intensity of incident light) is shifted from the excitation frequency. Because of the interaction between incident light and vibrational energy level in the sample, the shit scattered light takes place. Plotting of this shifted light intensity vs. frequency is interpreted as Raman spectrum. Most common cases, Raman spectra are plotted in compliance with the laser wavelength such a way that the Rayleigh band remain at 0 cm⁻¹. On this scale, the band position will remain at energy levels corresponding to the frequencies of vibration from different functional groups. Thus, the Raman spectroscopy can be interpreted likewise the infrared absorption spectroscopy.

The Raman spectrum of graphene and related materials [104] exhibit a relatively simple structural characteristics by three primary bands namely the G, D and 2D bands which appears around 1600cm⁻¹, 1350cm⁻¹ and 2700cm⁻¹ respectively. Note that the D band (mainly in case of GO or rGO) appears when defects within the graphene lattice are present. Although they appear subtle, these differences provide very crucial information when analyzed closely. In case of G & D bands, significant differences in band positions and intensity can be observed. Evidently, these Raman spectrums can be utilized to differentiate between single & multi-layer graphene, GO, rGO and graphite. However, the most significant advantage of Raman spectroscopy is hidden inside the ability to differentiate single, double, and multi layers of graphene. In simple word, Raman spectroscopy has the ability to determine layer

thickness at an atomic level resolution of less than four layers and in case of functionalized graphene (GO or rGO), it can determine the degree of defect present in the carbon network (sp^2 bonds).

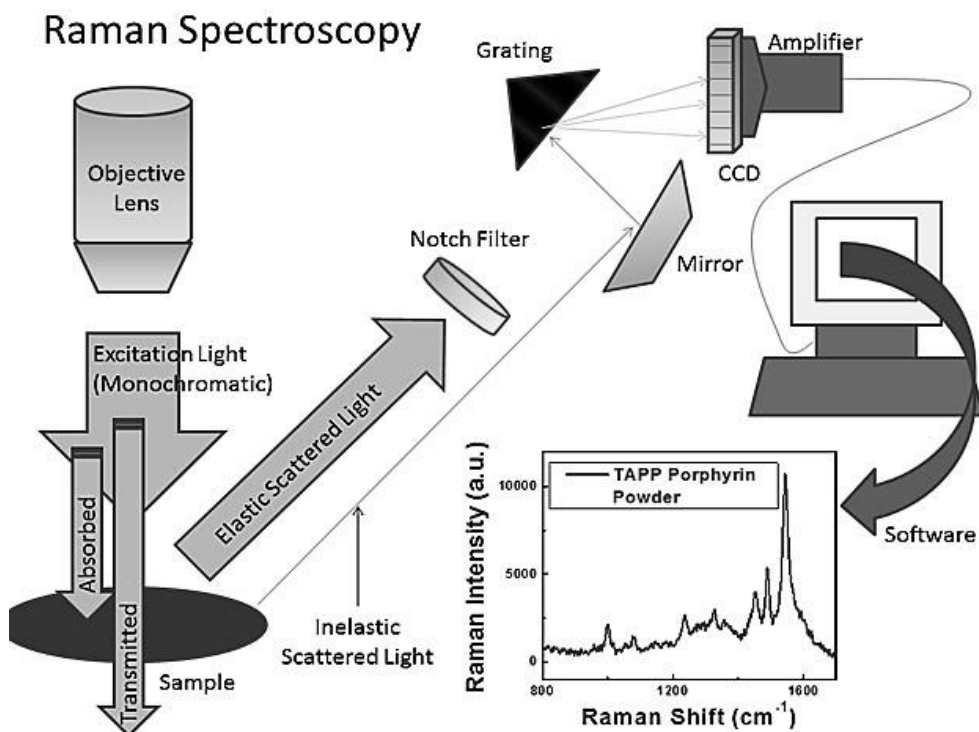


Figure 3.8: Schematic diagram of Raman spectrometer.

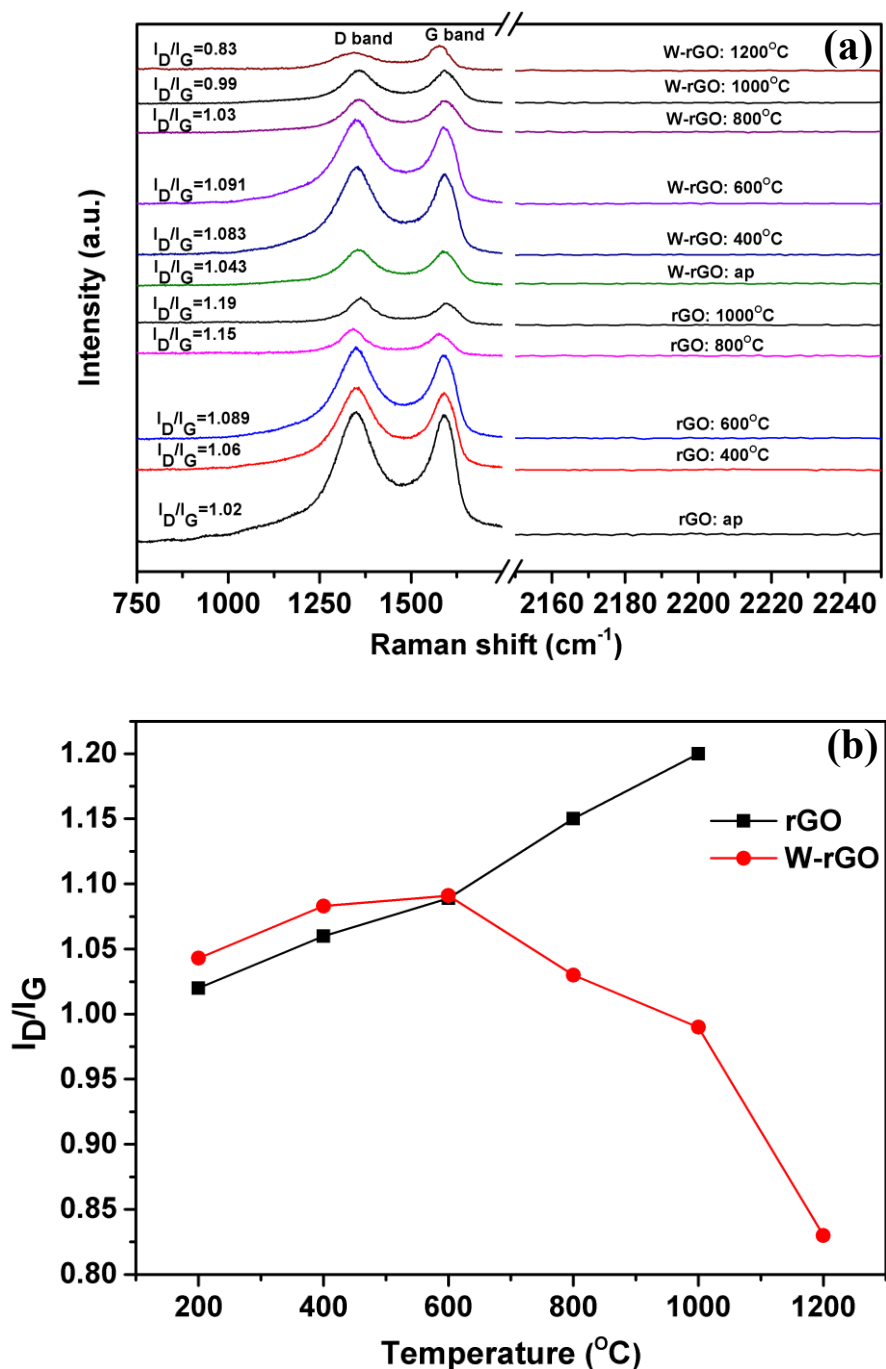


Figure 3.9: (a) Raman spectra of the synthesized rGO and W-rGO films annealed different reduction temperatures, that is 400 $^{\circ}\text{C}$, 600 $^{\circ}\text{C}$, 800 $^{\circ}\text{C}$, 1000 $^{\circ}\text{C}$ and 1200 $^{\circ}\text{C}$. (b) I_D/I_G curve showing that the restoration of sp^2 network with increased annealing temperature.

In this thesis, Raman spectroscopy was utilized to study the changes in carbon network for both, rGO and W-rGO film, annealed in different temperatures. Compared to the rGO film (figure 3.9(a)), the G peak of the W-rGO film associated with the sp² domain of carbon (1600 cm⁻¹) is noticeably increased and the D peak corresponding to defect in sp² domain of carbon (1350 cm⁻¹) reduced significantly. From the figure 3.9(b), it is clearly visible that the I_D/I_G ratio in rGO film increase with temperature, which indicates that the defect is also increased with annealing temperature as a result of evaporation of carbon along with the removal of oxygen functional groups. However, for W-rGO films, it was observed that, upto 600°C, the I_D/I_G ratio was increased, but after that it start to decrease and at 1200°C, I_D/I_G was ~0.83 which is quite low. This phenomenon indicated that the after 600°C, tungsten starts to dope inside the film, and as annealing temperature go up, doping rate also increased. This phenomenon is the result of doping of tungsten where due to strong covalent bond between carbon and tungsten, evaporation of carbon is restricted.

3.2.4 X-ray Diffraction Spectroscopy

The phase characterization assessment was carried out using a XRD (Smart Lab, Rigaku, Japan) device. A schematic diagram of XRD is shown in figure 3.10. The diffraction patterns were collected from 10° - 80° at a scan rate of 0.01° per step and at 10 second per point. Figure 3.11(a)–(d) shows typical XRD patterns of the films. The peak at 23.5° claims reduction and peaks at 31.4° denotes the W-C bond, where tungsten is doped inside the film and the forms a covalent bond.

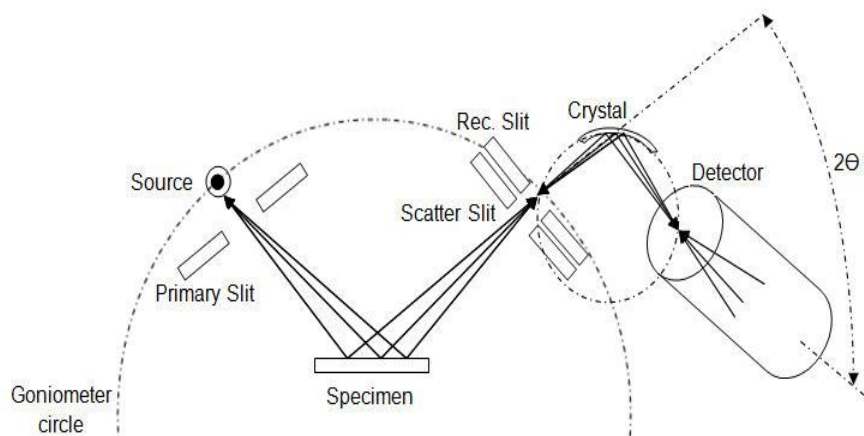


Figure3.10: Schematic diagram of Scanning X-ray diffractometer.

$$\lambda=2d\sin(\Theta)\dots\dots\dots (3.1)$$

The layer spacing (spacing) could be calculated with the aid of Bragg equation (eq. 3.1) [105]: where λ is represented the X-ray beam wavelength ($\lambda= 0.154\text{nm}$), d is the gap between the GO or rGO adjacent sheets, and Θ is the diffraction angle. From the equation (3.1), it can be rearranged like the following that,

$$d=\lambda/2 \sin(\Theta)=0.154\text{nm}/2\sin(\Theta) \dots\dots\dots (3.2)$$

Using the equation (3.2), and the 2Θ data from XRD analysis, layer distance can be calculated with ease. In general, XRD pattern of rGO exhibits a diffraction peak at

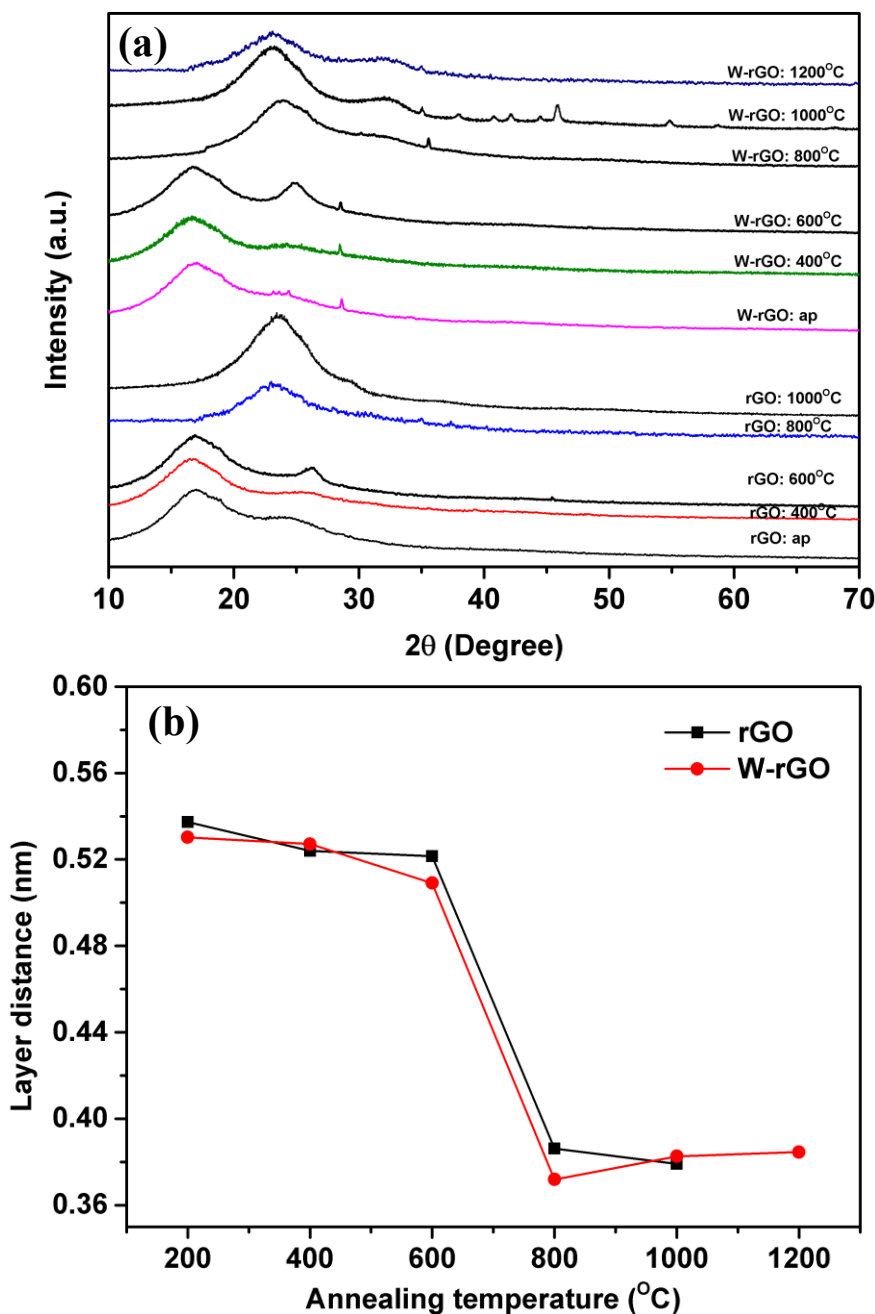


Figure 3.11. (a) XRD spectra and (b) interlayer distance shows that the interlayer distance reduces with annealing temperature. Interestingly, for the W-rGO annealed at 1200°C, it can be observed that the interlayer distance increased. We assume that this phenomenon took place because of the doping of large number of tungsten atom to repair broken carbon network.

26.1°. Diffraction peak become much broad in case expanded pattern of Graphene oxide at 17.1°. the significant increase in spacing is due to the oxygen functional groups intercalated in between layers of graphene oxide. The XRD pattern of rGO and W-rGO composites collected is presented in Figure 3.11(a). The narrow diffraction peak from W-rGO for the annealing temperature of 1200°C, which is centred around 23.5°, belongs to the (002) plane of the graphene. For W-rGO films, after the annealing temperature of 600°C, few low intensity peaks are clearly visible. Those peaks belong to the reflections from (100) planes of typical tungsten. From the XRD pattern, it can be inferred that samples are highly crystallized. The presence of the diffraction peak at 31° confirms that the WC bond is formed, and tungsten were successfully inserted into the rGO film. Absence of any other peaks from any impurities has confirmed the high purity of the fabricated film. With the annealing temperature, the layer distance reduces with removal of functional groups, which can be depicted from the Figure 3.11 (b). Interestingly, at annealing temperature of 1200°C, it can be observed that the layer distance increased compared to 800°C. This phenomenon can be interpreted as result of tungsten doping, where, because of larger molecular radius, tungsten increased the layer distance in W-rGO.

Table 3.2: Tungsten peak of the XRD spectrum corresponding to different annealing temperature for the W-rGO films.

Annealing temperature	C:W ratio	1st Peak	2nd Peak
400°C	0.00604	27.5	-
600°C	0.00844	27.8	-
800°C	0.01468	28.2	37
1000°C	0.017	29.2	36.5
1200°C	0.02266	32.6	36

Table 3.2 shows that annealing temperature increases the tungsten peak of XRD spectrum become prominent, which indicates the formation of a pure W-C bond. The annealing temperature can positively affect the doping rate and also can affect the doping strength, leading to the formation of large of C-W covalent bond. Therefore, the phase purity, bonding strength and doping concentration can be efficiently controlled by the means of the annealing temperature.

The standard peak belongs to (002) plane in graphene was appeared around $\sim 23.58^\circ$ after the high temperature annealing of both rGO and W-rGO at 800°C . After the high-temperature reduction, that typical peak becomes much thinner and sharper. Based on the position of the peak, inter layer distance between the rGO layers was calculated, which decreases from 0.369nm for 800°C annealing to 0.351nm for 1200°C annealing, for W-rGO film. Decrease in the observed layer gap, is the result of the efficient removal of oxygen functional groups in W-rGO film. It is evident that the layer gap is close to the value of graphite (~ 0.334 nm). Note that for W-rGO films, peaks around 31.4° denotes the (001) plane of WC. Which confirms the uniform doping of tungsten into the carbon network.

3.2.5 X-ray Photoelectron Spectroscopy

X-ray photo electron spectroscopy (XPS) [106] was utilized to find out the surface chemical state of both, rGO and W-rGO film samples, annealed in different temperatures. A schematic diagram of XPS is shown in figure 3.12. Analysis was performed in a XPS device (Sigma Probe, VG, UK) with X-ray energy upto 10keV. It can obtain the chemical data from the top 10nm of a material with a very high scanning resolution between three to few hundreds of μm . Sensitivity with a resolution of 0.1% can be obtained for elemental composition. $3\mu\text{m}$ angle resolved XPS can image surface chemical state, thickness and depth-distribution of chemical species Also thickness can be measured of overlayers of up to 8nm on a substrate. Depth profiling also can be carried out using an ion gun to clean outer plane. Density of state and work function can also be obtained using the ultraviolet photoelectron spectroscopy (UPS) device attached in the XPS system.

In XPS, the sample surface is illuminated with X-rays beam in high-vacuum condition. Upon hitting, X-ray beam energizes the core-level electron in the sample. That electron is escaped from the initial condition with an energy corresponding to the incident X-ray beam and binding energy of the atomic orbital from which it emerged. Energy and the intensity those escaped electrons are analyzed to identify and find out the concentrations of the elements present in the sample. Note that these photoelectrons originate from a depth of $<10\text{ nm}$.

Ultra violet photo electron spectroscopy (UPS) [107] operates with a low level energy source, He(I) and He(II), where the energy level is 21.2 eV and 40.8 eV respectively. UPS analysis can be used for determining work function, distinguishing and estimation of surface contamination of organic overlayers, that is to resolve the issues of sticking of coatings on substrates, analysis of nanoparticles, thickness measurement of semiconductors, classification of counterfeit goods, and characterization of a broad range of materials such as polymers, glasses, ceramics etc.

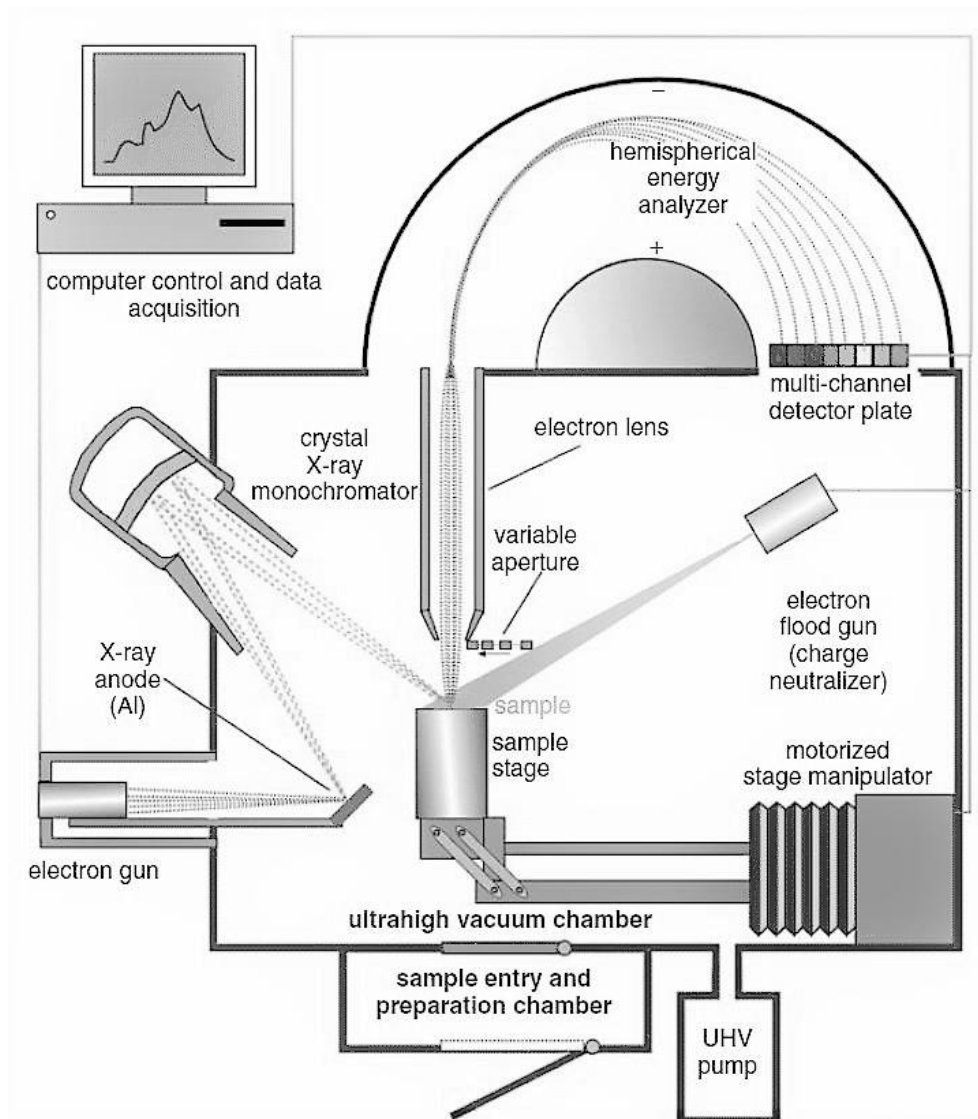


Figure 3.12: Schematic diagram of X-ray photo electron spectrometer.

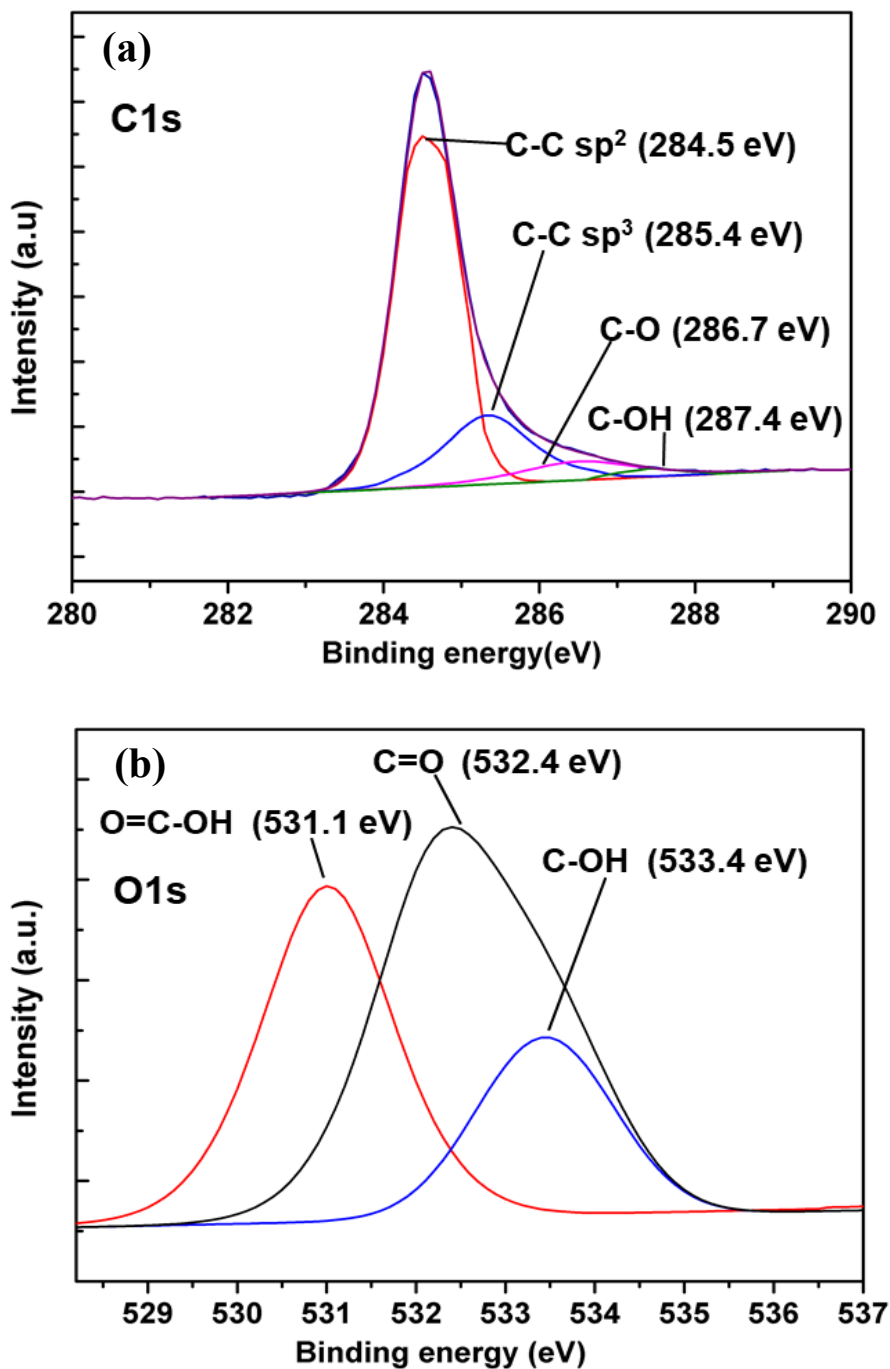


Figure 3.13: (a) C1s and (b) O1s for rGO film obtained from XPS, annealed at 800°C. We choose this temperature, as films annealed in this temperature is not physically damaged and usable for field emission experiment.

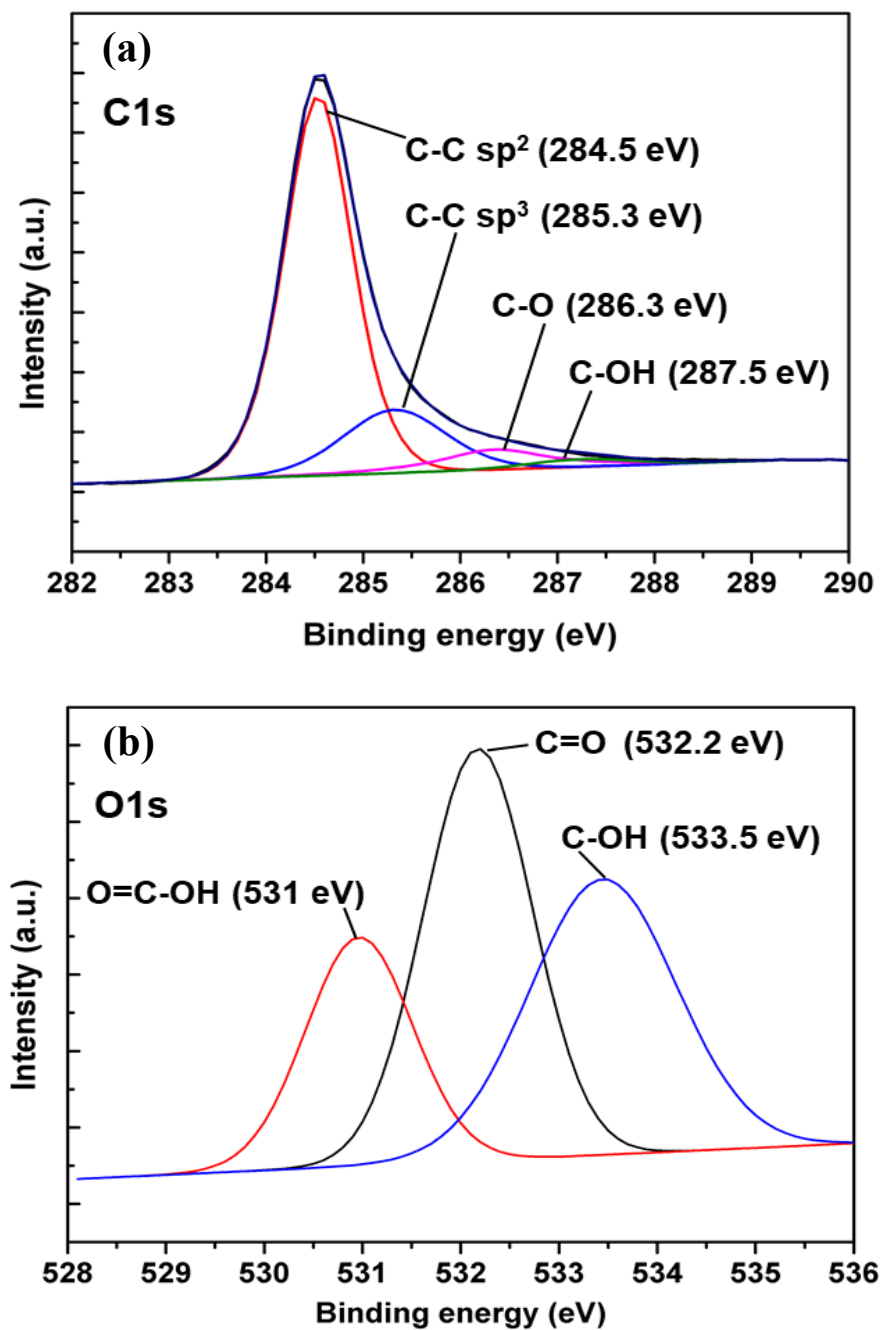


Figure 3.14: (a) C1s (b) O1s for W-rGO film obtained from XPS analysis, annealed at 1200 °C. We choose this temperature, as films annealed in this temperature is not physically damaged and usable for field emission experiment.

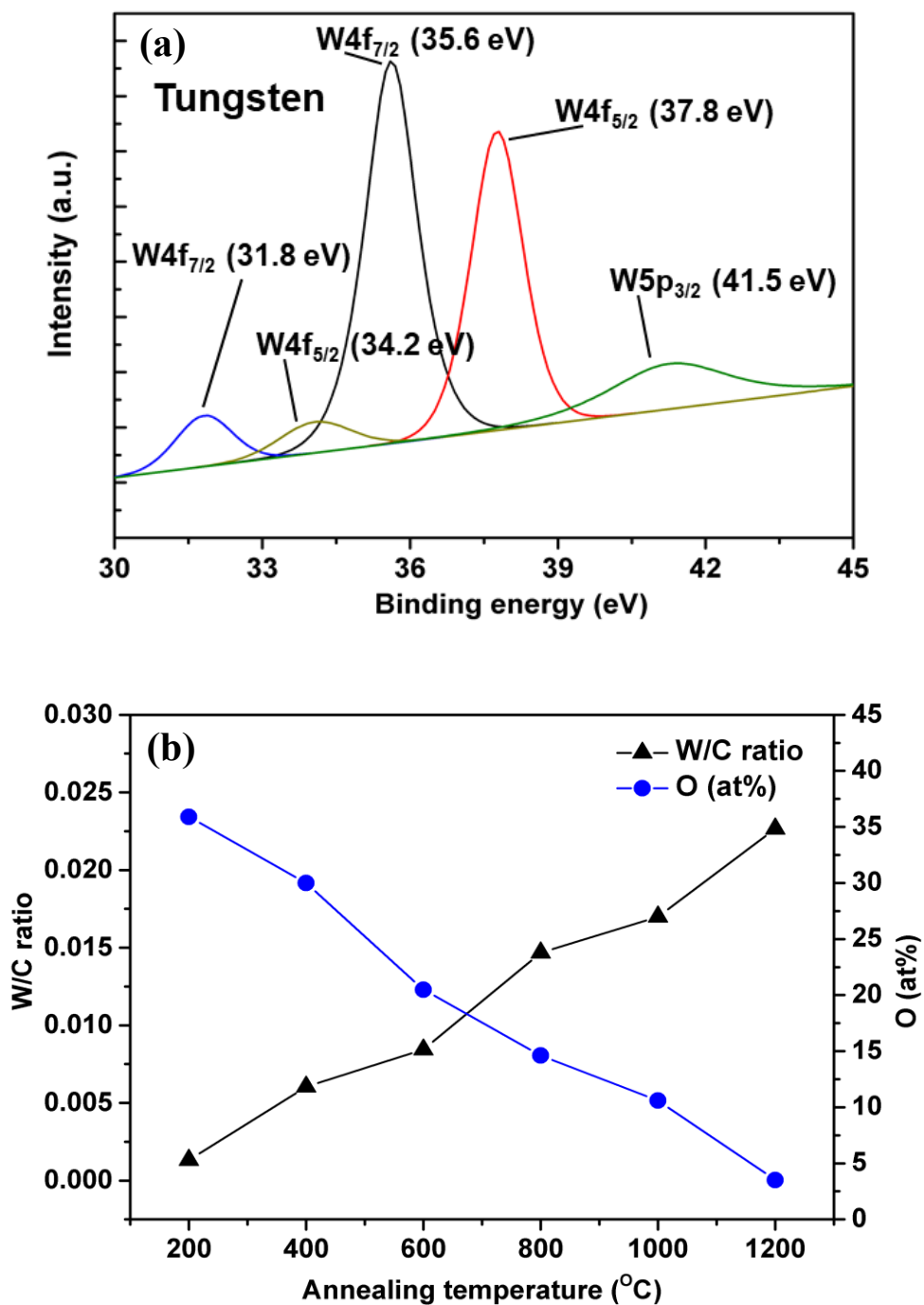


Figure 3.15: (a) XPS spectra for tungsten, (b) Oxygen at% & carbon to tungsten ratio as a function of annealing temperature.

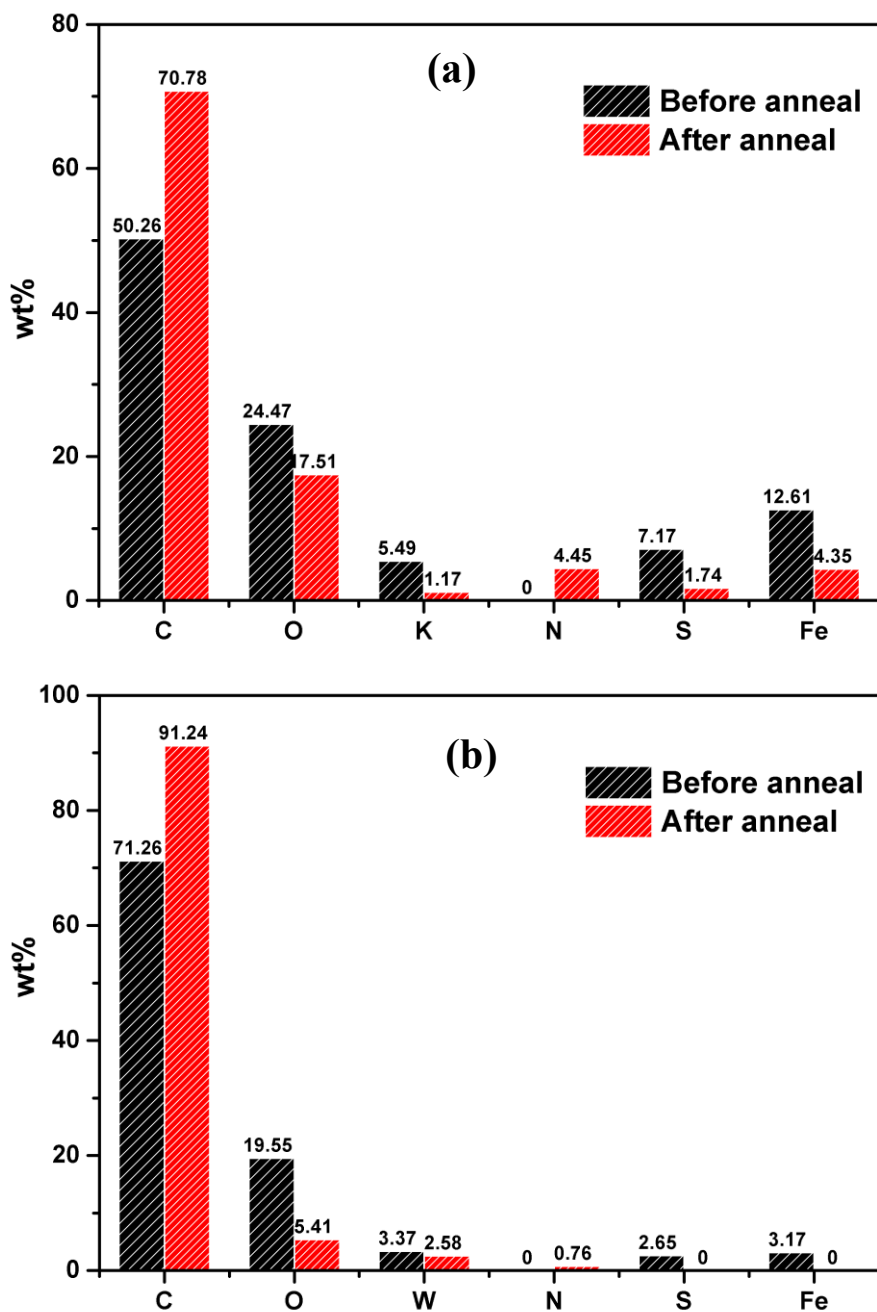


Figure 3.16: (a) wt% of elements present in as-prepared films and films after annealing at 800°C for rGO films, (b) wt% of elements present in as-prepared films and films after annealing at 1200°C for W-rGO films.

Further to analyze energy state, bonding and elemental presence, X-ray photo electron spectroscopy (XPS) analysis has been carried out. Five number of rGO samples (as-prepared, and annealed in 400°C, 600°C, 800°C & 1000°C), and six number of W-rGO (as-prepared, and annealed in 400°C, 600°C, 800°C, 1000°C & 1100°C) samples were used for the XPS analysis. rGO samples were completely evaporated during annealing process under 1200°C temperature, thus making itself unavailable for analysis. It can be seen from the XPS elemental analysis, (model: Sigma probe) that the W-rGO films annealed in 1200°C, maintained a ratio of ~1:0.01 for C:W at%. Presence of oxygen functional groups reduced significantly comparing to the films without the W doping, by more than 60%, which indicates a very large rate of improvement in carbon network. Further EDA data from FESEM (Model-Supra) also verifies the XPS data. To analyses further the surface chemical and bonding states of the rGO and W-rGO films, XPS scan was performed on a wide range of carbon & oxygen. The XPS spectrum confirms C, W and O appeared in the synthesized films. C1s and O1s is plotted in figure 3.13(a-b) and fig.3.14(a-b), for rGO and W-rGO films respectively. Five tungsten crystalline peaks have been found at 31.8eV, 34.2eV, 36.5eV, 37.7eV & 41.5eV and plotted in fig.3.15(a), which indicates the W-C bond (31.8eV & 34.2 eV) and tungsten cluster (36.5 eV & 37.7 eV) in W-W form. The peak at 41.5eV indicates the formation of a complex form of W⁶⁺ corresponding to the 5p₃ peak of tungsten is found often in tungsten based composites [108]. The binding energies obtained from XPS, corresponds to the C1s core level from the graphene plane, which can be fitted by the sp³-hybridized carbon atoms (centered at 285.3 eV) and the planar sp²-hybridized carbon atoms (centered at 284.6 eV). The peak of O1s are appeared at 531eV, 532.5 eV & 533.8 eV indicated that oxygen is from functional groups and the contamination of rGO. The C1s peak at 284.6 eV increased in intensity following high temperature reduction for both of the films. However, W-rGO shows a strong C1s peak with large intensity and lower intensity from oxygen groups (in O1s) compared to rGO. Those peaks indicating a large percentage of sp² hybridization and efficient reduction in oxygen groups in W-rGO. Further to support this phenomena, C:W ratio and oxygen at% as a function of annealing temperature was plotted and shown in figure 3.15(b). It is clearly visible from the graph that, with increasing temperature, oxygen at% is reduced significantly,

however carbon at% reduced nominally. Similarly, for the case of rGO, it is also clear that, with temperature, carbon network improves and oxygen groups decreases. However, the intensity of C1s core level is much smaller compared to other conjugate groups, which depicts that reduction is not efficient and still a large number of oxygen groups are present inside. This phenomenon can be attributed the doping of tungsten, which replaced the oxygen groups and repaired broken carbon network, thus reducing the carbon loss during annealing process. The O1s peak at 532.8eV is appeared for both the samples. However, we see significant decrease in the peak of 532.8eV, which indicates the significant removal of oxygen from the rGO and W-rGO samples after thermal reduction. Elemental analysis shows the change in wt% of elements present in both of the films for the case of before and after reduction. Figure 3.16 (a) shows that carbon at% increased from ~51% to ~71% in rGO films where O% reduces from 24% to 17%. Similarly, for W-rGO it is found (figure 3.16(b)) that C% increased from 71% to 91% and O% reduces from 19% to 5%. This analyses supported the statement that doping of tungsten replace the oxygen groups and repair carbon network during annealing. Furthermore, to verify the elemental analysis, EDS data from FESEM was compared with XPS data and can be found in figure 3.17. From the fig.3.17(a) for rGO films and fig.3.17(b) for W-rGO films, it can be clearly observed that both analysis indicated similar at% of element present inside films, thus confirming the result.

Doping of tungsten has an influence on energy state of W-rGO films. To find out the effect, and to differentiate with non-doped films, UPS analysis was carried out on both of the films, annealed in different temperatures. Figure 3.18 show the work function from UPS data. It can be observed that, work function for W-rGO films annealed in 1200°C was reduced by 2% compared to rGO films. This is quite a large reduction regarding the field emission mechanism, where work function exponentially affects the emission current. This reduced work function makes the W-rGO film stronger candidate, where a larger current, compared to rGO films, can be drawn, with same applied electric field.

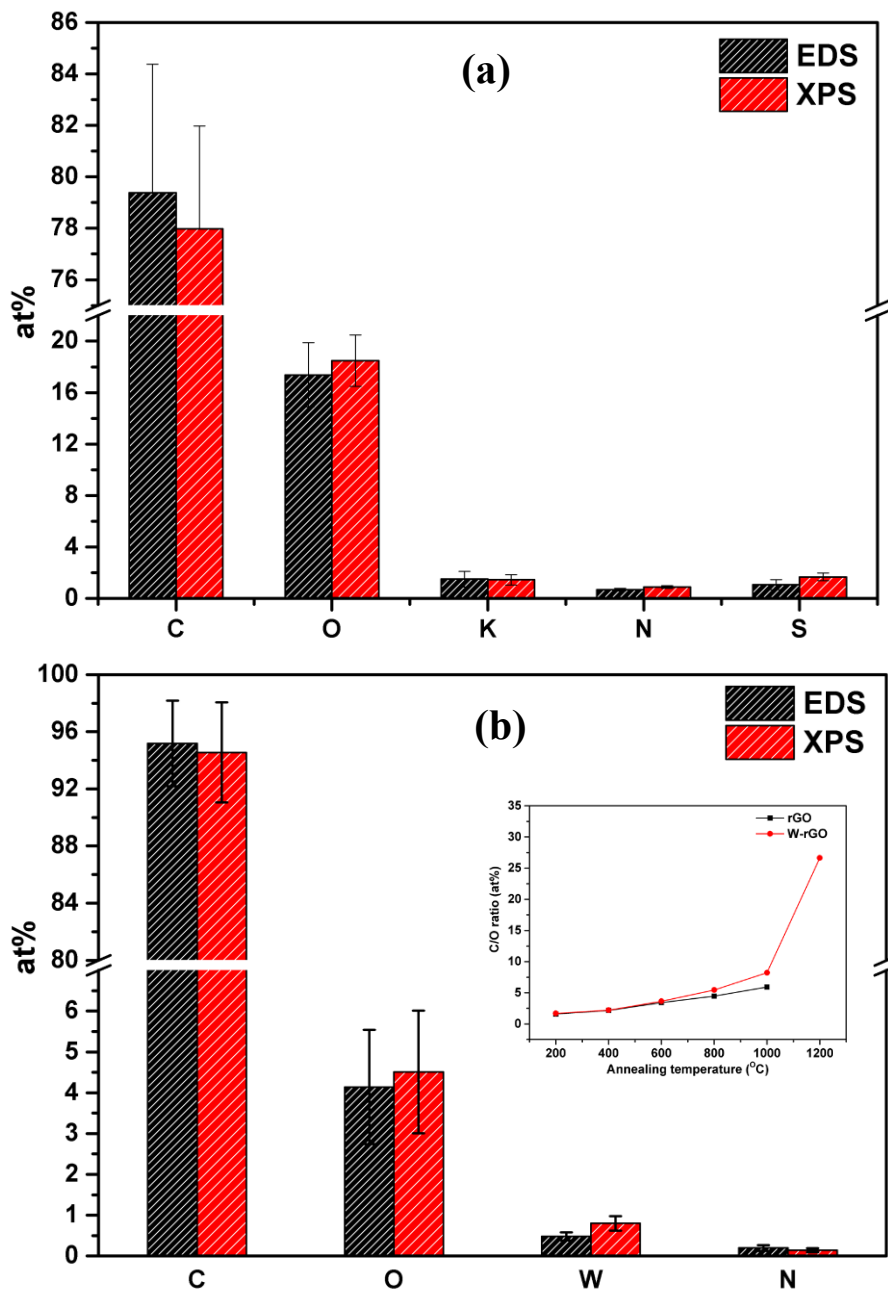


Figure 3.17: Comparison of at% of elemental data acquired from EDS and XPS analysis. (a) rGO annealed at 800°C and (b) W-rGO annealed at 1200°C. (Inset: Carbon to oxygen ratio as a function of annealing temperature)

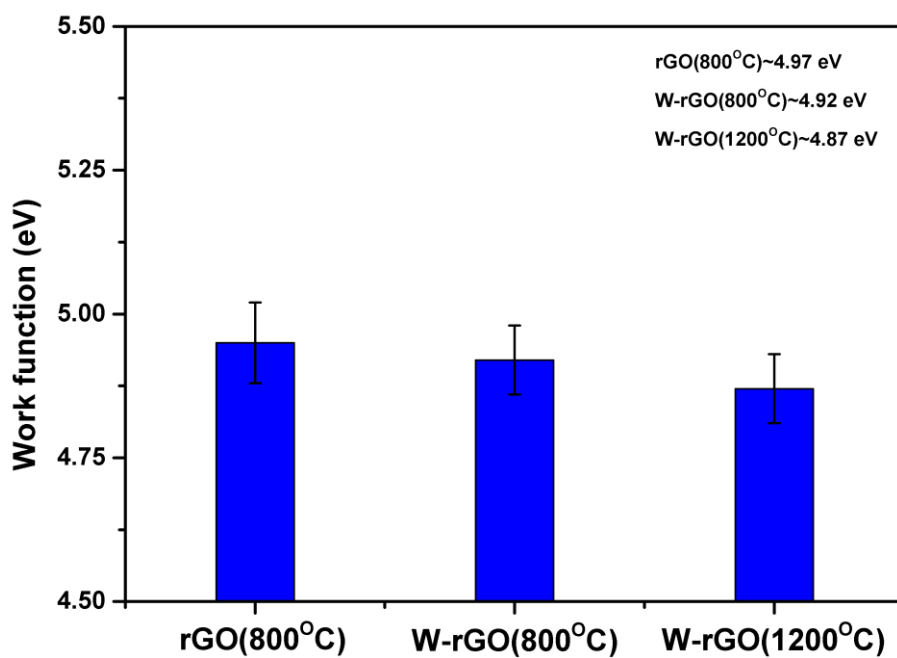


Figure 3.18: Comparison of work functions calculated from UPS analysis. rGO and W-rGO annealed at 800°C show a work function of 4.96eV and 4.92eV respectively. W-rGO films annealed at 1200°C show a much less work function of 4.87eV.

CHAPTER 4

Characterization of Physical Properties and Shaping of W-rGO Films

4.1 Experimental Characterization of Electrical Conductivity

4.2 Experimental Characterization of Thermal Conductivity

4.3 Experimental Characterization of Mechanical Properties

4.4 Shaping of Synthesized Film Using Microtome Cutting Technique

4.1 Experimental Characterization of Electrical Conductivity

Sheet resistance measurement were carried out using the four-point probes [109]. In this device, four probes are placed linearly with equal distance in-between them which can be placed on the sample. Two outer probes are used for passing the current and other two inner probes are used for measuring potential. A schematic diagram of a four-probe device is shown in figure 4.1. Because of the separate current and voltage probes, errors in measurement due to contact is negligible. This is the most broadly used measurement device for electrical resistivity of thin films, bulk metals etc. This method is primarily utilized in the semiconductor and thin film research to measure sheet resistance. The resistivity of sample is given by Eq. (4.1) [110]–[112]

$$\rho = (V/I) \times 2\pi g \dots\dots\dots (4.1)$$

Where V is the voltage(mV), I is the current(mA) and g is the gap in between two point electrodes. Here, g=1 mm. However, for the case of conducting thin-film with large length to thickness aspect ratio, the electrical resistivity (ρ) with the thickness d can be calculated by formula shown the in the equation (4.2), which is given below.

$$\rho = (\pi/\ln 2) (V/I) \times d, \rho \approx 4.532(V/I) \times d \dots\dots\dots (4.2).$$

Here V is voltage drop measured between the internal electrodes, I is the current (mA) and d= thickness of thin film. The electrical conductivity of the film can be expressed as,

$$\sigma = 1/ \rho \dots\dots\dots (4.3).$$

Likewise, using the parameter ρ and thickness of film, the sheet resistance can be calculated using the equation (4) as expressed below.

$$R_s = \rho/d \dots\dots\dots (4.4)$$

For our measurements, we have used the 4-point probe machine (Changmin Tech Co., Ltd, CMT-SR series) with gold pin to avoid measurement errors. Films were placed on top of a dielectric disk and then place in the device for measurement.

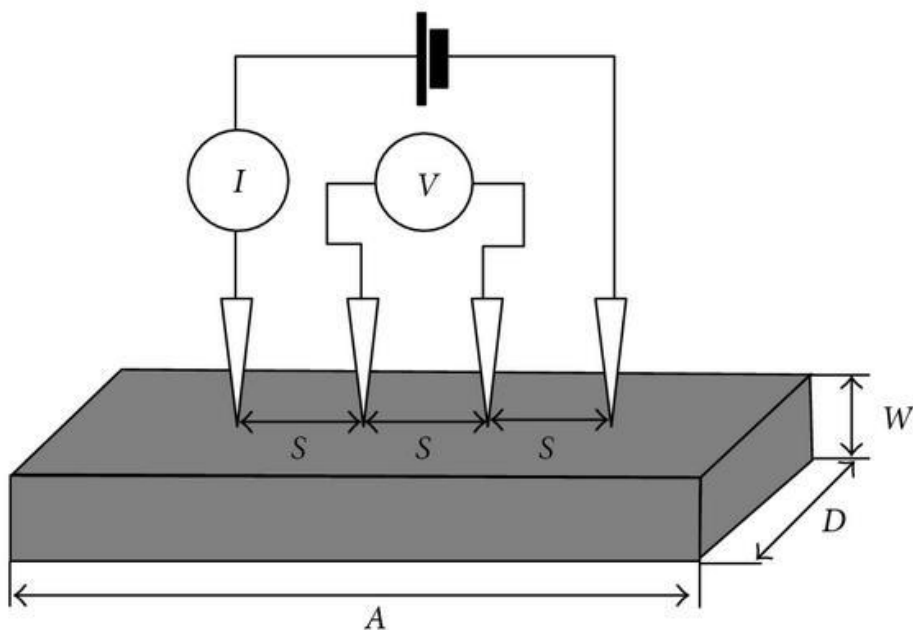


Figure 4.1: Schematic diagram of 4-point probe measurement system.

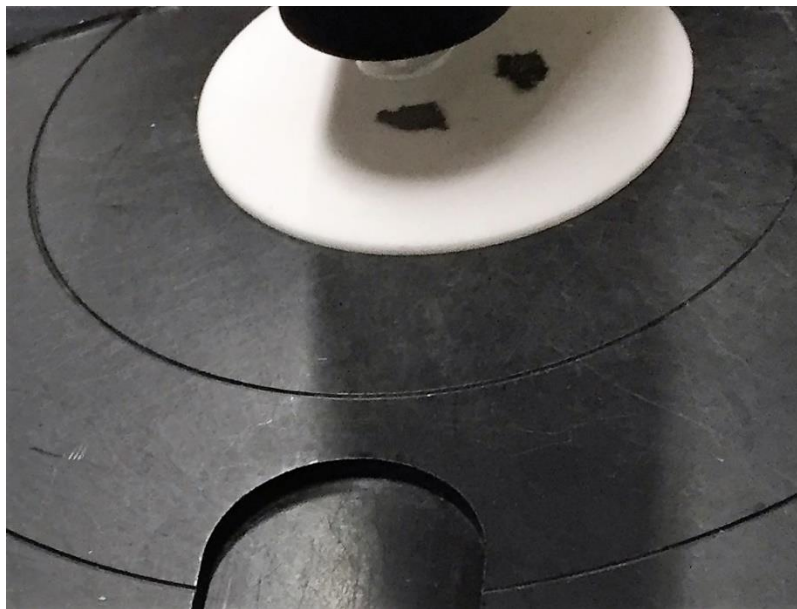


Figure 4.2: Film samples loaded on a 4-point probe measurement stage.

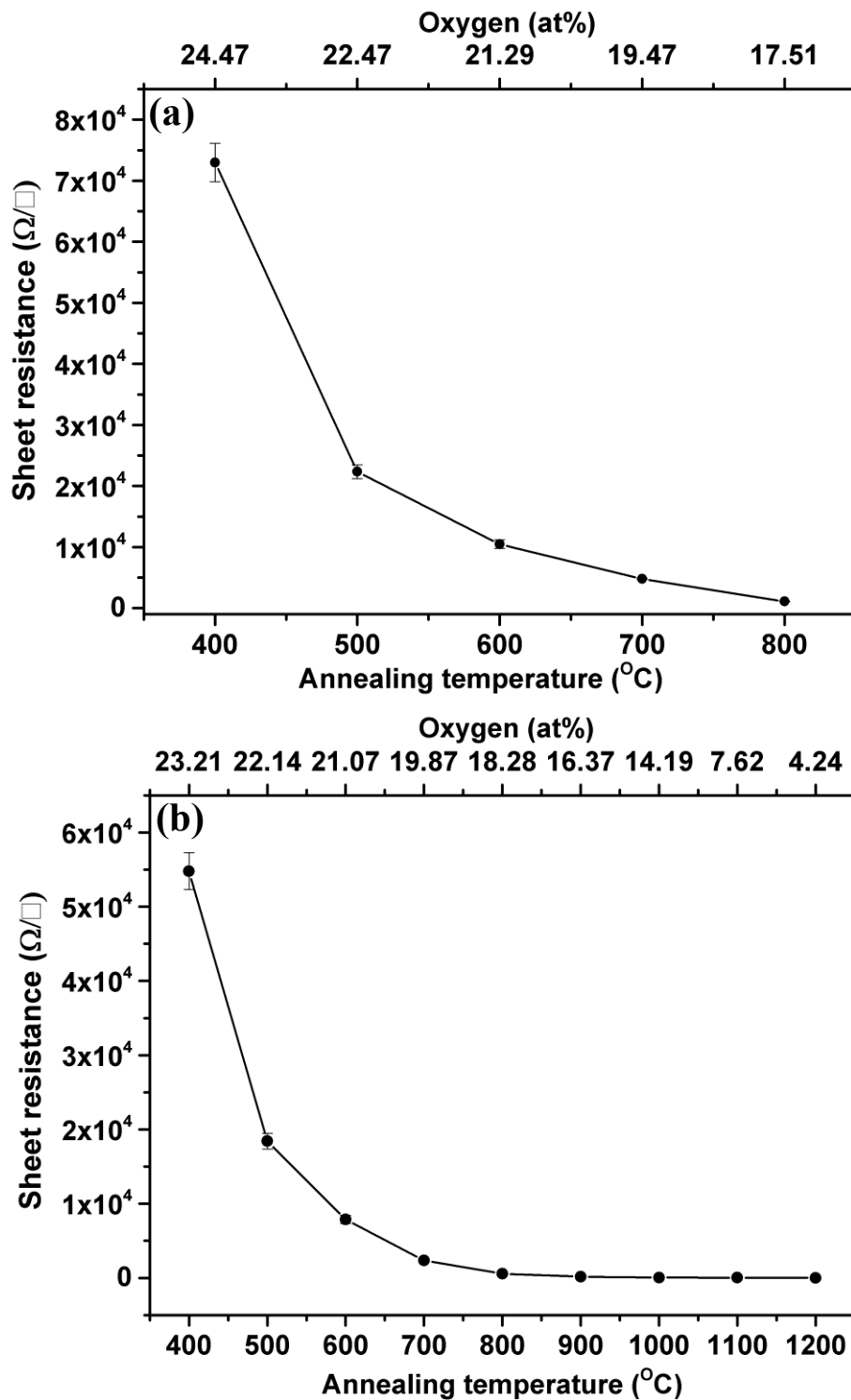


Figure 4.3: Measurement of sheet resistance for (a) rGO and (b) W-rGO as a function of annealing temperature and corresponding oxygen at%.

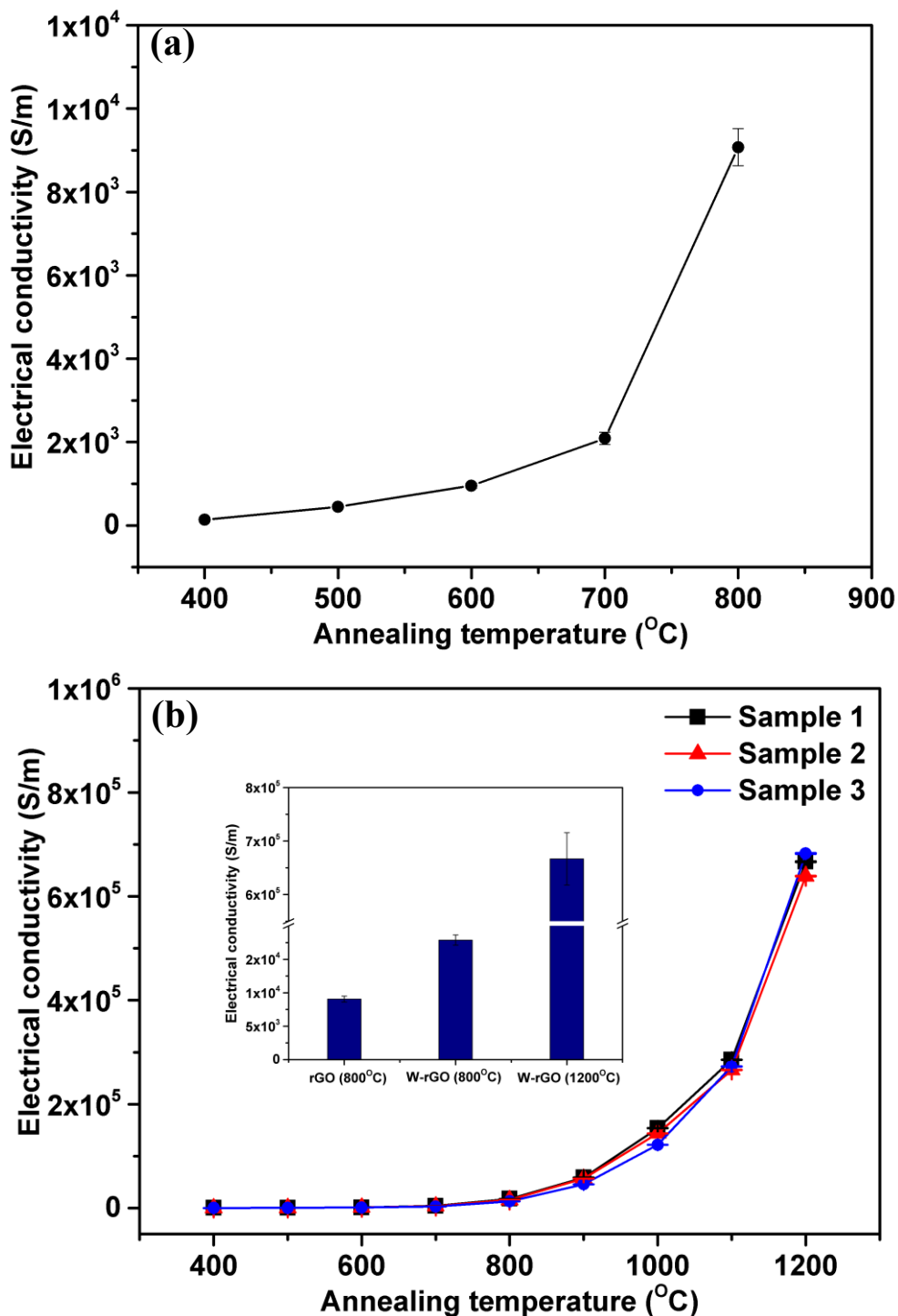


Figure 4.4: Calculated electrical conductivity for (a) rGO and (b) W-rGO as a function of annealing temperature (Inset: Comparison of electrical conductivity).

In this study, we chose two types of film, one is rGO film synthesized by hummers method followed by modified hydrothermal method to form the film. The 2nd type of film was W-rGO films, where films synthesis method was described in chapter 3. Figure 4.3 shows the measured sheet resistance for (a) as-prepared rGO films and (b) W-rGO film with the function of annealing temperature and corresponding oxygen at% (Chapter 3). Conductivities for both of film were calculated using the eq. 4.4. With an increase of the tungsten fraction and decrease of the oxygen functional groups (Chapter 3), the conductivities of the W-rGO film increase dramatically, along with the increasing reduction temperature, and at the annealing temperature of 1200°C it shows about $6.5\text{--}6.8 \times 10^5$ S/m (Figure 4.4 (b)) for a 2.12 wt% of tungsten. This highly improved conductivity of W-rGO film, with an improvement factor of ~66 times, is the record high electrical conductivity for a thin free standing graphene based film [90], [113]–[115]. Comparing with the improvement factor of doped graphene based film, our data is about six times larger than that of AuCl₃ doped graphene based membranes (600%), [116] and three times larger than that of nitric acid doped packed graphene based film [117]. We consider that the dissolved W⁺ ions present during the hydrothermal process are accountable for the in-situ doping (Chapter 3). For the case of un-doped rGO films synthesized by conventional method (Chapter 3), the chemical morphology and physical properties after the thermal annealing behaves typically as described elsewhere [118].

The conductivity of un-doped rGO films constantly increased from 5.1×10^2 S/m for as-prepared films to approx. 1×10^4 S/m (Figure 4.4(a)) for the film annealed in 800°C temperature (20 times improvement). This constantly increasing conductivity implies a typical mechanism for the as-prepared rGO film, which is quite different from W-rGO film [119]. Comparing with the conductivity of W-rGO films, this relatively much lower value of as-prepared rGO films can be attributed to their inability to remove contaminations efficiently and restore the pure graphene structure [60], [67], [70], [100]. This phenomena, that as-prepared rGO films show lower conductivity than W-rGO films, is verified by the experimental result and depicted in figure 4.4(b)(inset).

4.2 Experimental Characterization of Thermal Conductivity

The most broadly used instrument for measuring thermal diffusivity is the laser flash system. A schematic diagram of the laser flash device is shown in figure 4.5. The sample is placed on a stage inside the laser flash furnace [120]. After the sample reaches a preset temperature, a pulse of energy originated from a laser source is irradiated on the one side of the sample, inducing a uniform heating. An IR detector then measure the increment in temperature, as a function of time on the other side of the sample. The thermal diffusivity is calculated in the using these time varying temperature rising data. The thermal diffusivity, T_d is obtained using the equation expressed below.

$$T_d = 0.1388(l^2/ t_{0.5}) \dots\dots\dots (4.5)$$

Here l = thickness of the sample and $t_{0.5}$ = time at 50% increment in temperature. The non-complexity of this technique is clearly visible, where much more precise and direct measurement of time varying temperature rise is incorporated instead of a complex measurement of the total amount of absorbed laser energy & the corresponding temperature rise inside the sample.

The optimization of the thermal conductivity has a critical importance on the stability of the W-rGO film:

- (a) Efficient heat dissipation: Large heat generates during current conduction, which needs to be dissipated efficiently.
- (b) Fast heat conduction: Heat generated during current conduction needs to be transported faster to reduce temperature rise.
- (c) Large specific heat can accumulate larger heat energy thus reducing temperature Rise.

Measurement was carried out on Laser flash device (NETZSCH, LFA 467) with the thermal conductivity measurement range of 0.1W/mK to 4000W/mK and the temperature range of -100°C to 500°C.

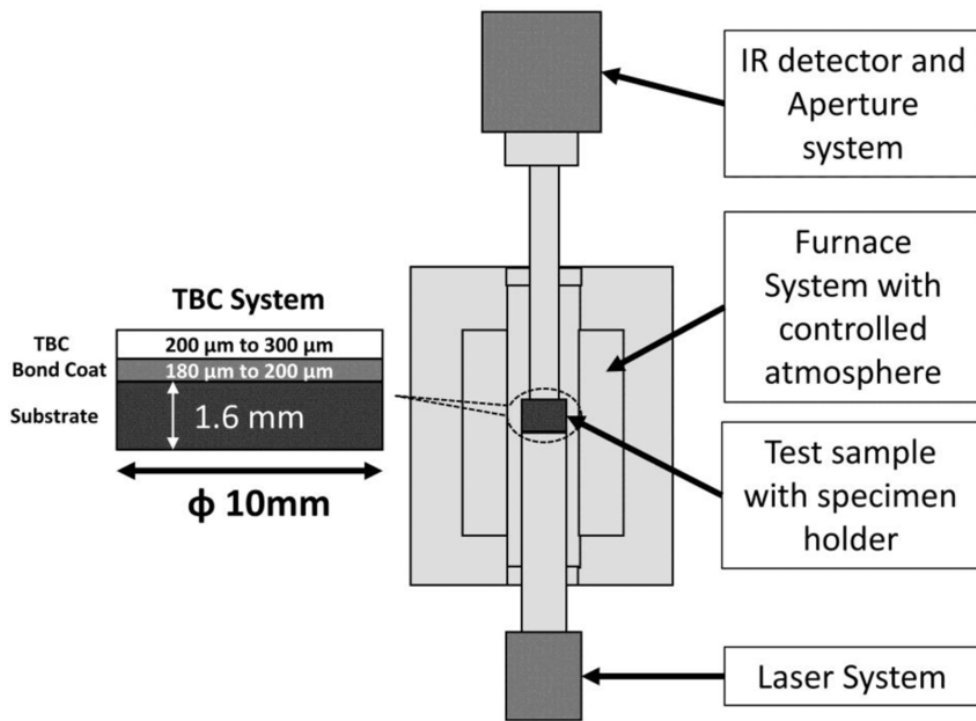


Figure 4.5: Schematic diagram of a laser flash system.

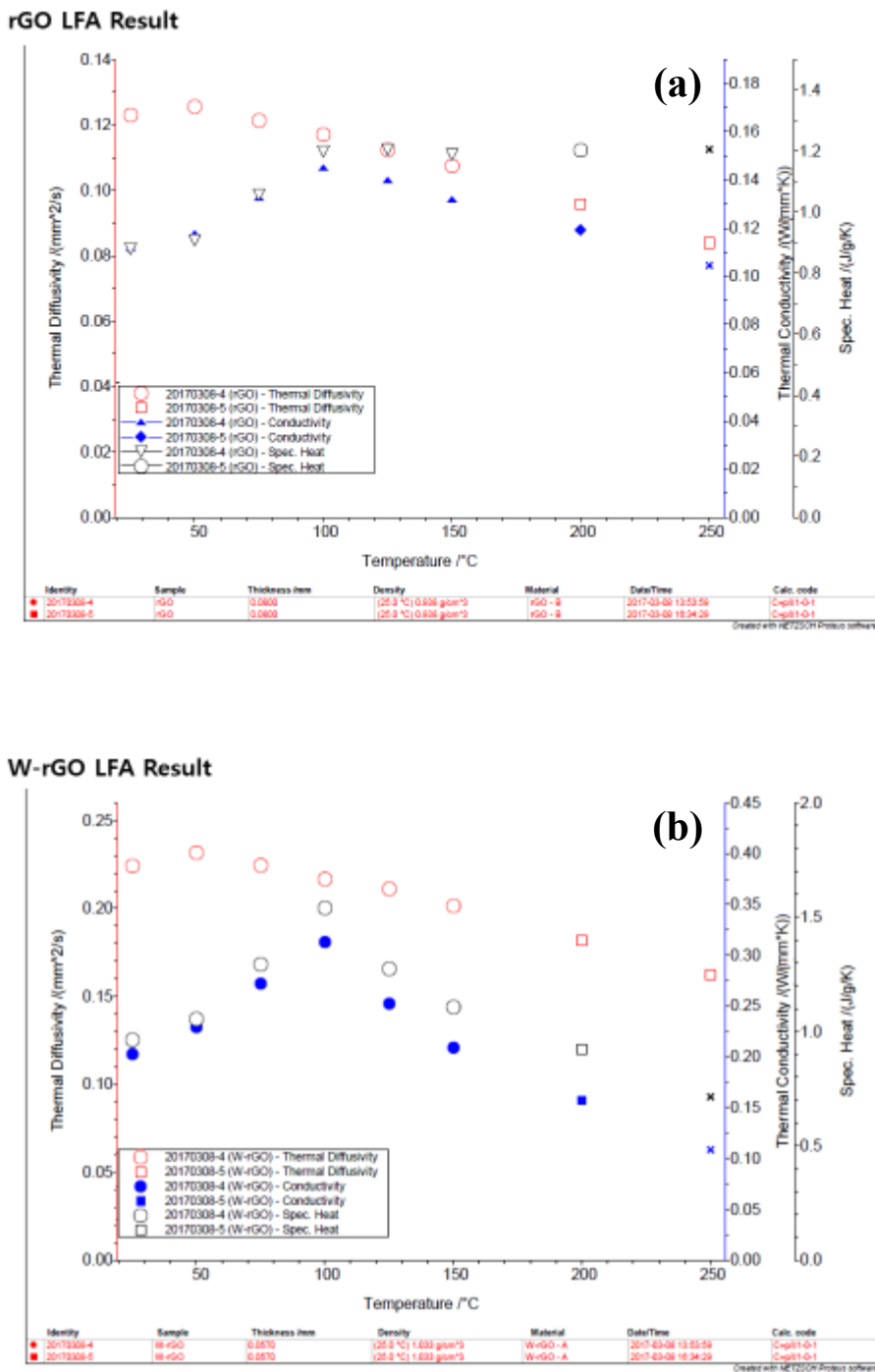


Figure 4.6: Thermal conductivity data acquired from laser flash analysis as function of temperature. (a) rGO shows much lower conductivity than (b) W-rGO.

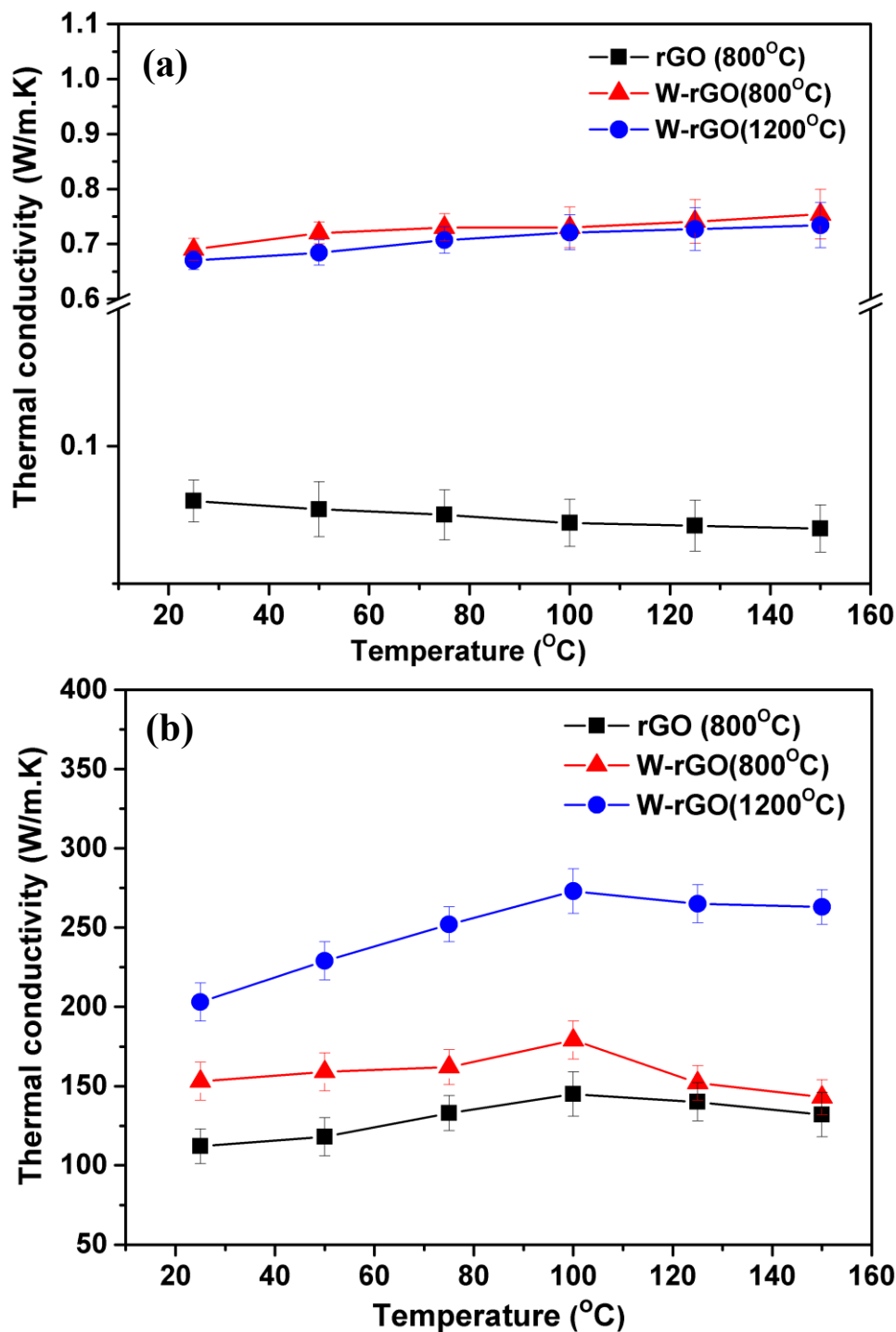


Figure 4.7: (a) Cross plane and (b) in-plane conductivity plot for rGO and W-rGO films as function of temperature. Graph show that the cross plane conductivity is much lower than in-plane.

The film samples studied in this thesis consists of the as-prepared free-standing rGO films annealed at 800°C (upto usable state) and for W-rGO, annealed at 800°C & 1200°C. The holding time for each temperature was of 3 Hr.

The thermal conductivity of the films were measured utilizing the laser flash method described in previous page. The transient laser flash technique can directly measure the thermal diffusivity (α) of the sample [41]. Afterwards, thermal conductivity can be obtained from the formulae $K = m\alpha C_p \dots$ (4.6). Here m is density and C_p is the heat capacity of the sample. The heat capacity can be obtained utilizing the same apparatus using a reference material with known and comparable thermal properties and known heat capacity (example. graphite). The cross-plane and in-plane diffusivity was measured using this method in the regular configuration. For the cross plane, the film is heated by laser from one face and the temperature increment is recorded on the other face. The in plane thermal diffusivity measurement was carried out using the identical manner where laser input on one face of the sample and temperature increased was measured on the opposite face of the sample. Figure 4.6(a) & (b) shows the in plane thermal diffusivity measurement for rGO and W-rGO films respectively, as function of temperature. Figure 4.7(a) shows the plot for the cross plane thermal conductivity, as a function of increasing temperature for rGO and W-rGO films annealed at different temperatures. It is visible from the plot that K is much lower for all the samples. We explain it by the creation of the air pockets (Figure 3.5(e to g)) [121]. However, for W-rGO films, because of restoration of sp^2 bonds, and relatively denser layers, thermal conductivity is comparatively much larger than the as-prepared rGO films. The in plane thermal conductivity is plotted as a function of temperature. The graph is shown for rGO and W-rGO in figure 4.7(b). It is clearly visible that the higher annealing temperature yielded larger K values for both of the films. The room temperature in plane thermal conductivity increases from 120 W/mK for the as-prepared rGO film to 140W/mK at 150°C. However, W-rGO films annealed in the temperature 800°C & 1200°C, shows much improved conductivity of 170W/mK and 260W/mK respectively, compared to as-prepared rGO film. Interestingly, W-rGO films annealed in 1200°C shows a ~200% improvement. This can be attributed to the doping of tungsten, thus reduction of oxygen and restoration of sp^2 bonded carbon network simultaneously.

4.3 Experimental Characterization of Mechanical Properties

Tensile strength or ultimate tensile strength [122] is the ability to withstand a mechanical load for a material up-to the point where the material either breaks or suffers from a permanent deformation. Tensile strength can be measured by Universal Testing Machine (UTM) [123]. A schematic diagram of a four-probe device is shown in figure 4.8. Elastic modulus and Poisson's ratio can also be found f this testing method. Data from this measurement is plotted as applied load vs stretching, which can be converted to stress vs strain (uniform change in length over the sample under test).

The key uses of this testing devise is to plot a stress versus strain graph. Tensile strength measurement finds out the strength of the sample by the help of a simple stretching procedure. In general, a sample under test with known dimension is dragged with an slow and uniform rate in the UTM machine while data is recorded in the form of strain (ϵ) which is defined as below,

$$\epsilon = (\text{change in length}) / (\text{original length}) = \delta/L_0 \dots\dots\dots (4.6)$$

The stress (σ) can be expressed as,

$$\sigma = (\text{applied force}) / (\text{original area}) = P/A_0 \dots\dots\dots (4.7)$$

The target of this measure is to obtain the mechanical properties of sample material, such as ultimate tensile strength, young's modulus, passion's ratio etc. For the case of graphene based film like materials, such as GO, rGO etc., which are assembled in stack by stack, are studied to find out their mechanical properties [124]–[126], however not so extensively. As a layer of carbon atoms with single atomic thickness, graphene can be engineered to several forms, such as roll of graphene, graphene nets and many more. Tensile strength of graphene sheet was found 200 time stronger than stainless steel, thus making it strongest material so far [127]. Thus a microstructure made from graphene is anticipated to reflect its

unprecedented mechanical properties to the bulk structure also. However, it is difficult to utilize these sheet for their lack of availability. A more economic and flexible product, such as reduced graphene is more preferable.

However, rGO generally contain a large number of impurities in form of the oxygen-rich chemical groups like epoxy and hydroxyl. In this regard, rGO deteriorates much from its original mechanical properties. Several groups are trying to restore the mechanical properties of rGO film using different methods such as annealing [128], [129], metal doping [130] etc. Comparing both of the process we have adopted a combination of both of the process to improve as much as possible.

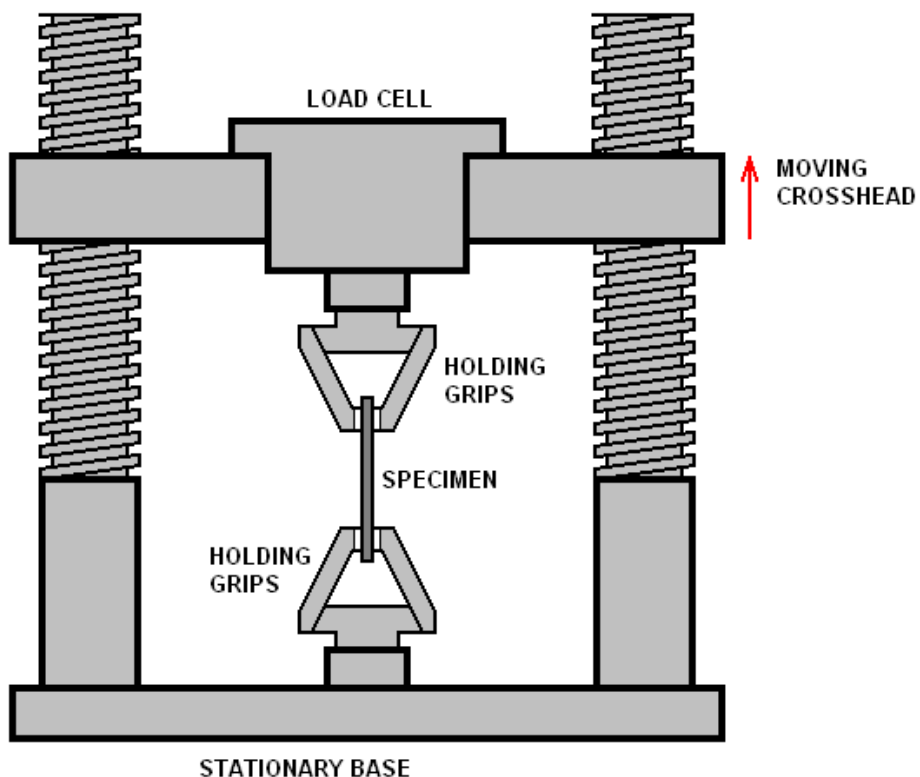


Figure 4.8: Schematic diagram of a universal testing machine.

Like thermal conductivity measurement, samples examined in this thesis includes the as-prepared free standing rGO films annealed at 800°C, and W-rGO films annealed at 800°C & 1200°C. The holding time for each temperature was of 3 Hr. All the film samples for the mechanical measurements were slit into rectangular shape with a width of 5 mm and length of 10mm by a x-acto knife. To exclude the influences of humidity on mechanical properties of rGO and W-rGO films, all samples were kept in a constant humidity environment (70%) for one day before tensile tests, and all tensile tests were performed under identical environment with a temperature of 25°C. Mechanical measurements were performed on an Instron-5543 UTM device (Illinois Tool Works Inc, USA). A uniform loading rate of 0.2 mm/min & a 5mm gauge length were used for the measurements. Tensile strength and corresponding strain were recorded. Using the slope of the linear region of stress versus strain curve, Young's modulus was calculated and fracture toughness is obtained by integrating the areas under the same curve. All the presented data were the average of over 5 strips of the same sample. Suitable gripping force should be modulated for different samples, and the sample sliding at the grip or samples fracture closely neighboring the clamps should be abandoned.

From the figure 4.9, it can be observed that remarkable improved in mechanical properties are achieved. The tensile strength 4.9(a) graph show that the rGO, annealed in 800°C, have a tensile strength of ~ 450 MPa where W-rGO have ~ 680 MPa. Interestingly, W-rGO films annealed in 1200°C has a tensile strength of ~ 941 MPa, which has been improved by 200% where the young's modulus (fig4.9(b)) is by ~ 20 times, compared to as-prepared rGO films. This remarkable tensile strength in among the highest for a thin free standing rGO films [131] to the best of our knowledge. These remarkable restorations of the mechanical properties can be attributed to our novel synthesis process where we successfully doped W into the rGO films using modified the synthesis method by introducing a novel sol-sol mixing process.

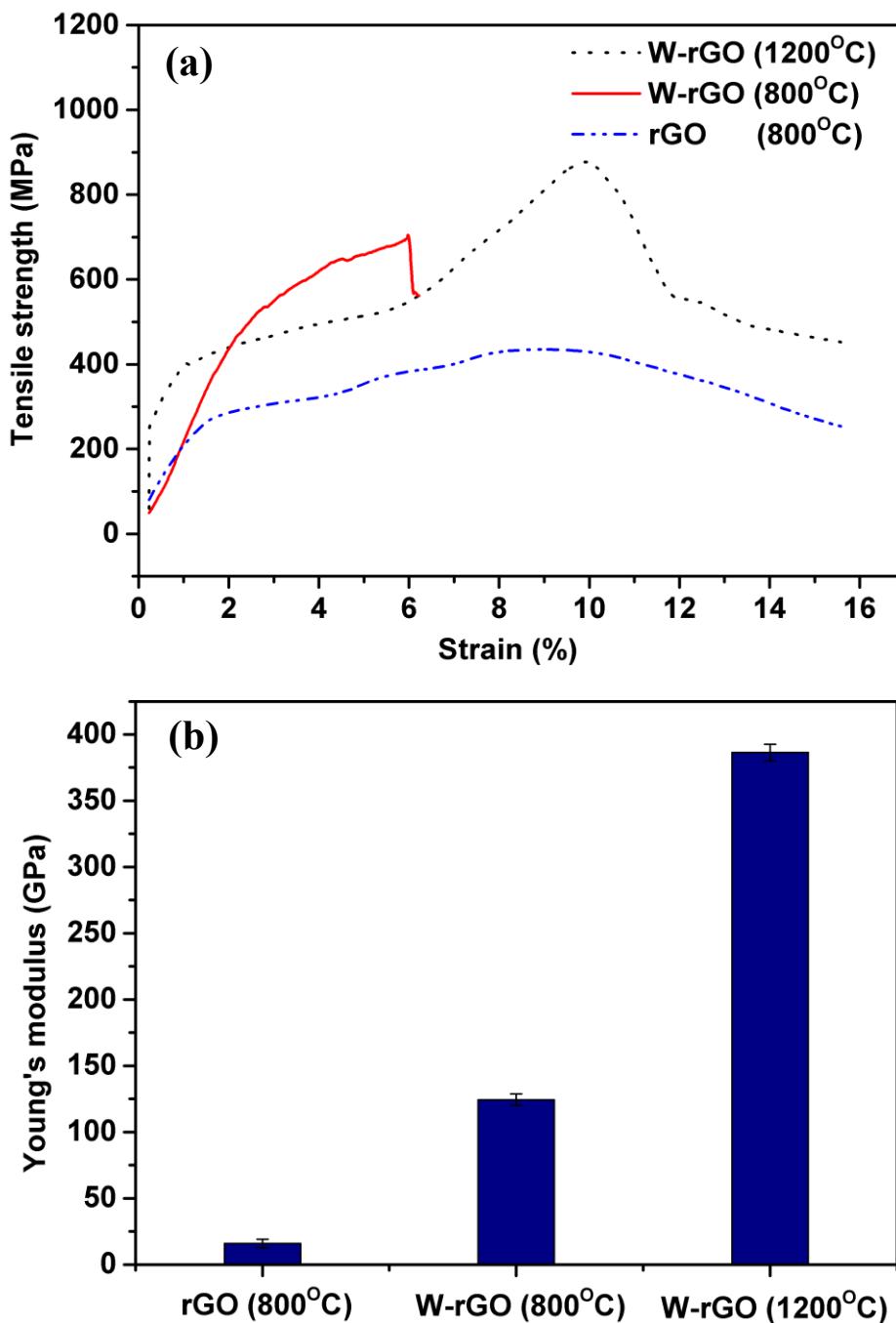


Figure 4.9: (a) tensile test graph for rGO(800°C) and W-rGO (800°C & 1200°C). (b) comparison Young's modulus. It can be seen that the W-rGO has a Young's modulus more than 20 times that of rGO.

4.4 Shaping of Synthesized Film Using Microtome Cutting Technique

The prepared rGO film was slit into shape on the thin edge by several methods such as the reactive ion etching (RIE) [132], laser cutting [133], knife cutting, microtome [134], and focused ion beam (FIB) [135] to obtain a protrusion free edge cross section which is necessary for uniform field emission. Among these methods, FIB method produced the highest uniform surface. However, FIB is not efficient as it requires a large amount of time, mainly because graphene based materials have strong resistance to ion collision where colliding ion is base of the FIB cutting. Both of the films rGO and W-rGO film is free standing in nature. Therefore, it is inconvenient to mask these film against etching by ion. As a consequence, it is extremely difficult to use RIE method, as it cannot provide uniform etching on the edge surface. The laser-cutting method is ruled out, as it produces localized heating, ultimately damaging the edge surface. However, both rGO and W-rGO films have shown mechanical properties such as young's modulus, ultimate strength etc., which makes them stable (even for a 100 nm thin film), even when handled manually. These excellent properties make these film stable under manual cutting, even with knife also. These phenomena give the idea to use microtome technique. To obtain precision shaping using the microtome, rGO films were coarsely slit in rectangular shape using the x-acto knife and embedded in paraffin wax cubes, for holding firmly during the microtome operation (Figure 4.9(a)). After shaping using the microtome, those films loaded inside the paraffin wax is (Figure 4.9 (b)) was cleaned using diluted xylene solution followed by ethyl alcohol solution. Those cleaned films were annealed at 180°C inside a vacuum oven to remove rest of the contaminations. After that these films were mounted inside stainless steel jig and prepared for field emission experiment.

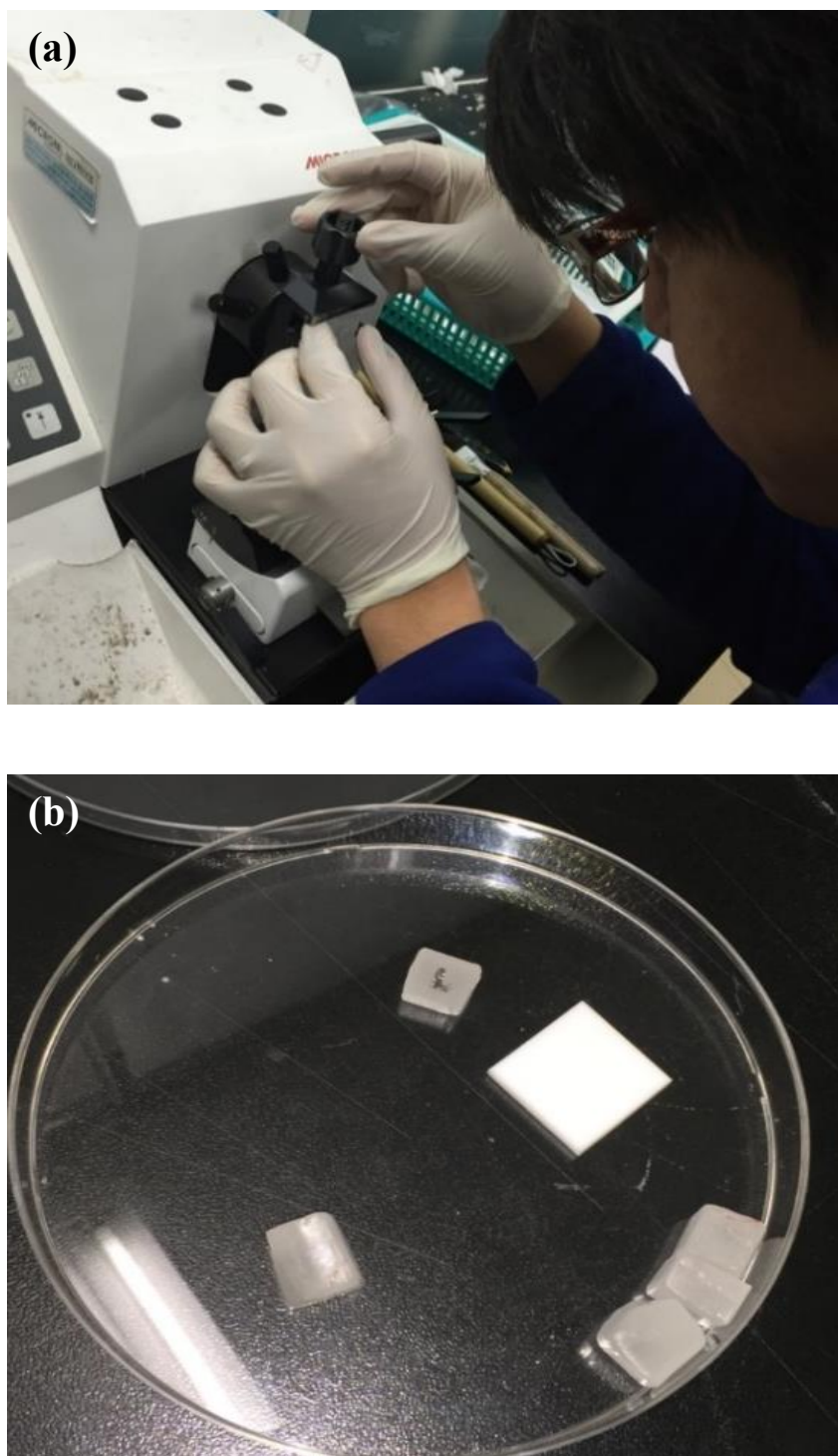


Figure 4.10: (a) Shaping using microtome (b) Shaped films inside paraffin wax.

CHAPTER 5

Realization of W-rGO Film Field Emitter Cathode

5.1 Fabrication of Cathode

5.2 Details of Experimental Setup for Emission Measurement

5.3 Characterization of W-rGO Film Filed Emitter Cathode

5.3.1 Emission Measurement

5.3.2 Characterization of Emission Edge after the Experiment Using FESEM

5.1 Fabrication of Cathode

An as prepared rGO and W-rGO free standing field emitter cathode was synthesized using conventional and a novel sol-sol as discussed in section 3.1. The average thickness was found to be about 100 nm. After the synthesis, both of the films are heat treated inside a furnace under a nitrogen environment. It is found that rGO films can hold the structural integrity upto an annealing temperature of 800°C, where a W-rGO film can go upto a much larger temperature of 1200°C. Reason behind this phenomenon was explained in section 3. For field emission comparison, rGO films annealed in 800°C and W-rGO film annealed in 1200°C was chosen. (Both of the cases, the usable film was chosen).

- 1) **Shaping of films:** Films were shaped using microtome (Section 4). Shaped and cleaned films are flexible, can be handled manually (Figure 5.1(a)) and can be fitted in any test set-up
- 2) **Fabrication of testing jig:** A sandwich type holder jig was specially designed and fabricated (Figure 5.1(b)) using stainless steel (SS304L) for the field emission experiment
- 3) **Mounting of the films:** Films are mounted in-between the stainless steel jig (Figure 5.1(b)), like a sandwich structure. Special mounting jig was designed using two silicon wafer. Each wafer has a thickness of 0.5 mm. One wafer was broken into half and placed on top of another wafer, such a manner that the holder jig can be place on top of the broken wafer. The film height was adjusted to 0.5 mm from the top of the holder jig using the broken and intact wafer.

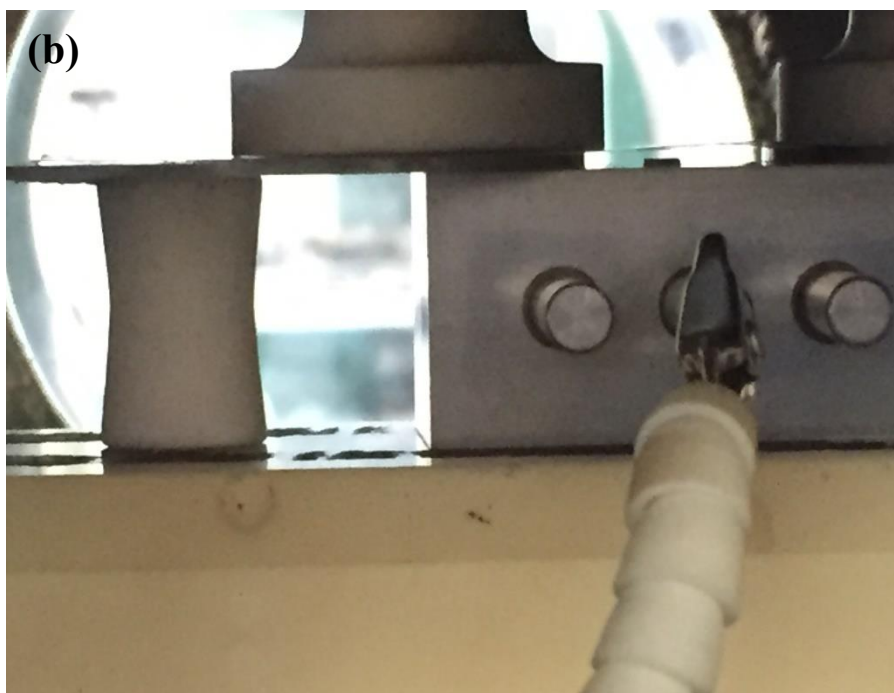
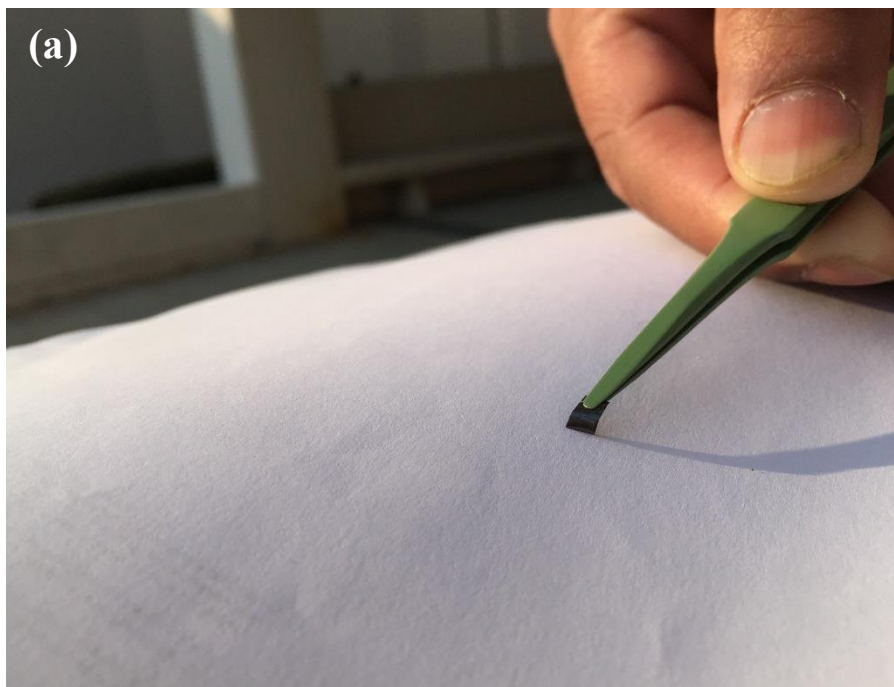


Figure 5.1: (a) Shaped W-rGO film (b) Film loaded inside experiment jig.

4) **Assembly of cathode test set-up:** Figure 5.2(a) shows the schematic test set-up. Films loaded in-between the holder jig was placed on top of a ceramic bar. A 0.1 mm thick moly sheet was used as anode1 where a molybdenum bar was used as anode2. 20 mm thick glass slide spacer was used to adjust the height of holder and glass spacers. Glass slides were used between holder and anode1 to maintain a distance of 0.5 mm between anode1 and film end. Two pieces of hollow ceramic rod were used in between anode1 and anode 2. The complete assembly of test setup was mounted inside an UHV chamber containing: (a) 2 anodes for field emission measurement, and (b) later anode2 was removed and anode1 was replaced with an ITO glass to obtain beam shape.

5.2 Details of Experimental Setup for Emission Measurement

The emission measurement and beam shape characterization were performed in an analytical UHV system. A schematic diagram of the stainless steel vacuum chamber for the field emission experiment, containing various facilities is shown in figure 5.2(b). The photograph of the test set-up is consisting of: a) Rotary, turbo and ion pump which helped us to maintain a vacuum level of $1e-8$ torr inside the chamber, during the experiment, b) a DC power supply (upto 5 kV, model: Glassman high voltage), c) two digital multimeters (NI-model:3301 & LG 3301) for field emission current measurement, d) $50\text{ k}\Omega$ resistance to protect the setup from current overflow, e) ITO glasses for beam shape luminance and f) CCD camera (THOR Labs), for beam shape capture and measurement from ITO glass.

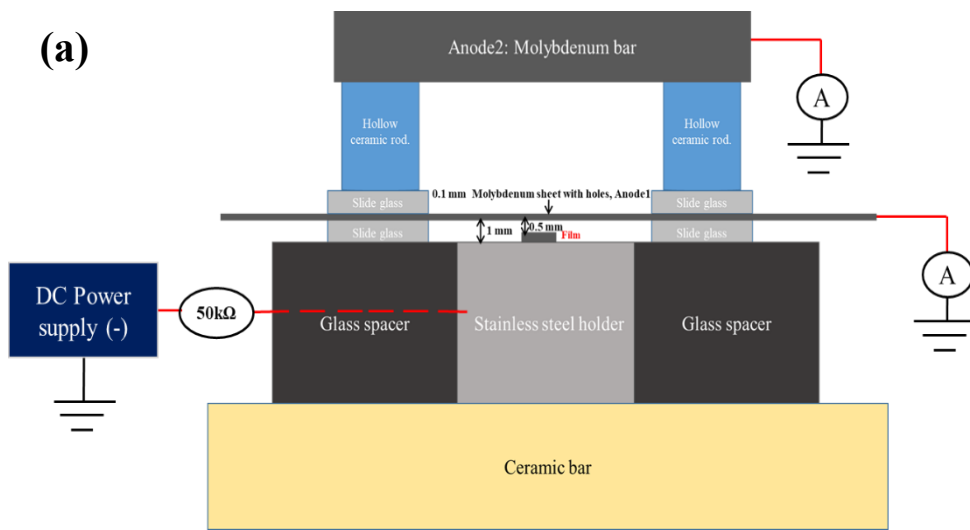


Figure 5.2: (a) Schematic diagram of test set-up. (b) Photograph of analytical system.

5.3 Characterization of W-rGO Film Field Emitter Cathode

5.3.1 Emission Measurement

To find out the field emission capability of the synthesized films, measurements were carried out in dc condition. Three different films, that is rGO & W-rGO film annealed in 800°C and W-rGO film annealed in 1200°C, was used for comparison of field emission performance & stability. For all the three cases, film emitter was kept parallel to the anode with a gap of 0.5 mm in between them to form a plane parallel diode.

The out gassing of cathode was carried out by gradually holding and rising the applied voltage. Holding time for each step was 10 ~15 minutes. DC voltage is applied across the diode to draw emission current from the cathode. All experiments were performed in room temperature condition. The I-V characteristics data were obtained at different applied voltage. These plots and calculated current density plots are depicted in figure 5.3(a) & (b) respectively. Both of these films follow F-N rule for field emission which can be confirmed by the F-N plot exhibited in figure 5.4(a). From the I-V characteristics, it can be seen that, W-rGO emit a current of ~18 mA for an applied voltage of 3.7V. For the same applied voltage, rGO produced a current of 14mA which is 77% of the field emission current from W-rGO. However, at this point rGO started to degrade and visible burnout was noticed. During the 2nd cycle, rGO shows much less field emission current of ~ 6mA which is ~33% of field emission current from W-rGO. Field emission current density was calculated by dividing the emission current with the emitter edge cross section area obtained from FESEM (section 3) and plotted in figure 5.3(b). Calculated average current density was more than 6000A/cm² from the W-rGO film, which is so far the best from any W-rGO film, to the best of our knowledge. With further experiment, maximum current density achieved from a W-rGO was more than 10000 A/cm², but because of extreme rate of degassing due to large power dissipation on anode, vacuum breakdown occurred and applied potential was reduced to avoid damage to the film. Similarly, calculated current density from rGO film was ~ 4400A/cm² and ~

2300A/cm², before and after degradation respectively. From this data it can be inferred that the field emission performance is quite larger in case of W-rGO film compared to the rGO film. Furthermore, excellent stability can be observed (Fig.5.4(b)) over a 192 hours of test, at an applied field of 6.6V/um with less than 1% fluctuation. It can be concluded that the W-rGO film is a far superior candidate over rGO film, for a field emitter, in terms of current density and stability. This excellent improvement and stability can be attributed to the doping of the tungsten during the synthesis process, which improves the field physical properties of W-rGO film to a larger extent. Further, to study the stability over a long term use, a 1000 Hr. stability test was carried out on the W-rGO film and the current vs time plot is shown in figure 5.5. During the experiment, the applied voltage was kept at 3.1V to a corresponding field emission current of 3.8mA. Emission current was kept at a comparatively low value to avoid any unattended accident during this long term experiment. It has been found that during this long run, current was not degraded and the current fluctuation was less than 1%. This result again proves that the W-rGO film can be strong candidate for a large current, stable field emitter.

The field enhancement factor is obtained using Fowler-Nordheim equation as follows,

$$J = A(\beta E / \phi)^2 \exp(-B\phi^{1.5} / \beta E) \dots\dots (5.1).$$

Here J is the current density, A and B are F-N constants and can be expressed as $1.54 \times 10^{-6} \text{ AV}^{-2}\text{eV}$ and $6.83 \times 10^7 \text{ eV}^{-3/2}\text{Vcm}^{-1}$ respectively. E is applied electric field, ϕ is the work function and β is the field enhancement factor.

The work function is determined using UPS (chapter 3). Then the field enhancement factor can be expressed as,

$$\beta = -Bd\phi^3 / S_L \dots\dots\dots (5.2).$$

Here S_L is slope of F-N plot, where F-N plot is shown in figure 5.4(a) and d is anode cathode distance. Calculated field enhancement factor for W-rGO is ~1427

which is quite large for a free standing graphene based film. Interestingly, calculated β for rGO before degradation show a value of 1567 which is larger than W-rGO films. This phenomenon took place because of the geometry of rGO films. From the figure 3.5 (chapter 3) it can be clearly seen that, although rGO films sustained its structure after 800°C annealing (but below 1000°C annealing), edges were noticeably exfoliated compared to W-rGO film. Local field enhancement took place on those edges, which resulted in an overall large enhancement. However, this local enhancement is also partially responsible for eventual failure (degradation). Nevertheless, though field enhancement in case of W-rGO film is less than rGO film, field emission current is larger for W-rGO film because of the lower work function (chapter 3). Moreover, W-rGO films has showed a superior stability even for a very large current density, compared to rGO films. To observe the beam shape, anode was replaced by a phosphor coated Indium Tin Oxide (ITO) glass. To visualize the post experiment state, films used in field emission test were removed carefully from the jig and analyzed using FESEM. Beam shape and post experiment analysis is discussed in next section.

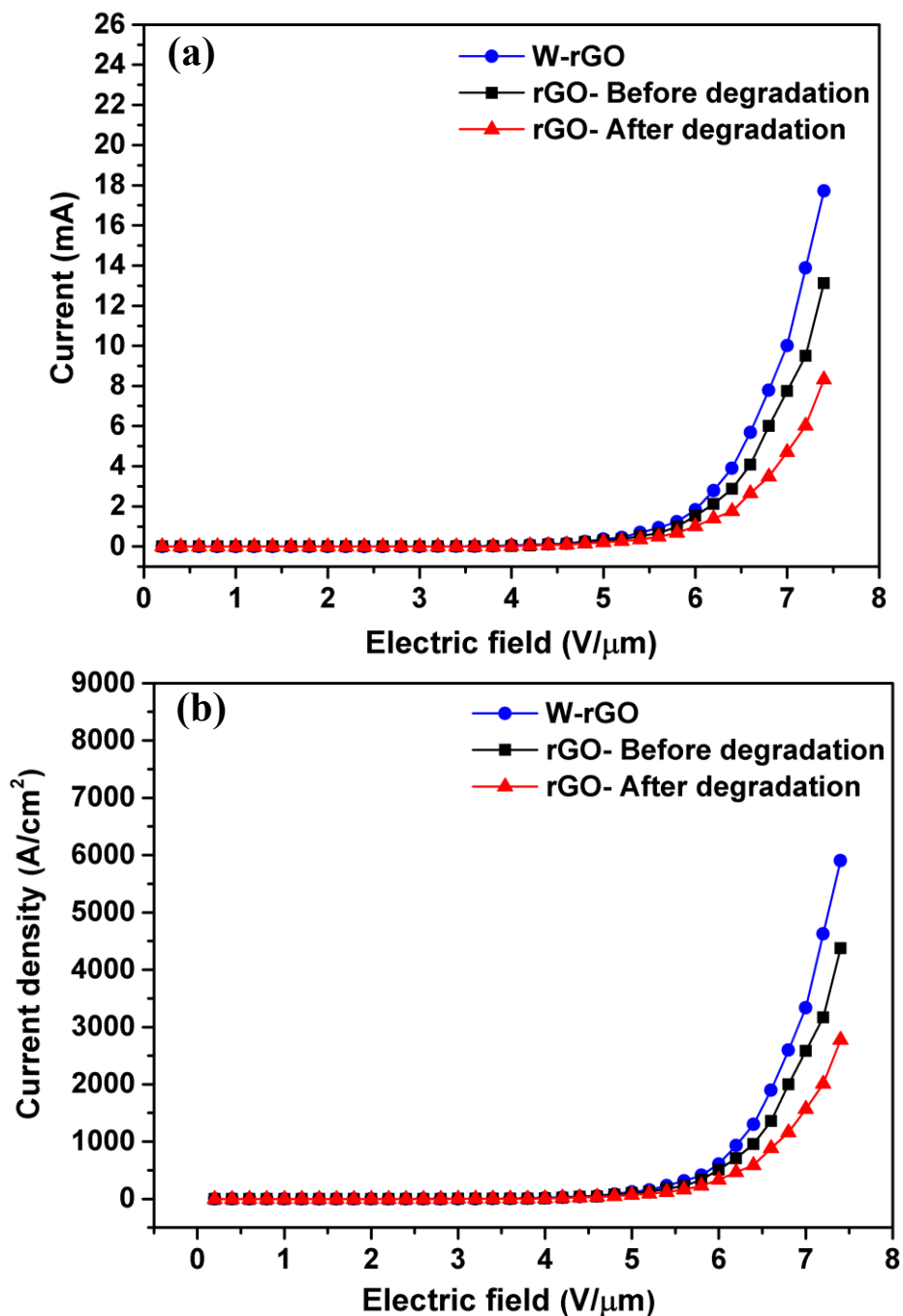


Figure 5.3: Field emission experiment data. (a) Field emission current as a function of applied potential for the rGO (800°C) and W-rGO(1200°C) films. (b) calculated emission current density for rGO (800°C) and W-rGO (1200°C) films.

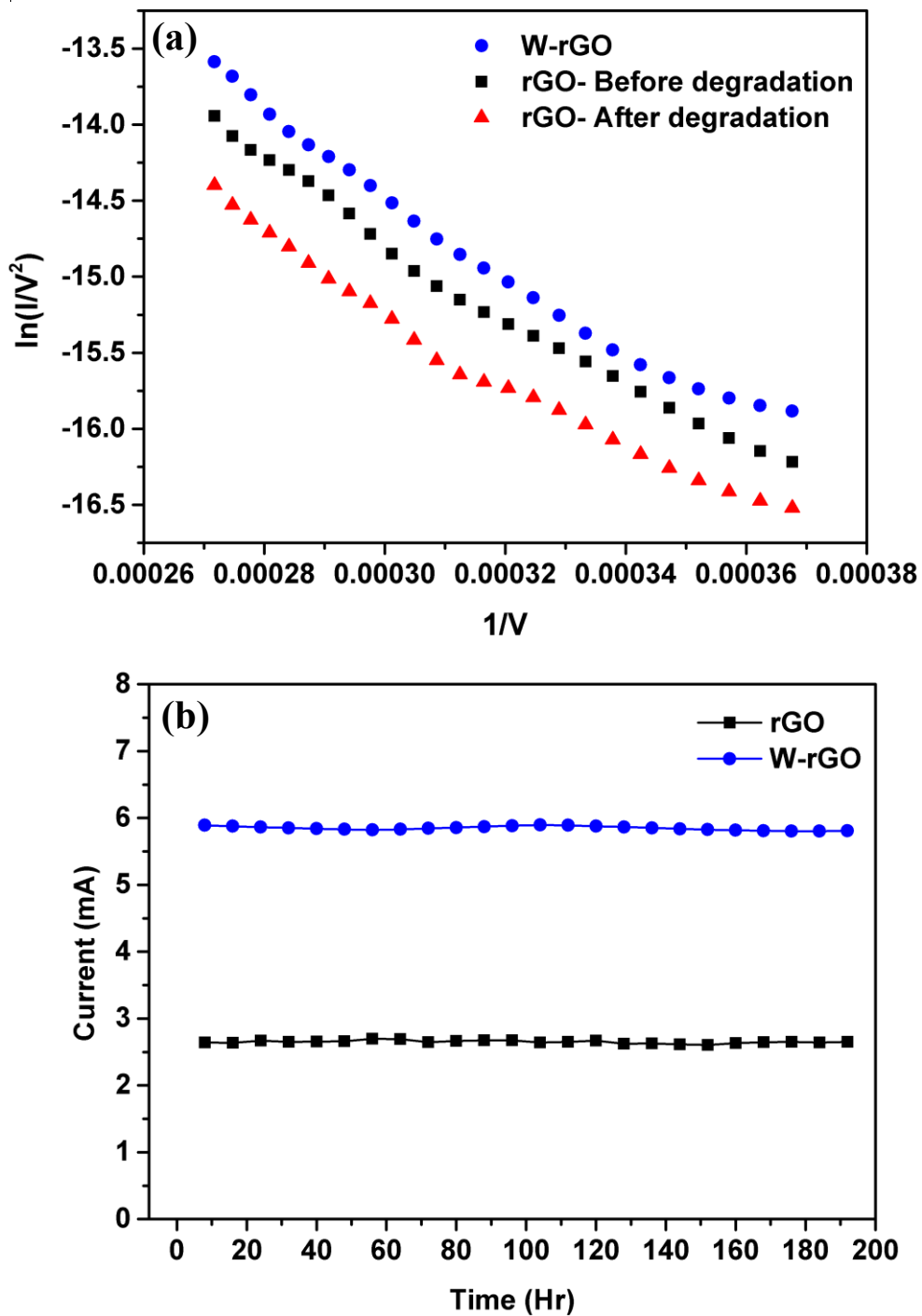


Figure 5.4: (a) F-N plot. (b) Stability measurement over a period of 192 Hr. Applied potential was 3.3 kV.

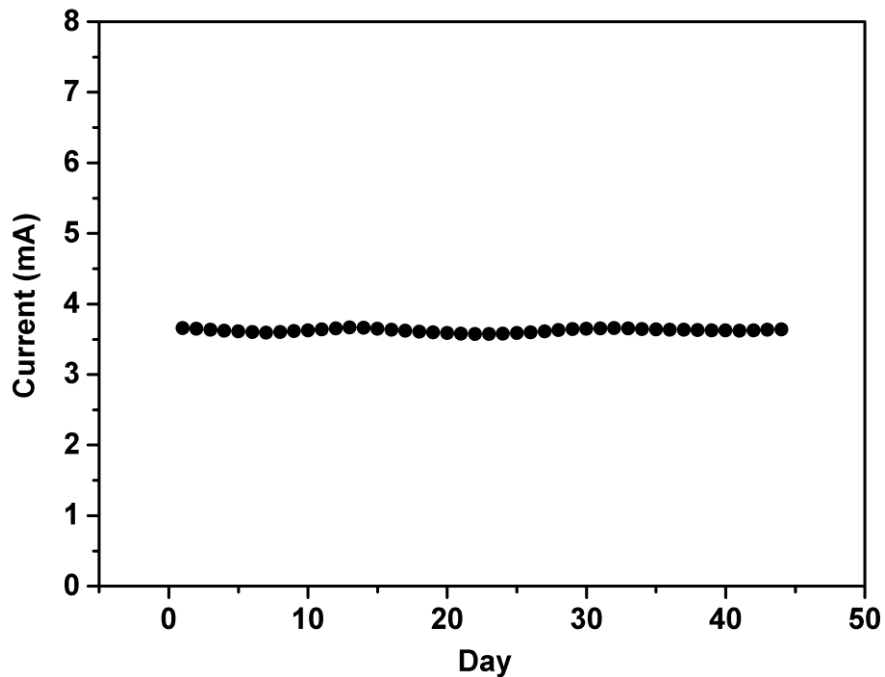


Figure 5.5: 1000 Hr stability test reveal that the W-rGO films is remarkably stable over a long period of time and can be used in practical devices.

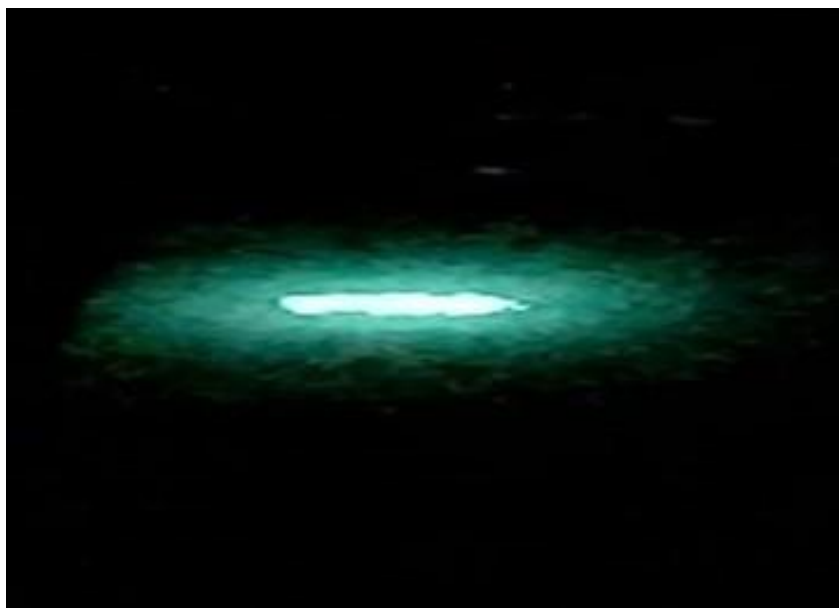


Figure 5.6: Beam shape captured on a phosphor screen on ITO glass.

5.3.2 FESEM Characterization of Post-Experiment Emission Edge

Emission pattern can be seen in figure 5.6, where a phosphor screen was placed instead of the anode. Rectangular sheet type beam pattern can be observed which denotes that emitted electron beam is sheet type in nature and can be shaped more precisely with focusing elements. Figure 5.7 (a) & (b) show the rGO and W-rGO films respectively after the field emission experiment. It is evident for W-rGO film that this film structure holds to a tight formation (though exfoliated nominally) where the rGO films edge is destroyed completely. From this result we can depict that the W-rGO films does not degrade even after a long cycle of field emission operation. Because of the compact, large aspect ratio yet strong structure, lower work function, extremely improved physical properties and unmatched stability, W-rGO films can be a strong potential candidate as a field emission cathode for realizable, high power, compact THz devices.

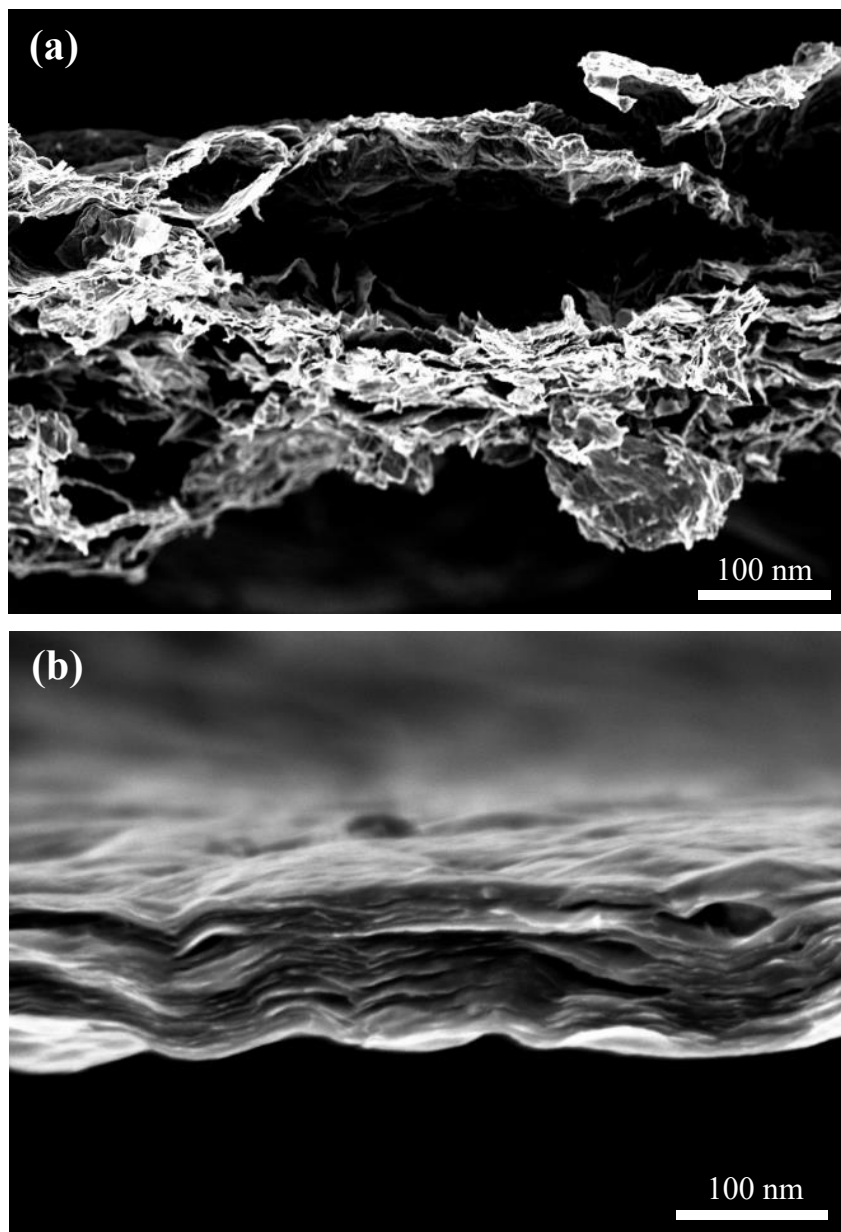


Figure 5.7: After experiment SEM image. Physical damage is clearly visible for the case of (a) rGO, where (b)W-rGO film retained the structure.

CHAPTER 6

Discussion of Results, Conclusions, and Suggestions for Future Work

6.1 Study of Graphene Field Emission

6.2 Study of Various Synthesis Methods for rGO Film

6.3 Synthesis and Characterization of W-rGO Film

6.4 Realization of W-rGO Film Field Emitter Cathode

6.5 Suggestions for Future Work

The primary influencing factor on field emission is of the geometric structure and work function. Large aspect ratio structure has larger field enhancement on the emission surface, whereas lower work function increases the current density for a similar applied field. Therefore, thin films with large aspect ratio was synthesized to extract large field emission current. It was found that the films with ~100 nm thickness has very high current density field emission. Studies also reveal that the uniform edge has positive influence on emission current density.

However, experimental studies also reveal that the films are not stable after a certain current density. Physical burnout took place after a current density of 10000 A/cm². Primary reason behind this failure was the degraded physical properties. Further analysis has revealed that rGO films, synthesized using conventional methods have large amount of contaminations in the form of oxygen functional groups. These groups are responsible for the degradation of electrical and thermal conductivity. High temperature annealing results in the reduction of oxygen functional groups, consequently improving the conductivities. However, during high temperature reduction, along with the oxygen groups, a large amount of carbon atoms also evaporates, and ultimately after a certain temperature, those thin film suffers from physical damage, making those unusable. Another method is to dope with metal particle so that the broken carbon network can be repaired. This method is effective upto a certain level. But where there is large improvement is required, say in the order of 2, this method proven to be inefficient. Here we have combined those above mentioned two methods to achieve large number of improvements. Films synthesized using this novel method were assembled in an UHV system for emission and for beam shape characterization. The maximum current density up to 10000A/cm² with an average of 6000A/cm² were drawn. The I-V characteristics exhibited large field enhancement. Large current density with long stability makes these film a suitable candidate. Thus it is proposed for use in a THz device where high current density is a critical requirement.

Discussion of results on the above work and the conclusions are given below. Future work to be carried is proposed for a better understanding of emission mechanism and for enhancement of emission.

6.1 Study of Graphene Field Emission

The following parameters are studied with a view to obtain high current density.

- a) Emission from flakes: Significant amount of electron can only be obtained sharp edges of graphene when the electric field is applied along the sheet causing large field enhancement on the sharp tips. However, it is inefficient to extract current from non-uniform edges of graphene sheet as the total current would be much lower than expectation
- b) Emission from free standing films: Likewise, rGO sheets have to be oriented to align the edges with an applied electric field for electron emission. However field emission property with a very high emission current from rGO films[53] shows a great possibility as an electron source for high power terahertz vacuum electron devices (VEDs), where very dense, uniform and sheet beam is required, from a comparatively smaller dimension emitter. J. Liu et.al. [37] have shown that using a free standing, vertically aligned graphene oxide papers, sandwiched in wafer, 10 A/cm² of current density can be achieved, which is quite big for a field emitter.

6.2 Study of Various Synthesis Methods of rGO Film

Fabrication of free-standing graphene films has been very difficult to realize. Advanced methods to synthesize graphene is mostly substrate based, such as chemical vapor deposition [61], [62], electrophoretic deposition [36], screen printing [136], and spin coating [137], and are unable to produce free standing films. Thus, obtaining a large emission current from those film is extremely difficult, as those films are horizontal and only randomly oriented flakes are effectively acts as emitter. Because of this, those sheets end up as low current emitters. Fortunately, vertically oriented, free-standing rGO films [138] can emit large field emission current with large current density. Synthesis of thin free standing rGO film is possible only through chemical route. Graphite powder is oxidized first, then exfoliated into graphene oxide nano-sheets [97]. These nano-sheets can be converted into GO sheets using vacuum filtration. However, due to oxygen functional groups, these sheets suffer from degraded physical properties such as electrical and thermal

conductivities, which is reduced by two or sometimes three order. To restore those properties, we have devised a novel synthesis process.

6.3 Synthesis and Characterization of W-rGO Film

The synthesis of free-standing rGO films was carried out using modified hummers methods followed by a modified hydrothermal method, where those film were doped with tungsten nano-particle to remove oxygen functional groups and restore physical properties. For homogenous mixing and uniform doping, a novel sol-sol method was incorporated. GO solution was mixed with tungsten oxide solution. After that, the mixture was put into a novel in-house developed hydrothermal vessel for a simultaneous doping and film forming process. Amount of solution was controlled to acquire a film thickness of 100nm. Similar synthesis process was used to fabricated as-prepared rGO films (without tungsten doping) for property and performance comparison. Synthesized films are annealed inside a furnace, under a nitrogen environment for further reduction. It has been found that W-rGO film can retain its structural integrity even in a very high annealing temperature of 1200°C, whereas-prepared rGO films broke down under an annealing temperature of 1000°C. After the annealing process, the films are characterized with FESEM, Raman, XRD and XPS, to confirm thickness, reduction of oxygen and recovery of the carbon domain. Film thickness was measured using FESEM, where results imply the thickness is maintained between 100 nm to 140 nm (Figure 3.5). From Raman data, I_D/I_G curve shows (Fig 3.9) constant rise for rGO films, where due to high temperature annealing defect in sp^2 domain increase, but for W-rGO film, from 800°C it can be observed that the restoration of sp^2 domain started to increased. This phenomenon is the result of doping of tungsten where due strong covalent bond between carbon and tungsten, evaporation of carbon is restricted. XPS has been used to analyze the elements present in the film. It can be said from the XPS that, wt% of carbon and tungsten maintain a ratio of 1:0.01. Presence of oxygen groups reduced significantly comparing to the films without the W doping, by more than 60%, which indicates a very high rate of improvements. Further EDA data from FESEM also verifies the XPS data. The XRD pattern of W-rGO composites collected is presented

in Figure 3.11. The comparatively narrow diffraction peak, which is centered at around 23.5° , belongs to the (002) plane of the graphene. Diffraction peaks of graphene and tungsten was found simultaneously, which confirms that the tungsten were successfully inserted into the rGO film. Any other peaks from impurities such as oxygen functional groups were not detected, which confirms largely pure and defect free structure of the synthesized film.

6.4 Characterization and Shaping of Synthesized Film

To gain further confidence on the above studies related to electrical conductivity, thermal conductivity and mechanical strength, a complete measurement study has been made and characterized for physical properties. After that, films are shaped using microtome technique. The discussion and conclusions on the measurement and shaping are as given below:

- (a) **Electrical conductivity:** Electrical sheet resistance has been measured using the four probe method has shown that it has been improved by more than one order. Calculated conductivity of these films are among the largest for a free standing W-rGO film so far to the best of our knowledge. Three different samples prepared using same synthesis method, was measured. Measured electrical conductivity was approx. 600000S/m for W-rGO which is 60 times more than the measured value for as-prepared rGO films.
- (b) **Thermal conductivity:** The in plane and cross plane thermal conductivity was measured for both of the films. Results have shown, that rGO films annealed at 800°C , and W-rGO films has a thermal conductivity of 140 W/mK and 160 W/mK respectively. Interestingly, W-rGO films annealed in 1200°C , have showed an increased thermal conductivity $\sim 260\text{ W/mK}$. It can be concluded that the high temperature annealing restore the graphene structure thus phonon transport [139], which is responsible for thermal conductivity inside graphene, became faster.
- (c) **Mechanical Properties:** Tensile strength for both the films, rGO and W-rGO

was measured using UTM. It has been found that the tensile strength of W-rGO annealed in 1200°C has been improved by 200% where the young's modulus is by ~ 20 times, compared to rGO films annealed in 800°C. These extremely large restorations of the physical properties can be attributed to our novel synthesis process where we successfully doped W into the rGO films by modifying the synthesis process and introducing a novel sol-sol mixing process.

6.5 Realization of W-rGO Film Field Emitter Cathode

Based on the work carried out so far, the following experiments were carried out for the realization of field emission performance from both of the films.

- (a) **Experiment setup:** Field emission experiment has been carried out on two different films prepared using same method, to verify the performance reproducibility of the films. Experiment has been done inside a stainless steel vacuum chamber. The chamber is equipped with rotary, turbo and ion pump which helped us to maintain a vacuum level $1e-8$ torr during the experiment. A DC power, two digital multimeter, phosphor screen and ccd camera has been used for the experiment. A $50\text{ k}\Omega$ resistance has been used to protect the setup from current overflow.
- (b) **Field emission experiment:** The field emission test result shows the extreme current density (Fig 8(a)) with impressive reliability for the W-rGO film, comparing to the as prepared rGO film. A very large current density of approx. 6000 A/cm^2 was achieved for an applied electric field of $7.4\text{V}/\mu\text{m}$, which is so far the highest for a W-rGO film to the best of our knowledge. Excellent stability can be observed over a 192 hours of test, at an applied field of $6.6\text{ V}/\mu\text{m}$ with less than 1% of fluctuation. The improvement and stability can be attributed to the doping of the tungsten nano-particle during the synthesis process. Emission pattern was acquired with the help of a phosphor screen. Rectangular sheet type beam pattern can be observed which denotes that emitted electron beam is sheet type in nature and can be shaped more precisely with a focusing

elements. From an after experiment FESEM image, it is evident for W-rGO films the film structure retains the structural integrity (though exfoliated nominally) where the rGO films edge is destroyed complete. From this result we can depict that the W-rGO films does not degrade even after a long cycle of field emission operation, which makes it a potential candidate for field emission cathode for realizable compact THz devices.

6.6 Suggestions for Future Work

Based on the work carried out so far, the following suggestions are made for future work for a better understanding of emission mechanism and for enhancement of emission.

- (a) In this study, tungsten has been used as a dopant metal to repair and improve broken carbon network inside a rGO film. Here we have optimized the annealing temperature, for maximum removal of oxygen functional groups and recovery of sp² domain. However, with optimization and parametrization of C:W, for more efficient recovery of carbon network would be an useful study to achieve further largely improved physical properties.
- (b) **Use of Cs-STEM to profile doping uniformity and condition:** In this study, tungsten has been doped to rGO and characterized by XRD and XPS. However, to quantify and observe the tungsten domain, tungsten-carbon domain, and graphitic domain, Cs-STEM would be useful tool. We can directly observe, analyze and with the analyzed data can optimized the doping thus improve the repairmen of the broken structure in a more efficient way.
- (c) **FTIR spectroscopy:** In this study we have characterized the synthesized film, using FESEM, Raman, XRD and XPS. However, for further analysis, FTIR (Fourier transform infrared), spectroscopy can be used. FTIR can deliver the information on transmission, absorption and reflection from a sample. Thus for graphene we can calculate the transmission coefficient of the prepared sample. With these data further improvement can be carried out.
- (d) **Use of efficient testing jig to extract maximum current:** As showed in section

5.2, the testing jig which consists of a molybdenum sheet with holes, (anode1), suffers from a large degassing as a large number of electrons strike on the sheet itself. Comparatively a fewer number of electrons passes through the holes. This phenomenon degrades the local vacuum condition (between anode1 and emitter edge). Therefore, the applied potential was limited due to arcing. Use of a gate with sleet would be more efficient as if, designed properly, ~100% emitted electron will pass through the gate thus maintaining high vacuum condition, and extracting a maximum possible current.

Bibliography

- [1] J. H. Booske *et al.*, “Vacuum Electronic High Power Terahertz Sources,” *IEEE Trans. Terahertz Sci. Technol.*, vol. 1, no. 1, pp. 54–75, Sep. 2011.
- [2] E. L. Murphy and R. H. Good, “Thermionic Emission, Field Emission, and the Transition Region,” *Phys Rev*, vol. 102, no. 6, pp. 1464–1473, Jun. 1956.
- [3] F. A. Padovani and R. Stratton, “Field and thermionic-field emission in Schottky barriers,” *Solid-State Electron.*, vol. 9, no. 7, pp. 695–707, Jul. 1966.
- [4] G. Z. Yue *et al.*, “Generation of continuous and pulsed diagnostic imaging x-ray radiation using a carbon-nanotube-based field-emission cathode,” *Appl. Phys. Lett.*, vol. 81, no. 2, pp. 355–357, Jun. 2002.
- [5] A. K. Geim and K. S. Novoselov, “The rise of graphene,” *Nat. Mater.*, vol. 6, no. 3, pp. 183–191, 2007.
- [6] R. F. Greene and H. F. Gray, “Field emitter array,” Sep. 1992.
- [7] X.-M. Zhao, Y. Xia, and G. M. Whitesides, “Soft lithographic methods for nano-fabrication,” *J. Mater. Chem.*, vol. 7, no. 7, pp. 1069–1074, 1997.
- [8] J. A. Crawley and V. J. Saywell, “Chemical vapor deposition,” Feb. 1999.
- [9] K. S. Novoselov, V. Fal, L. Colombo, P. Gellert, M. Schwab, and K. Kim, “A roadmap for graphene,” *Nature*, vol. 490, no. 7419, pp. 192–200, 2012.
- [10] S. Cahangirov, M. Topsakal, E. Aktürk, H. Şahin, and S. Ciraci, “Two-and one-dimensional honeycomb structures of silicon and germanium,” *Phys. Rev. Lett.*, vol. 102, no. 23, p. 236804, 2009.
- [11] H. Lipsanen, “Structure and Electrical Characteristics of Graphene Field Effect Transistors,” *PhD Diss Aalto Univ.*, 2011.
- [12] A. V. Raghu, Y. R. Lee, H. M. Jeong, and C. M. Shin, “Preparation and physical properties of waterborne polyurethane/functionalized graphene sheet nanocomposites,” *Macromol. Chem. Phys.*, vol. 209, no. 24, pp. 2487–2493, 2008.
- [13] D. K. Schroder and J. A. Babcock, “Negative bias temperature instability: Road to cross in deep submicron silicon semiconductor manufacturing,” *J. Appl. Phys.*, vol. 94, no. 1, pp. 1–18, 2003.
- [14] G. Eda, H. Emrah Unalan, N. Rupesinghe, G. A. Amaratunga, and M. Chhowalla, “Field emission from graphene based composite thin films,” *Appl.*

- Phys. Lett.*, vol. 93, no. 23, p. 233502, 2008.
- [15] S. Kim, J. Ihm, H. J. Choi, and Y.-W. Son, “Origin of anomalous electronic structures of epitaxial graphene on silicon carbide,” *Phys. Rev. Lett.*, vol. 100, no. 17, p. 176802, 2008.
- [16] A. Reina *et al.*, “Large area, few-layer graphene films on arbitrary substrates by chemical vapor deposition,” *Nano Lett.*, vol. 9, no. 1, pp. 30–35, 2008.
- [17] K. F. Mak, C. H. Lui, J. Shan, and T. F. Heinz, “Observation of an electric-field-induced band gap in bilayer graphene by infrared spectroscopy,” *Phys. Rev. Lett.*, vol. 102, no. 25, p. 256405, 2009.
- [18] C. H. Lui, Z. Li, K. F. Mak, E. Cappelluti, and T. F. Heinz, “Observation of an electrically tunable band gap in trilayer graphene,” *Nat. Phys.*, vol. 7, no. 12, pp. 944–947, 2011.
- [19] G. Xu *et al.*, “Enhanced conductance fluctuation by quantum confinement effect in graphene nanoribbons,” *Nano Lett.*, vol. 10, no. 11, pp. 4590–4594, 2010.
- [20] F. Guinea, M. Katsnelson, and A. Geim, “Energy gaps and a zero-field quantum Hall effect in graphene by strain engineering,” *Nat. Phys.*, vol. 6, no. 1, pp. 30–33, 2010.
- [21] M. Y. Han, B. Özyilmaz, Y. Zhang, and P. Kim, “Energy band-gap engineering of graphene nanoribbons,” *Phys. Rev. Lett.*, vol. 98, no. 20, p. 206805, 2007.
- [22] M. Yankowitz, F. Wang, C. N. Lau, and B. J. LeRoy, “Local spectroscopy of the electrically tunable band gap in trilayer graphene,” *Phys. Rev. B*, vol. 87, no. 16, p. 165102, 2013.
- [23] A. A. Balandin, “Thermal properties of graphene and nanostructured carbon materials,” *Nat. Mater.*, vol. 10, no. 8, pp. 569–581, 2011.
- [24] R. R. Schaller, “Moore’s law: past, present and future,” *IEEE Spectr.*, vol. 34, no. 6, pp. 52–59, 1997.
- [25] K. S. Kim *et al.*, “Large-scale pattern growth of graphene films for stretchable transparent electrodes,” *nature*, vol. 457, no. 7230, pp. 706–710, 2009.
- [26] S. S. Varghese, S. Lonkar, K. Singh, S. Swaminathan, and A. Abdala, “Recent advances in graphene based gas sensors,” *Sens. Actuators B Chem.*, vol. 218, pp. 160–183, 2015.
- [27] A. Reserbat-Plantey *et al.*, “Electromechanical control of nitrogen-vacancy

- defect emission using graphene NEMS,” *Nat. Commun.*, vol. 7, 2016.
- [28] T. Gu *et al.*, “Regenerative oscillation and four-wave mixing in graphene optoelectronics,” *Nat. Photonics*, vol. 6, no. 8, pp. 554–559, 2012.
- [29] J. S. Suh, K. S. Jeong, J. S. Lee, and I. Han, “Study of the field-screening effect of highly ordered carbon nanotube arrays,” *Appl. Phys. Lett.*, vol. 80, no. 13, pp. 2392–2394, 2002.
- [30] J. H. Yim, Y. S. Kim, K. H. Koh, and S. Lee, “Fabrication of transparent single wall carbon nanotube films with low sheet resistance,” *J. Vac. Sci. Technol. B Microelectron. Nanometer Struct. Process. Meas. Phenom.*, vol. 26, no. 2, pp. 851–855, 2008.
- [31] W. L. Wang *et al.*, “Direct observation of a long-lived single-atom catalyst chiseling atomic structures in graphene,” *Nano Lett.*, vol. 14, no. 2, pp. 450–455, 2014.
- [32] G. M. Viskadourous, M. M. Stylianakis, E. Kymakis, and E. Stratakis, “Enhanced Field Emission from Reduced Graphene Oxide Polymer Composites,” *ACS Appl. Mater. Interfaces*, vol. 6, no. 1, pp. 388–393, Jan. 2014.
- [33] H. J. Jeong *et al.*, “Flexible field emission from thermally welded chemically doped graphene thin films,” *Small*, vol. 8, no. 2, pp. 272–280, 2012.
- [34] J. Li *et al.*, “The improvement of the field emission properties from graphene films: Ti transition layer and annealing process,” *AIP Adv.*, vol. 2, no. 2, p. 022101, 2012.
- [35] S. Santandrea *et al.*, “Field emission from single and few-layer graphene flakes,” *Appl. Phys. Lett.*, vol. 98, no. 16, p. 163109, Apr. 2011.
- [36] Z. Wu *et al.*, “Field emission of single-layer graphene films prepared by electrophoretic deposition,” *Adv. Mater.*, vol. 21, no. 17, pp. 1756–1760, 2009.
- [37] J. Liu *et al.*, “Graphene electron cannon: High-current edge emission from aligned graphene sheets,” *Appl. Phys. Lett.*, vol. 104, no. 2, p. 023101, 2014.
- [38] W. Zhu, *Vacuum microelectronics*. John Wiley & Sons, 2004.
- [39] K. S. Novoselov *et al.*, “Two-dimensional atomic crystals,” *Proc. Natl. Acad. Sci. U. S. A.*, vol. 102, no. 30, pp. 10451–10453, Jul. 2005.
- [40] R. H. Fowler and L. Nordheim, “Electron emission in intense electric fields,” presented at the Proceedings of the Royal Society of London A: Mathematical, Physical and Engineering Sciences, 1928, vol. 119, pp. 173–181.

- [41] W. Brinkman, R. Dynes, and J. Rowell, "Tunneling conductance of asymmetrical barriers," *J. Appl. Phys.*, vol. 41, no. 5, pp. 1915–1921, 1970.
- [42] P. Cutler, J. He, J. Miller, N. Miskovsky, B. Weiss, and T. Sullivan, "Theory of electron emission in high fields from atomically sharp emitters: Validity of the Fowler-Nordheim equation," *Prog. Surf. Sci.*, vol. 42, no. 1–4, pp. 169–185, 1993.
- [43] L. A. Samoska, "An overview of solid-state integrated circuit amplifiers in the submillimeter-wave and THz regime," *IEEE Trans. Terahertz Sci. Technol.*, vol. 1, no. 1, pp. 9–24, 2011.
- [44] R. Köhler *et al.*, "Terahertz semiconductor-heterostructure laser," *Nature*, vol. 417, no. 6885, pp. 156–159, 2002.
- [45] W. Liu, Y. Lu, L. Wang, and Q. Jia, "A compact terahertz free-electron laser with two gratings driven by two electron-beams," *Phys. Plasmas*, vol. 24, no. 2, p. 023109, 2017.
- [46] W. Li, Y. Lu, Z. He, Q. Jia, and L. Wang, "Harmonics generation of a terahertz wakefield free-electron laser from a dielectric loaded waveguide excited by a direct current electron beam," *Opt. Lett.*, vol. 41, no. 11, pp. 2458–2461, 2016.
- [47] G. Chattopadhyay, "Technology, capabilities, and performance of low power terahertz sources," *IEEE Trans. Terahertz Sci. Technol.*, vol. 1, no. 1, pp. 33–53, 2011.
- [48] P. H. Siegel, "Terahertz technology," *IEEE Trans. Microw. Theory Tech.*, vol. 50, no. 3, pp. 910–928, 2002.
- [49] T. Otsuji, "Trends in the research of modern terahertz detectors: plasmon detectors," *IEEE Trans. Terahertz Sci. Technol.*, vol. 5, no. 6, pp. 1110–1120, 2015.
- [50] B. Gorshunov *et al.*, "Terahertz BWO-spectroscopy," *Int. J. Infrared Millim. Waves*, vol. 26, no. 9, pp. 1217–1240, 2005.
- [51] Y.-Q. Liu, C.-H. Du, and P.-K. Liu, "Spoof-surface-plasmons-assisted enhanced terahertz vacuum electronic source," presented at the Millimetre Waves and Terahertz Technologies (UCMMT), 2016 IEEE 9th UK-Europe-China Workshop on, 2016, pp. 44–47.
- [52] S.-T. Han *et al.*, "Experimental investigations on miniaturized high-frequency vacuum electron devices," *IEEE Trans. Plasma Sci.*, vol. 33, no. 2, pp. 679–684, 2005.

Bibliography

- [53] H. Yamaguchi *et al.*, “Field emission from atomically thin edges of reduced graphene oxide,” *Acs Nano*, vol. 5, no. 6, pp. 4945–4952, 2011.
- [54] G. Viskadourous, D. Konios, E. Kymakis, and E. Stratakis, “Electron field emission from graphene oxide wrinkles,” *RSC Adv.*, vol. 6, no. 4, pp. 2768–2773, 2016.
- [55] G. Wu, X. Wei, S. Gao, Q. Chen, and L. Peng, “Tunable graphene micro-emitters with fast temporal response and controllable electron emission,” *Nat. Commun.*, vol. 7, 2016.
- [56] U. Palnitkar, R. V. Kashid, M. A. More, D. S. Joag, L. Panchakarla, and C. Rao, “Remarkably low turn-on field emission in undoped, nitrogen-doped, and boron-doped graphene,” *Appl. Phys. Lett.*, vol. 97, no. 6, p. 063102, 2010.
- [57] M. Daud, M. S. Kamal, F. Shehzad, and M. A. Al-Harathi, “Graphene/layered double hydroxides nanocomposites: a review of recent progress in synthesis and applications,” *Carbon*, vol. 104, pp. 241–252, 2016.
- [58] V. Eswaraiyah, S. S. J. Aravind, and S. Ramaprabhu, “Top down method for synthesis of highly conducting graphene by exfoliation of graphite oxide using focused solar radiation,” *J. Mater. Chem.*, vol. 21, no. 19, pp. 6800–6803, 2011.
- [59] J. Cai *et al.*, “Atomically precise bottom-up fabrication of graphene nanoribbons,” *Nature*, vol. 466, no. 7305, pp. 470–473, 2010.
- [60] S. Stankovich *et al.*, “Synthesis of graphene-based nanosheets via chemical reduction of exfoliated graphite oxide,” *carbon*, vol. 45, no. 7, pp. 1558–1565, 2007.
- [61] M. Losurdo, M. M. Giangregorio, P. Capezzuto, and G. Bruno, “Graphene CVD growth on copper and nickel: role of hydrogen in kinetics and structure,” *Phys. Chem. Chem. Phys.*, vol. 13, no. 46, pp. 20836–20843, 2011.
- [62] J. Shi *et al.*, “3D Mesoporous Graphene: CVD Self-Assembly on Porous Oxide Templates and Applications in High-Stable Li-S Batteries,” *Small*, vol. 11, no. 39, pp. 5243–5252, 2015.
- [63] S. Choubak, P. L. Levesque, E. Gaufres, M. Biron, P. Desjardins, and R. Martel, “Graphene CVD: interplay between growth and etching on morphology and stacking by hydrogen and oxidizing impurities,” *J. Phys. Chem. C*, vol. 118, no. 37, pp. 21532–21540, 2014.
- [64] P. W. Sutter, J.-I. Flege, and E. A. Sutter, “Epitaxial graphene on ruthenium,” *Nat. Mater.*, vol. 7, no. 5, pp. 406–411, 2008.

Bibliography

- [65] H. Chen, W. Zhu, and Z. Zhang, “Contrasting behavior of carbon nucleation in the initial stages of graphene epitaxial growth on stepped metal surfaces,” *Phys. Rev. Lett.*, vol. 104, no. 18, p. 186101, 2010.
- [66] W. Yang *et al.*, “Epitaxial growth of single-domain graphene on hexagonal boron nitride,” *Nat. Mater.*, vol. 12, no. 9, pp. 792–797, 2013.
- [67] Y. Zhang, K. Fugane, T. Mori, L. Niu, and J. Ye, “Wet chemical synthesis of nitrogen-doped graphene towards oxygen reduction electrocatalysts without high-temperature pyrolysis,” *J. Mater. Chem.*, vol. 22, no. 14, pp. 6575–6580, 2012.
- [68] Z. Lin, G. Waller, Y. Liu, M. Liu, and C. Wong, “Facile synthesis of nitrogen-doped graphene via pyrolysis of graphene oxide and urea, and its electrocatalytic activity toward the oxygen-reduction reaction,” *Adv. Energy Mater.*, vol. 2, no. 7, pp. 884–888, 2012.
- [69] X. Wang, L. Zhi, and K. Müllen, “Transparent, conductive graphene electrodes for dye-sensitized solar cells,” *Nano Lett.*, vol. 8, no. 1, pp. 323–327, 2008.
- [70] H. Wang, J. T. Robinson, X. Li, and H. Dai, “Solvothermal reduction of chemically exfoliated graphene sheets,” *J. Am. Chem. Soc.*, vol. 131, no. 29, pp. 9910–9911, 2009.
- [71] Y. Si and E. T. Samulski, “Exfoliated graphene separated by platinum nanoparticles,” *Chem. Mater.*, vol. 20, no. 21, pp. 6792–6797, 2008.
- [72] S. Stankovich, R. D. Piner, S. T. Nguyen, and R. S. Ruoff, “Synthesis and exfoliation of isocyanate-treated graphene oxide nanoplatelets,” *Carbon*, vol. 44, no. 15, pp. 3342–3347, 2006.
- [73] G. Ciofani, V. Raffa, Y. Obata, A. Menciassi, P. Dario, and S. Takeoka, “Magnetic driven alginate nanoparticles for targeted drug delivery,” *Curr Nanosci*, vol. 4, 2008.
- [74] J. Park, C. Ruiz-Vargas, M. P. Levendoff, and L. Brown, “Transfer-free batch fabrication of single layer graphene devices,” Jun. 2016.
- [75] M. A. Hamrick, “Mechanical Exfoliation of 2D Nanomaterials Using Simple Machines,” 2016.
- [76] L. Liu, X.-X. Lin, S.-Y. Zou, A.-J. Wang, J.-R. Chen, and J.-J. Feng, “One-pot wet-chemical synthesis of PtPd@ Pt nanocrystals supported on reduced graphene oxide with highly electrocatalytic performance for ethylene glycol oxidation,” *Electrochimica Acta*, vol. 187, pp. 576–583, 2016.

Bibliography

- [77] M. Antonietti and K. Müllen, *Chemical Synthesis and Applications of Graphene and Carbon Materials*. John Wiley & Sons, 2016.
- [78] S. P. Sasikala, P. Poulin, and C. Aymonier, “Advances in Subcritical Hydro-/Solvothermal Processing of Graphene Materials,” *Adv. Mater.*, 2017.
- [79] R. Atchudan, T. N. J. I. Edison, S. Perumal, D. Karthikeyan, and Y. R. Lee, “Facile synthesis of zinc oxide nanoparticles decorated graphene oxide composite via simple solvothermal route and their photocatalytic activity on methylene blue degradation,” *J. Photochem. Photobiol. B*, vol. 162, pp. 500–510, 2016.
- [80] J. M. Tour and D. V. Kosynkin, “Highly oxidized graphene oxide and methods for production thereof,” Aug. 2016.
- [81] H. Yu, B. Zhang, C. Bulin, R. Li, and R. Xing, “High-efficient synthesis of graphene oxide based on improved hummers method,” *Sci. Rep.*, vol. 6, p. 36143, 2016.
- [82] N. Zaaba, K. Foo, U. Hashim, S. Tan, W.-W. Liu, and C. Voon, “Synthesis of Graphene Oxide using Modified Hummers Method: Solvent Influence,” *Procedia Eng.*, vol. 184, pp. 469–477, 2017.
- [83] J. Sun *et al.*, “Solution-assisted ultrafast transfer of graphene-based thin films for solar cells and humidity sensors,” *Nanotechnology*, vol. 28, no. 13, p. 134004, 2017.
- [84] B. Tang, L. Zhang, R. Li, J. Wu, M. N. Hedhili, and P. Wang, “Are vacuum-filtrated reduced graphene oxide membranes symmetric?,” *Nanoscale*, vol. 8, no. 2, pp. 1108–1116, 2016.
- [85] B. Xie *et al.*, “Hydrothermal synthesis of layered molybdenum sulfide/N-doped graphene hybrid with enhanced supercapacitor performance,” *Carbon*, vol. 99, pp. 35–42, 2016.
- [86] E. Rokhsat and O. Akhavan, “Improving the photocatalytic activity of graphene oxide/ZnO nanorod films by UV irradiation,” *Appl. Surf. Sci.*, vol. 371, pp. 590–595, 2016.
- [87] Y. Zhou, Q. Bao, L. A. L. Tang, Y. Zhong, and K. P. Loh, “Hydrothermal dehydration for the ‘green’ reduction of exfoliated graphene oxide to graphene and demonstration of tunable optical limiting properties,” *Chem. Mater.*, vol. 21, no. 13, pp. 2950–2956, 2009.
- [88] D. Pan, J. Zhang, Z. Li, and M. Wu, “Hydrothermal route for cutting graphene sheets into blue-luminescent graphene quantum dots,” *Adv. Mater.*, vol. 22, no. 6, pp. 734–738, 2010.

- [89] Y. Xu, K. Sheng, C. Li, and G. Shi, "Self-assembled graphene hydrogel via a one-step hydrothermal process," *ACS Nano*, vol. 4, no. 7, pp. 4324–4330, 2010.
- [90] Z. Xu, Z. Liu, H. Sun, and C. Gao, "Highly electrically conductive ag-doped graphene fibers as stretchable conductors," *Adv. Mater.*, vol. 25, no. 23, pp. 3249–3253, 2013.
- [91] Y. Shi, K. K. Kim, A. Reina, M. Hofmann, L.-J. Li, and J. Kong, "Work function engineering of graphene electrode via chemical doping," *ACS Nano*, vol. 4, no. 5, pp. 2689–2694, 2010.
- [92] M. Giovanni *et al.*, "Noble metal (Pd, Ru, Rh, Pt, Au, Ag) doped graphene hybrids for electrocatalysis," *Nanoscale*, vol. 4, no. 16, pp. 5002–5008, 2012.
- [93] Y. Guo, X. Sun, Y. Liu, W. Wang, H. Qiu, and J. Gao, "One pot preparation of reduced graphene oxide (RGO) or Au (Ag) nanoparticle-RGO hybrids using chitosan as a reducing and stabilizing agent and their use in methanol electrooxidation," *Carbon*, vol. 50, no. 7, pp. 2513–2523, 2012.
- [94] S. Guo, D. Wen, Y. Zhai, S. Dong, and E. Wang, "Platinum nanoparticle ensemble-on-graphene hybrid nanosheet: one-pot, rapid synthesis, and used as new electrode material for electrochemical sensing," *ACS Nano*, vol. 4, no. 7, pp. 3959–3968, 2010.
- [95] P. T. Yin, S. Shah, M. Chhowalla, and K.-B. Lee, "Design, synthesis, and characterization of graphene–nanoparticle hybrid materials for bioapplications," *Chem. Rev.*, vol. 115, no. 7, pp. 2483–2531, 2015.
- [96] P. T. Yin, T.-H. Kim, J.-W. Choi, and K.-B. Lee, "Prospects for graphene–nanoparticle-based hybrid sensors," *Phys. Chem. Chem. Phys.*, vol. 15, no. 31, pp. 12785–12799, 2013.
- [97] W. S. Hummers Jr and R. E. Offeman, "Preparation of graphitic oxide," *J. Am. Chem. Soc.*, vol. 80, no. 6, pp. 1339–1339, 1958.
- [98] D. Long, W. Li, L. Ling, J. Miyawaki, I. Mochida, and S.-H. Yoon, "Preparation of nitrogen-doped graphene sheets by a combined chemical and hydrothermal reduction of graphene oxide," *Langmuir*, vol. 26, no. 20, pp. 16096–16102, 2010.
- [99] J. Shen, B. Yan, M. Shi, H. Ma, N. Li, and M. Ye, "One step hydrothermal synthesis of TiO₂-reduced graphene oxide sheets," *J. Mater. Chem.*, vol. 21, no. 10, pp. 3415–3421, 2011.
- [100] X. Zhou, T. Shi, and H. Zhou, "Hydrothermal preparation of ZnO-reduced

- graphene oxide hybrid with high performance in photocatalytic degradation,” *Appl. Surf. Sci.*, vol. 258, no. 17, pp. 6204–6211, 2012.
- [101] J. Shen, M. Shi, B. Yan, H. Ma, N. Li, and M. Ye, “One-pot hydrothermal synthesis of Ag-reduced graphene oxide composite with ionic liquid,” *J. Mater. Chem.*, vol. 21, no. 21, pp. 7795–7801, 2011.
- [102] R. Barik *et al.*, “A novel approach to synthesis of scandia-doped tungsten nano-particles for high-current-density cathode applications,” *Int. J. Refract. Met. Hard Mater.*, vol. 38, pp. 60–66, 2013.
- [103] N. Colthup, *Introduction to infrared and Raman spectroscopy*. Elsevier, 2012.
- [104] A. C. Ferrari, “Raman spectroscopy of graphene and graphite: disorder, electron–phonon coupling, doping and nonadiabatic effects,” *Solid State Commun.*, vol. 143, no. 1, pp. 47–57, 2007.
- [105] L. Whittig and W. Allardice, “X-ray diffraction techniques,” *Methods Soil Anal. Part 1—Physical Mineral. Methods*, no. methodsofsoilan1, pp. 331–362, 1986.
- [106] J. F. Watts and J. Wolstenholme, “An introduction to surface analysis by XPS and AES,” 2003.
- [107] A. Siokou, F. Ravani, S. Karakalos, O. Frank, M. Kalbac, and C. Galiotis, “Surface refinement and electronic properties of graphene layers grown on copper substrate: an XPS, UPS and EELS study,” *Appl. Surf. Sci.*, vol. 257, no. 23, pp. 9785–9790, 2011.
- [108] X. Bo *et al.*, “The research on improving the anti-oxidation of tungsten rhenium alloy wires,” presented at the Journal of Physics: Conference Series, 2017, vol. 885, p. 012019.
- [109] F. Smits, “Measurement of sheet resistivities with the four-point probe,” *Bell Labs Tech. J.*, vol. 37, no. 3, pp. 711–718, 1958.
- [110] M. P. Gutiérrez, H. Li, and J. Patton, “Thin film surface resistivity,” *Mater. Eng.*, pp. 0–24, 2002.
- [111] G. Reeves and H. Harrison, “Obtaining the specific contact resistance from transmission line model measurements,” *IEEE Electron Device Lett.*, vol. 3, no. 5, pp. 111–113, 1982.
- [112] J. G. Webster, *Electrical measurement, signal processing, and displays*. CRC Press, 2003.
- [113] G. Xin *et al.*, “Highly thermally conductive and mechanically strong

- graphene fibers,” *Science*, vol. 349, no. 6252, pp. 1083–1087, 2015.
- [114] L. Peng, Z. Xu, Z. Liu, Y. Guo, P. Li, and C. Gao, “Ultrahigh Thermal Conductive yet Superflexible Graphene Films,” *Adv. Mater.*, 2017.
- [115] Y. Chen *et al.*, “Reduced Graphene Oxide Films with Ultrahigh Conductivity as Li-Ion Battery Current Collectors,” *Nano Lett.*, vol. 16, no. 6, pp. 3616–3623, 2016.
- [116] K. K. Kim *et al.*, “Enhancing the conductivity of transparent graphene films via doping,” *Nanotechnology*, vol. 21, no. 28, p. 285205, 2010.
- [117] A. Kasry, M. A. Kuroda, G. J. Martyna, G. S. Tulevski, and A. A. Bol, “Chemical doping of large-area stacked graphene films for use as transparent, conducting electrodes,” *ACS Nano*, vol. 4, no. 7, pp. 3839–3844, 2010.
- [118] L. L. Zhang *et al.*, “Highly conductive and porous activated reduced graphene oxide films for high-power supercapacitors,” *Nano Lett.*, vol. 12, no. 4, pp. 1806–1812, 2012.
- [119] S. Pei and H.-M. Cheng, “The reduction of graphene oxide,” *Carbon*, vol. 50, no. 9, pp. 3210–3228, 2012.
- [120] R. Taylor, “Thermal conductivity determinations of thermal barrier coatings,” *Mater. Sci. Eng. A*, vol. 245, no. 2, pp. 160–167, 1998.
- [121] J. D. Renteria *et al.*, “Strongly anisotropic thermal conductivity of free-standing reduced graphene oxide films annealed at high temperature,” *Adv. Funct. Mater.*, vol. 25, no. 29, pp. 4664–4672, 2015.
- [122] R. Bowen and M. S. Rodriguez, “Tensile strength and modulus of elasticity of tooth structure and several restorative materials,” *J. Am. Dent. Assoc.*, vol. 64, no. 3, pp. 378–387, 1962.
- [123] F. Shama and P. Sherman, “Evaluation of some textural properties of foods with the Instron Universal Testing Machine,” *J. Texture Stud.*, vol. 4, no. 3, pp. 344–352, 1973.
- [124] Q. Lu, M. Arroyo, and R. Huang, “Elastic bending modulus of monolayer graphene,” *J. Phys. Appl. Phys.*, vol. 42, no. 10, p. 102002, 2009.
- [125] D. Sen, K. S. Novoselov, P. M. Reis, and M. J. Buehler, “Tearing graphene sheets from adhesive substrates produces tapered nanoribbons,” *Small*, vol. 6, no. 10, pp. 1108–1116, 2010.
- [126] C. Lee, X. Wei, J. W. Kysar, and J. Hone, “Measurement of the elastic properties and intrinsic strength of monolayer graphene,” *science*, vol. 321,

- no. 5887, pp. 385–388, 2008.
- [127] R. Grantab, V. B. Shenoy, and R. S. Ruoff, “Anomalous strength characteristics of tilt grain boundaries in graphene,” *Science*, vol. 330, no. 6006, pp. 946–948, 2010.
- [128] B. Hajgató *et al.*, “Theoretical investigation of the intrinsic mechanical properties of single-and double-layer graphene,” *J. Phys. Chem. C*, vol. 116, no. 42, pp. 22608–22618, 2012.
- [129] Y. Liu, B. Xie, Z. Zhang, Q. Zheng, and Z. Xu, “Mechanical properties of graphene papers,” *J. Mech. Phys. Solids*, vol. 60, no. 4, pp. 591–605, 2012.
- [130] S. Park, K.-S. Lee, G. Bozoklu, W. Cai, S. T. Nguyen, and R. S. Ruoff, “Graphene oxide papers modified by divalent ions—enhancing mechanical properties via chemical cross-linking,” *ACS Nano*, vol. 2, no. 3, pp. 572–578, 2008.
- [131] X. Wang *et al.*, “Mechanical properties of polymer composites reinforced by functionalized graphene prepared via direct exfoliation of graphite flakes in styrene,” *RSC Adv.*, vol. 6, no. 113, pp. 112486–112492, 2016.
- [132] L. M. Ephrath, “Reactive ion etching,” Aug. 1981.
- [133] M. Yamada, “Laser cutting process,” Dec. 1994.
- [134] A. Von Bohlen, R. Klockenkämper, G. Tölg, and B. Wiecken, “Microtome sections of biomaterials for trace analyses by TXRF,” *Fresenius Z. Für Anal. Chem.*, vol. 331, no. 3–4, pp. 454–458, 1988.
- [135] L. A. Giannuzzi, *Introduction to focused ion beams: instrumentation, theory, techniques and practice*. Springer Science & Business Media, 2006.
- [136] J. Ping, J. Wu, Y. Wang, and Y. Ying, “Simultaneous determination of ascorbic acid, dopamine and uric acid using high-performance screen-printed graphene electrode,” *Biosens. Bioelectron.*, vol. 34, no. 1, pp. 70–76, 2012.
- [137] C. Spindt, I. Brodie, L. Humphrey, and E. Westerberg, “Physical properties of thin-film field emission cathodes with molybdenum cones,” *J. Appl. Phys.*, vol. 47, no. 12, pp. 5248–5263, 1976.
- [138] C. S. Rout *et al.*, “Superior field emission properties of layered WS₂-RGO nanocomposites,” *Sci. Rep.*, vol. 3, 2013.
- [139] A. A. Balandin *et al.*, “Superior thermal conductivity of single-layer graphene,” *Nano Lett.*, vol. 8, no. 3, pp. 902–907, 2008.

List of Publications

Journal publications:

- [1] Narendra Kr. Singh, **Ranojoy Bhattacharya**, Hasina Khatun, Udaybir Singh, A K Sinha, “Simulation of Filament Heater for Uniform Emission from Dispenser Cathode,” *J. Fusion Energy*, vol. 31, no. 3, pp. 205–210, 2012.
- [2] Nitin Kumar, Udaybir Singh, Anil Kumar, **Ranojoy Bhattacharya**, T. P. Singh, A. K. Sinha, “Numerical design of megawatt gyrotron with 120 GHz frequency and 50% efficiency for plasma fusion application,” *J. Fusion Energy*, vol. 32, no. 1, pp. 20–27, 2013.
- [3] Hasina Khatun, **Ranojoy Bhattacharya**, Sudeep Sharan, Kapil Singhal, Uttam Gowswami, Anil Kumar, Nitin Kumar, Udaybir Singh, A.K. Sinha, “Design of single-stage depressed collector for 42 GHz, 200 kW gyrotron,” *Vacuum*, vol. 86, no. 10, pp. 1465–1469, 2012.
- [4] Uttam Kr Goswami, Udaybir Singh, Anil Kumar, **R Bhattacharya**, H Khatun, RL Dua and AK Sinha “Design Optimization of Un-Depressed Collector through Magnetic Field and Thermal Studies” International Journal of Engineering Science and Innovative Technology (IJESIT) Volume 1, Issue 2, November 2012
- [5] Anil Kumar, Nitin Kumar, Udaybir Singh, Ranojoy Bhattacharya, V. Yadav, and A. K. Sinha, “Towards a 1MW, 170GHz gyrotron design for fusion application,” *Infrared Phys. Technol.*, vol. 57, pp. 1–7, 2013.
- [6] Vivek Yadav, Nitin Kumar, Anil Kumar, Udaybir Singh, **R Bhattacharya**, SC Deorani and A.K. Sinha, “High-Frequency Transmission Characteristics of Inert Coolant Liquids for High-Power Gyrotron Windows,” *IEEE Trans. Plasma Sci.*, vol. 41, no. 3, pp. 450–455, 2013.
- [7] **Ranojoy Bhattacharya**, Hasina Khatun, Narendra Kr. Singh, Udaybir Singh, A. K. Sinha, “Design of Cathode Heater Assembly for High Power Gyrotron,” *Frequenz*, vol. 67, no. 5–6, pp. 163–167, 2013.
- [8] **Ranojoy Bhattacharya**, Naveen Kr Sahu, Arani Ali Khan, Hasina Khatun, A.K. Sinha, “Electrical and thermo-mechanical analysis of beam recovery system for megawatt power gyrotron,” *Fusion Eng. Des.*, vol. 88, no. 4, pp. 253–257, 2013.
- [9] Ohjoon Kwon, Matlabjon Abdurahimovich Sattorov, Sun-Hong Min, In-Keun Baek, Seontae Kim, Anirban Bera, Ranjan Kumar Barik, **Ranojoy**

- Bhattacharya**, Jin-Young Jeong, Jong-Hyo Won, and Gun-Sik Park, “Efficient terahertz oscillation using a half-period staggered grating resonator,” *Jpn. J. Appl. Phys.*, vol. 53, no. 6, p. 066201, 2014.
- [10] Matlabjon Sattorov, Eduard Khutoryan, Konstantin Lukin, Fellow, IEEE, Ohjoon Kwon, Sun-Hong Min, **Ranajoy Bhattacharya**, In-Keun Baek, Seontae Kim, Minwoo Yi, Jonho So, Gun-Sik Park, “Automodulation processes in clinotrons with low-focusing magnetic field,” *IEEE Trans. Electron Devices*, vol. 62, no. 5, pp. 1617–1621, 2015.
- [11] Eduard Khutoryan, Matlabjon Sattorov, Konstantin Alexandrovich Lukin, Fellow, IEEE, Oh-Joon Kwon, Sun-Hong Min, **Ranajoy Bhattacharya**, In-Keun Baek, Seontae Kim, Minwoo Yi, Joonho So, and Gun-Sik Par, “Theory of multimode resonant backward-wave oscillator with an inclined electron beam,” *IEEE Trans. Electron Devices*, vol. 62, no. 5, pp. 1628–1634, 2015.
- [12] Sun-Hong Min, Ohjoon Kwon, Matlabjon Sattorov, Hoechun Jung, In-Keun Baek, Seontae Kim, Anirban Bera, Ranjan Kumar Barik, **Ranajoy Bhattacharya**, and Gun-Sik Park, “Design Study of GW-THz Wave Transmission Without Mode Competition in an Oversized Relativistic Backward Wave Oscillator,” *IEEE Trans. Plasma Sci.*, vol. 45, no. 4, pp. 610–622, 2017.
- [13] In-Keun Baek, **Ranajoy Bhattacharya**, Jeong Seok Lee, Seontae Kim, Dongpyo Hong, Matlabjon A. Sattorov, Sun-Hong Min, Yong Hyup Kim & GunSik Park, “Uniform high current and current density field emission from the chiseled edge of a vertically aligned graphene-based thin film,” *J. Electromagn. Waves Appl.*, vol. 31, no. 18, pp. 2064–2073, 2017.
- [14] Sun-Hong Min, Ohjoon Kwon, Matlabjon Sattorov, Hoechun Jung, In-Keun Baek, Seontae Kim, Jin-Young Jeong, Jungmin Jang, Dongpyo Hong, **Ranajoy Bhattacharya**, Ranjan Kumar Barik, Anirban Bera, Seunghyuk Park, Jihwan Ahn, Sang Heun Lee, Young Joong Yoon & Gun-Sik Park, “Effects on electronics exposed to high-power microwaves on the basis of a relativistic backward-wave oscillator operating on the X-band,” *J. Electromagn. Waves Appl.*, vol. 31, no. 17, pp. 1875–1901, 2017.

Conference proceedings:

- [1] Hasina Khatun, Naveen K. Sahu, Sudeep Sharan, **Ranajoy Bhattacharya**, Uttam K. Goswami, Anil Kumar, Udaybir Singh, and Ashok Kumar Sinha, “Investigation of New Material for Megawatt Power Gyrotron Collector” In Proc. *PIERS 2012*, Kuala Lumpur, Malaysia, 27-30 March, 2012.

- [2] Anil Kumar, Nitin Kumar, Udaybir Singh, **Ranajoy Bhattacharya**, Narendra Kumar Singh, Hasina Khatun, Mukesh Kumar Alaria, and Ashok Kumar Sinha “Design of 120 GHz, 1 MW Gyrotron for Plasma Fusion Application” In Proc. *PIERS 2012*, Kuala Lumpur, Malaysia, 27-30 March 2012.
- [3] UttamGoswami, **Ranajoy Bhattacharya**, Sudeep Saran, Naveen Sahu, Udaybir Singh, Anil Kumar, Hasina Khatun and A K Sinha, “Design of single stage depressed collector for 120 GHz, 1MW gyrotron” In Proc. *Int. Conf. ICMARS-2011*, Jodhpur, India, 7-10 December, 2011,
- [4] Naveen kumar Sahu, **Ranajoy Bhattacharya**, Arani ali Khan, Uttam kumar Goswami, Udaybir Singh, Hasina Khatun & A.K. Sinha “Analysis of thermal behavior of 1 MW gyrotron collector” In Proc. *Int. Conf. E2NC-2012*, Mankundu, India, 3-4 February, 2012.
- [5] **Ranajoy Bhattacharya**, Naveen Kumar Sahu, Uttam Goswami, Hasina Khatun, Udaybir Singh, and Ashok K Sinha “Thermal and structural analysis of depressed collector for 42 GHz Gyrotron” In Proc. *Nat. Conf. MDCCT 2012*, Burdwan, India.6-7 February, 2012.
- [6] **Ranajoy Bhattacharya**, Tripti Sharma, Naveen Kr. Sahu, Narendra Singh, Hasina Khatun and AK Sinha “Structural and Vibrational Analysis of 42 Ghz 200 kW Gyrotron” In Proc. *Nat. Conf. Microwave-2012* Jaipur, India. 30th July-1st August, 2012.
- [7] **Ranajoy Bhattacharya**, In-Keun Baek, Jung Suk Lee, Seon-Tae Kim, Anil Kumar, Ohjoon Kwon and Gun-Sik Park, “Numerical Calculation of heat generation due to field emission current inside a rGO film”, In Proc. *5th International THz-Bio Workshop 2014*, Seoul National University, Seoul, Korea. April 02-04, 2014.
- [8] Seon-Tae Kim, In-Keun Baek, Ohjoon Kwon, **Ranajoy Bhattacharya**, Anil Kumar, Anirban Bera and Gun-Sik Park, “Observation of a radiative behavior of the surface resonance from a modified metal slit array”, In Proc. *5th International THz-Bio Workshop 2014*, Seoul National University, Seoul, Korea. April 02-04, 2014.
- [9] **Ranajoy Bhattacharya**, In-Keun Baek, Jeong Seok Lee, Seontae Kim, Anil Kumar, Ohjoon Kwon, Sun-Hong Min, Anirban Bera, Ranjan Kumar Barik, Matlabjon Sattorov, and Gun-Sik Park, “Calculation of thermal transport of heat due to field emission current inside a rGO film”, In Proc. *6th International THz-Bio Workshop 2015*, Seoul National University, Seoul, Korea. April 08-10, 2015.
- [10] **Ranajoy Bhattacharya**, In-Keun Baek, Jeong Seok Lee, Ranjan Kumar Barik, Seontae Kim, Dongpyo Hong, Ohjoon Kwon, Matlabjon A. Sattorov,

- Yong Hyup Kim, and Gun-Sik Park, “Investigation of emission capability of rGO film cathode for terahertz vacuum electron devices”, *In Proc. 40th International Conference on IRMMW-THz 2015*, Hong Kong 23-28 Aug, 2015.
- [11] In-Keun Baek, **Ranajoy Bhattacharya**, Jeong Seok Lee, Seontae Kim, Dongpyo Hong, Ohjoon. Kwon, Young Hyup Kim and Gun-Sik Park, “Conditioning of Vertically Aligned RGO Film Electron Emitter for Terahertz Vacuum Electronic Devices”, *In Proc. 40th International Conference on IRMMW-THz 2015*, Hong Kong, 23-28 Aug. 2015.
- [12] Seontae Kim, In-Keun Baek, Ohjoon Kwon, Anirban Bera, **Ranajoy Bhattacharya**, Sattorov Matlabjon, Sun-Hong Min and Gun-Sik Park, “Electromagneticfield enhancement in metallic metamaterials: A potential for compact THz free electron lasers” *In Proc. 40th International Conference on IRMMW-THz 2015*, Hong Kong, 23-28 Aug. 2015.
- [13] **Ranajoy Bhattacharya**, In-Keun Baek, Jeong Seok Lee, Ranjan Kumar Barik, Seontae Kim, Dongpyo Hong, Ohjoon Kwon, Matlabjon A. Sattorov, Yong Hyup Kim, and Gun-Sik Park, “High Current Density Field Emission from Tungsten-RGO Composite Films for the High Frequency Vacuum Electron Sources”, *In Proc. 7th JKVNS- 2015*, Seoul, Korea 24th October, 2015.
- [14] **Ranajoy Bhattacharya**, In-Keun Baek, Jeong Seok Lee, Ranjan Kumar Barik, Seontae Kim, Dongpyo Hong, Ohjoon Kwon, Matlabjon A. Sattorov, Yong Hyup Kim, and Gun-Sik Park, “Improving the electrical conductivity of rGO thin film using tungsten nano particle”, *In Proc. Int. Conf. IVESC-2016*, Seoul, Korea, 18-20 October, 2016,
- [15] Dongpyo Hong, **Ranajoy Bhattacharya**, In-Keun Baek, Jeong Seok Lee, Ranjan Kumar Barik, Seontae Kim, Ohjoon Kwon, Matlabjon A. Sattorov, Yong Hyup Kim, and Gun-Sik Park,” Novel simulation method for designing graphene thin film based field emitters”, *In Proc. Int. Conf. IVESC-2016*, Seoul, Korea 18-20 October, 2016.
- [16] **Ranajoy Bhattacharya**, In-Keun Baek, Ranjan Kumar Barik, Seontae Kim, Dongpyo Hong Ohjoon Kwon, Matlabjon A. Sattorov, and Gun-Sik Park, “Efficient sintering method for scandium doped nano particle thermionic cathodes.”, *In Proc. Int. Conf. IVESC-2016*, Seoul, Korea 18-20 October, 2016.
- [17] Matlabjon A. Sattorov, In-Keun Baek, **Ranajoy Bhattacharya**, Seontae Kim, Dongpyo Hong, Michael P. Perkins and Gun-Sik Park, “Beam transmission study in S-band sheet beam Klystrons, *In Proc. Int. Conf. IVESC-2016*, Seoul, Korea 18-20 October, 2016.

- [18] Seontae Kim, In-Keun Baek, **Ranajoy Bhattacharya**, Dongpyo Hong, Matlabjon A. Sattorov, Anirban Bera, Ohjoon Kwon, Sun-Hong Min and Gun-Sik Park, “Experimental observation of electromagnetic field enhancement in metallic metamaterials for strong interaction with convection electron.” *In Proc. Int. Conf. IVESC-2016*, Seoul, Korea 18-20 October, 2016.
- [19] Gun-Sik Park, Matlabjon A. Sattorov, In-Keun Baek, **Ranajoy Bhattacharya**, Seontae Kim, Dongpyo Hong, “Issues of vacuum electron sources in the applications of EM radiation.” *In Proc. Int. Conf. IVESC-2016*, Seoul, Korea 18-20 October, 2016.

APPENDIX-I

Estimation of chemicals required

1. Target- (C:Oxidizing agent) = 1:6 (Conventional methods)

1.1 Target (Modified)- (C:Oxidizing agent) = 1:(6 - doping material)

Target amount for doping material:

2. Aim- (C:W) = 3:(0.3 × positive integer) Tungsten (doping material) doped rGO

Amount of required raw materials:

Graphite powder= 0.3 gm

We need to find out:

Amount of required Tungsten Oxide (WO_3)

Amount of required Potassium Permanganate (KMnO_4)

Molar weight of W= 183.84 gm

Molar weight of O= 16 gm

Molar Weight of WO_3 = 231.84 gm

0.0375 gm WO_3 required for 0.03 gm W

Molar weight of KMnO_4 = 158.0339 gm

Molar weight of 1.8 gm= 284.46102 gm

Molar weight of 0.0375 gm WO_3 = 8.964 gm

Required molar weight of KMnO_4 = 275.49702gm

KMnO_4 required = 1.74 gm

국문초록:

진공전자소자를 보완할 수 있는 고출력, 효율적인 광원의 부족 인한 테라헤르츠 갭(THz-gap)으로 인해 이를 의료, 방위, 통신, 재료 처리 분야의 응용에 어려움을 겪고 있다. 실용적인 테라헤르파를 발생시킬 수 있는 진공전자소자를 실현하기 위해서는 극한의 전류 밀도를 갖는 음극의 중요성이 부각되고 있는 상황이다. 이 논문에서 우리는 테라헤르츠 주파수에서 동작하는 진공전자소자를 위한 전자빔 발생원으로 새로운 그래핀 필름을 기반으로한, 최대방출 전류밀도가 10000 A/cm^2 에 이르는 전계방출소자 음극을 합성하고 개발하였다. 전기전도성, 기계적 강도, 필름의 두께에 따른 전계 방출 메커니즘영향, 전계 방출 성능 및 안정성에 대한 이론적 연구가 수행되었다. 실험적 분석을 통해 전계 방출 성능이 필름에 존재하는 불순물의 존재에 의해 영향을 받는 것이 확인되었고 이는 필름에 포함된 불순물을 제거하면 전계방출 성능이 향상된다는 것을 의미한다. 또한 불순물에 의해 저하되는 그래핀 필름의 열-전기적 특성 및 기계적 특성이 전계방출 성능 및 안정성에 중요한 역할을 한다는 것을 보였다. 앞서 언급한 모든 측면을 고려하여 개선된 물리적 특성을 지닌, 불순물을 최소화한 자립형 그래핀 산화물(rGO) 필름을 합성하기 위한 화학공정을 개발하였다. 그래핀 산화물 필름에 금속을 도핑하면 수배 이상으로 물리적 특성이 향상되고 결과적으로 전계방출 성능이 향상된다. 시뮬레이션 및 분석 연구에 따르면 도핑에 의한 필름의 물리적 특성이 기존의 rGO 와 비교하여 적어도 두 배 이상 향상되면 방출 전류 밀도가 두 배 이상이라도 안정된 전계방출을 얻을 수 있음을 보였다. 이는 전계방출로 발생하는 열-전기 부하 처리 성능이 도핑된 그래핀 필름의 경우 더욱 향상되기 때문이다. 그래핀 필름의 모양과 두께는 전자현미경(SEM)으로, 원소정보, 도핑균일성, 탄소-탄소 결합구조는 X 선 분광학(XPS)을 이용하여, 도핑메커니즘 및 레이어간 거리는 X선 회절(X-ray diffraction, XRD)를 이용하여, 도핑이 탄소결합 네트워크 형상에 미치는 영향에 대해서는 라만 분광법(Raman spectroscopy)를 이용하여 각각 수행되었다. 금속 도핑된 그래핀 필름은 기존의 필름에 비해

향상된 결합구조를 갖는 것을 확인되었다. 또한 물리적 특성의 개선을 비교하기 위한 실험도 수행하였다. 도핑된 필름은 열적, 전기적 및 기계적 특성 모두 비 도핑 필름보다 향상된 특성을 갖는 것으로 확인되었다. 두 필름의 전계방출특성을 측정하기 위해서 초고진공환경서 전계방출 시험을 수행하였다. $7.4\text{V}/\mu\text{m}$ 인가 전기장 환경에서 도핑된 필름은 안정적으로 6000 A/cm^2 의 전류밀도를 방출하는데 비해 비 도핑 필름은 초기 4300 A/cm^2 의 전류 밀도에 도달 후 성능이 저하되어 2300 A/cm^2 의 전류밀도를 보였다. 도핑된 필름은 더 높은 인가 전기장에서도 안정적으로 높은 전류를 방출하는 I-V 특성을 보인다. 이는 고전압 정전파괴를 효율적으로 제어하는 시스템을 가능케하여 높은 전류밀도가 달성 될 수 있음을 의미한다. 높은 전압에서 정전파괴 현상을 제어할 수 있는 시스템으로 보다 높은 전류밀도를 효율적으로 달성 할 수 있다는 것을 의미한다.

주요어: rGO 필름, 텅스텐 도핑, 물리적 특성, 전계 방출, 안정성, 테라헤르츠 음극.

학번: 2013-30772